12-1-2008

Modeling solutions and simulations for advanced III-V photovoltaics based on nanostructures

Ryan Aguinaldo

Modeling Solutions and Simulations for Advanced III-V Photovoltaics Based on Nanostructures

by

Ryan Aguinaldo

A Thesis Submitted

in Partial Fulfillment

of the Requirements for the Degree of

Master of Science

in

Materials Science & Engineering

Approved by:

Prof. _____

Dr. Ryne P. Raffaelle (Thesis Co-Advisor)

Prof. _____

Dr. Seth M. Hubbard (Thesis Co-Advisor)

Prof. _____

Dr. Sean L. Rommel (Thesis Committee Member)

Center for Materials Science & Engineering

College of Science

Rochester Institute of Technology

Rochester, NY

December 2008

Modeling Solutions and Simulations for Advanced III-V Photovoltaics Based on Nanostructures

by

Ryan Aguinaldo

To Mimi and Mom, loving mothers.
Grandpa and grandma too.

Acknowledgements

First and foremost I must acknowledge my advisors Dr. Seth Hubbard and Dr. Ryne Raffaelle for their support and guidance over the past couple of years. Dr. Hubbard has been especially helpful in providing advice regarding the directions that this work has gone. I am also extremely grateful to the other member of my thesis committee, Dr. Sean Rommel. Dr. Rommel has been a wonderful source of guidance and assistance throughout both my undergraduate and graduate experiences.

I would also like to thank Dr. Cory Cress for always seeming more than willing to lend a helping hand wherever possible as well as Mr. Christopher Bailey for our many illuminating discussions and also for the many journal articles he has randomly brought to my attention. I also express gratitude to Dr. John Andersen and Dr. Christopher Collison for their assistance in academic matters and for the interactions I have had with them.

The numerical computations performed in this work could not have been possible without the resources provided by the Department of Research Computing. Additional work was performed at the computing facilities in the Center for Microelectronic and Computer Engineering. Device simulations were made possible by the donation of the Silvaco tools by Simucad Design Automation to the Department of Microelectronic Engineering.

This work has been partially supported by the United States Department of Energy, Solar Energy Technologies Program (Grant #DE-FG3608GO18012) and other government agencies.

Abstract

It is the purpose of the work to develop methods for and present on the computational analyses of advanced III-V photovoltaic devices and their enhancement by the incorporation of semiconductor nanostructures. Such devices are currently being fabricated as part of the research efforts at the Nanopower Research Laboratories; therefore, this work aims to supplement and ground the experimental undertakings with a strong theoretical basis. This is accomplished by numerical calculations based on the detailed balance model and by physics-based device simulation. The specific materials focus of this work is on the enhancement of the GaAs solar cell. The aforementioned methodologies are applied to this device and to distinct enhancement schemes.

The detailed balance formalism is applied to the single-junction solar cell as an introduction leading up to the triple-junction device. A thorough analysis shows how the InGaP-GaAs-Ge triple-junction solar cell may be enhanced by the incorporation of nanostructures. The intermediate band solar cell is introduced as it may be realized by the coupling of a nanostructured array. The detailed balance analysis of this device is performed using the usual blackbody spectrum as well as the more realistic scenarios of illumination by the AM0 and AM1.5 solar spectra. Current research endeavors into placing an InAs quantum dot array in a GaAs solar cell are put into the context of these calculations. It is determined that, although the InAs/GaAs system is not ideal, it does exhibit a significant enhancement in performance over the standard single-junction device.

The evaluation of a commercially available, physics-based, device simulation software package for use in advanced photovoltaics analysis is also performed. The application of this tool on the single-junction GaAs solar cell indicates that the current design used in experimental work is optimized. Recommendations are made, however, in the optimized design of the InGaP-GaAs dual-junction cell. The device simulator is shown to exhibit difficulties in evaluating the complete operation of advanced solar devices; however, the software is used to compute fundamental quantum mechanical variables in a nanostructured solar cell.

Table of Contents

Chapter 1
Introduction

1.1 – Motivation

Solar power has become a topic of great focus in the past several years as the necessity for alternative energy schemes have become increasingly important. Recent reports indicate the global energy consumption to grow from 13 TW-yr currently to as high as 30 TW-yr by the year 2050 [1]. Indeed, nations around the world are quickly accepting the reality of dwindling fossil fuel reserves as well as the reality of global climate change [2, 3]. With approximately 125 PW of solar power striking the Earth at any one time, photovoltaic energy conversion easily lends itself as being a logical approach for the world's energy needs. The aerospace industry also has a vested interest in solar power since it represents a free and readily available source of energy for space applications. Approximately 20-30 % of the total mass and cost of present Earth-orbiting satellites is due to their electric power systems. Improved photovoltaic technology can clearly decrease these figures.

Part of the current research efforts at the Nanopower Research Laboratories focuses on the enhancement of photovoltaic conversion efficiency by the use of low-dimensional nanostructures. Specific to this work, the incorporation of quantum dots in an otherwise conventional III-V photovoltaic device has been proposed as a viable method to increase conversion efficiency [4, 5]. Direct bandgap III-V materials are chosen because they represent the current state-of-the-art in high efficiency photovoltaics [6] and thus may lead the way for the jump from efficiencies barely breaking 20 % for the best commercial silicon cells today to efficiency percentages in the 40's and 50's as promised by the so-called third

generation photovoltaics [7, 8]. Additionally, for space applications, III-V materials and devices have shown an affinity towards increased radiation tolerance [9].

Proper design and fabrication of novel nanostructured photovoltaic devices requires keen knowledge of the underlying physics governing solar cell performance. Fabrication runs are costly and time consuming, so it is beneficial to have a firm theoretical foundation on which to base future work. Therefore, it is the purpose of this work to develop and present methodologies by which novel devices may be computationally analyzed and simulated. Routines are developed to ascertain the limiting performance of novel devices based on detailed balance considerations. Additionally, the use of a commercial device simulator is evaluated for the ability to model devices that are currently being fabricated or are planned to be fabricated. Such analyses provides for an avenue to supplement experimental work in the analysis of nanostructured solar cells.

1.2 – Organization of this Work

The remainder of this chapter gives a brief introduction to the fundamental principles of solar cell device physics necessary to make this work self-contained. A brief discussion on nanostructures and the pertinent physics is also included. This serves as a logical segue into Chapter 2 where the detailed balance analysis of photovoltaic conversion efficiency is introduced. This theory is used to further elaborate on solar cell fundamentals. The theory is then applied to the analysis of multi-junction and intermediate band solar cells. The routines used for this analysis were written in the MATLAB language and are contained in the Appendix.

Chapter 3 evaluates the ability to use the commercially-available Silvaco ATLAS software packing for the physics-based device simulation of novel solar cells. The GaAs single-junction cell and the InGaP-GaAs tandem cell are the focus of this analysis. Additionally, the use of InAs quantum confined regions is explored. An overview of the pertinent device models that were invoked for the device simulations is given. This should allow the reader rapid assimilation into the methodology followed in this work. Pertinent code, written with the ATLAS syntax, is provided in the Appendix.

Chapter 4 gives concluding remarks and summary as well as recommendations for future endeavors to extend this work. Conversational knowledge of device physics [10], solar cell operation [11], quantum mechanics [12], and the physics of the solid state is assumed [13]; knowledge of thermodynamics [14] is beneficial although not absolutely necessary.

1.3 – Solar Cell Fundamentals

The classic design of a solar cell, or photovoltaic device, is by the use of inorganic semiconductor materials. In this sense, the photovoltaic device is essentially a glorified p-n junction diode. The p-n junction is realized by bringing a p-type semiconductor into intimate contact with an n-type semiconductor. From an energy band perspective, the Fermi levels on either side of the junction must equilibrate assuming no external applied bias. This gives rise to the well-known contact, or built-in, potential that causes bending of the conduction and valence bands in the vicinity of the metallurgical junction. The spatial extent of over which this band bending occurs is the so-called space charge, or depletion, region. The energy band diagram of this situation under zero applied bias is displayed in Fig. 1.a.

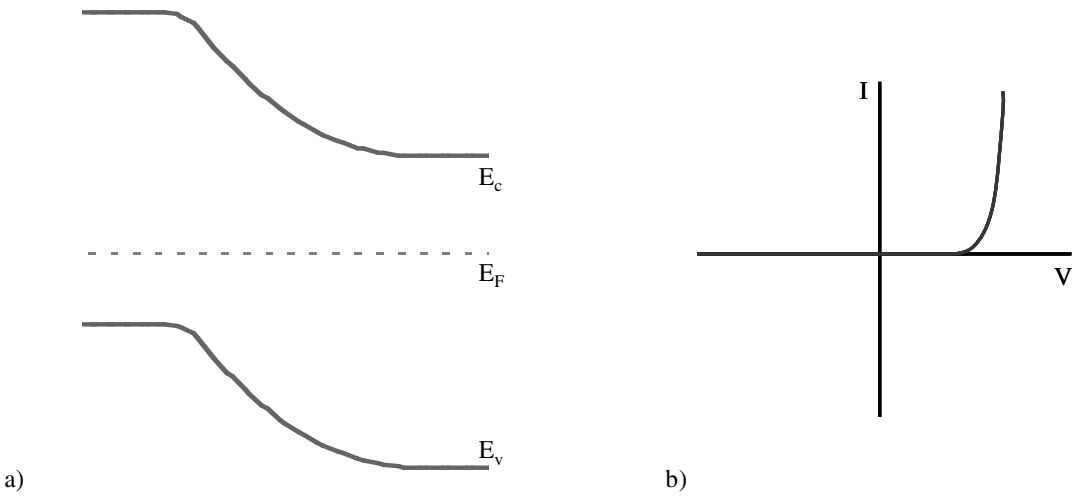

Fig. 1. a) Energy band diagram of the standard p-n junction at equilibrium. b) Current-voltage relation of the ideal diode as given by the Shockley equation.

The operation of an ideal diode is given by the celebrated Shockley equation [15]:

$$I = I_0\left(e^{qV/nkT} - 1\right) \tag{1}$$

which gives the current I though the p-n junction as a function of the applied voltage V; this is the ideal diode law. In the foregoing, I_0 is the reverse bias saturation current, q is the elementary charge, n is the diode ideality factor, k is the Boltzmann constant, and T is the temperature. A representative plot of (1) is drawn in Fig. 1.b; note that for a good device, I_0 tends to be on the order of femto- or picoampères.

When the diode is illuminated by light with photon energy hv such that hv is greater than the semiconductor bandgap, then photon absorption occurs and the diode is perturbed from equilibrium. The band diagram during this event is drawn in Fig. 2.a for zero applied bias. On the p-side of the junction, electrons are pumped from the valence band to the conduction band where they significantly increase the minority carrier population. Similarly, on the n-side of the junction, holes are pumped from the conduction band to the valence band where they significantly increase the minority carrier population. This perturbation from

equilibrium causes a split of the Fermi level into two quasi-Fermi levels, one each for the two carrier types. The splitting of the quasi-Fermi levels causes a small forward voltage to appear across the junction; this is the photovoltaic effect.

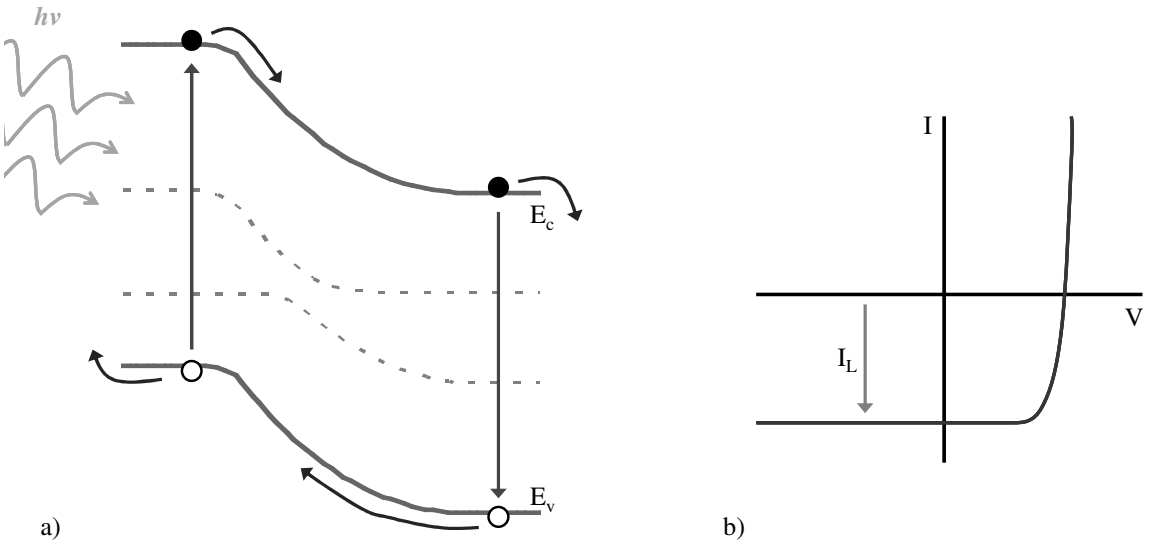

Fig. 2. a) The band diagram of the illuminated p-n junction such that the light has sufficient energy to induce photogeneration of charge carriers. The diagram is drawn for the case of zero applied bias; however, the device is in a non-equilibrium state due to the solar illumination. Photogenerated minority carriers on either side of the junction are swept across by the contact potential leading to a reverse current. b) The current-voltage relation of the illuminated diode. The curve is shifted downward from that of the unilluminated diode by an amount I_L; this is the reverse current at zero bias resulting from minority carrier photogeneration.

At zero applied bias, the increased minority carrier concentrations on either side of the junction causes a reverse current to flow due to the presence of the contact potential; this is implied by Fig. 2.a. The effect is to shift the current-voltage curve in Fig. 1.b downward by an amount I_L. This is indicated in Fig. 2.b. Thus the Shockley equation is modified:

$$I = I_0\left(e^{qV/nkT} - 1\right) - I_L \,. \tag{2}$$

The distinct operational difference between the standard diode and the illuminated cell is that the former only allows operation in either the first or third quadrants (Fig. 1.b) while the latter also adds fourth quadrant operation (Fig. 2.b). Joule's law for electric power is simply

$$P = VI\,. \tag{3}$$

Therefore, fourth quadrant operation distinctly gives rise to negative power, i.e. power is being supplied by the device to the external circuit rather than the device absorbing power. This is the operating mode of the photovoltaic device. Equation (2) is therefore the ideal model of the p-n junction solar cell.

As a matter of convenience, the photovoltaic community prefers to flip the current-voltage plot about the voltage axis so that the fourth quadrant is transferred to the position of the first quadrant as in Fig. 3. This is preferred because the vast majority of photovoltaic analyses occur in the quadrant of power generation. The standard figures of merit for a solar cell are the open-circuit voltage V_{oc}, short-circuit current I_{sc}, maximum power point P_m, efficiency η, and fill factor FF.

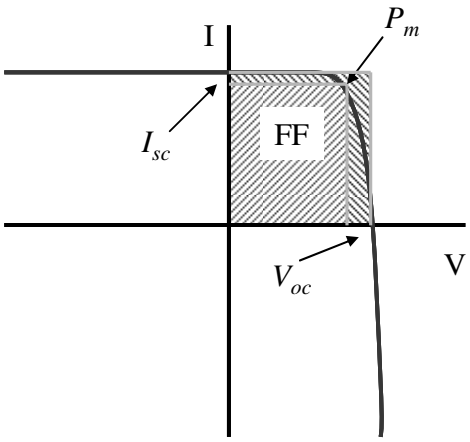

Fig. 3. Standard way of displaying the solar cell current-voltage plot; the power generation section of the I-V curve is placed is the first quadrant for convenient analysis. The standard solar cell device metrics are also displayed.

The short-circuit current I_{sc} is the current that flows at zero applied bias due to the conversion of incident photons. It indicates the amount of current that may be driven through the device. The open-circuit voltage is the applied bias that is necessary to return the device to a quasi-equilibrium, i.e. it is the point at which the current no longer flows even though the device is illuminated.

The maximum power point P_m is the point at which (3) is at a maximum. This is the maximum deliverable power from the solar cell. The ratio of this quantity to the incident power P_{inc} falling upon the cell from the illuminating source gives the solar cell device efficiency

$$\eta = \frac{P_m}{P_{inc}}. \tag{4}$$

This is perhaps the most often cited of the solar cell parameters. Indeed, much of the sought after advancement in the field focuses on the increase of this quantity. Clearly, from Fig. 3, an increase in either I_{sc} or V_{oc} from some reference value would lead to an increase in efficiency.

Then the final device metric is the fill factor:

$$FF = \frac{P_m}{I_{sc}V_{oc}}. \tag{5}$$

This quantity is a measure of the "rectangularity" of the current-voltage relation. It is a useful indicator of the ideality of a solar cell as non-ideal effects, such as intrinsic series resistances or shunt conductances, will tend to skew the current-voltage curve thus diminishing the value of the fill factor. Good solar cells will tend to exhibit fill factor percentages in the mid-80's. From (4) and (5), the efficiency may also be represented as

$$\eta = \frac{I_{sc} V_{ov}}{P_{inc}} FF \, . \tag{6}$$

As will be shown in Chapter 2, the operational response of a solar cell is dependent on the spectrum of light that illuminates the device. In the literature, the sun is often modeled as a 6000 K blackbody. Therefore, it is appropriate to approximate the illuminating spectrum with the blackbody spectrum of a 6000 K body. Realistically though, the sun's temperature varies across the solar disc. Additionally, light originating from the sun will be attenuated by the solar atmosphere. Therefore the blackbody approximation may be questioned.

In the year 2000, the American Society for Testing and Materials (ASTM) developed the AM0 solar spectrum [16]. This is the current standard used by the photovoltaics community to represent the solar spectrum just outside of the Earth's atmosphere. The data was tabulated based on a combination of sources including Earth-based telescopes, high-altitude aircraft, rocket soundings, space shuttle missions, satellites, and solar modeling. The reason for the naming of the spectrum will become apparent.

It is well known that incoming solar radiation is attenuated and scattered by the Earth's atmosphere. These effects are increased for longer optical path lengths traversed through the atmosphere. It is therefore convenient to define a nomenclature, called the air mass number, to account for this. The air mass number is abbreviated as *AMn* where *n* is the relative air mass. The parameter *n* is defined as the secant of the angle subtended by the sun and the local zenith ($n = sec\ \theta$). Therefore, AM1 corresponds to when the sun is directly overhead. This is the minimum possible optical path length introduced by the Earth's atmosphere. By definition, AM0 corresponds to observation from outside the Earth's atmosphere.

The AM0 spectrum, while useful for space-based photovoltaics, overestimates the solar radiance received by terrestrial photovoltaics due to the attenuation and scattering of the Earth's atmosphere. For terrestrial applications, the ASTM standards are the AM1.5-global (AM1.5G) and AM1.5-direct (AM1.5D) solar spectra [16]. The 48.19° angle subtended by the sun for these spectra is, by standard, taken to be the mean location of the sun. These spectra are used by the photovoltaics community for terrestrial based applications. The AM1.5D spectrum accounts for solar radiation as it is received directly from the sun after experiencing loss through the atmosphere. The AM1.5G spectrum adds extra solar radiance to the AM1.5D spectrum to account for additional light received from a 2π steradian field-of-view due to Rayleigh scattering.

The blackbody, AM0, AM1.5G, and AM1.5D spectra are plotted in Fig. 4. These are the usual spectra used in the analysis of photovoltaic devices. The blackbody spectrum is most often used in theoretical analysis. The AM0 spectrum is useful for space-based photovoltaics. The AM1.5G spectrum is often used for non-concentration solar cells while the AM1.5D spectrum is used for concentration devices.

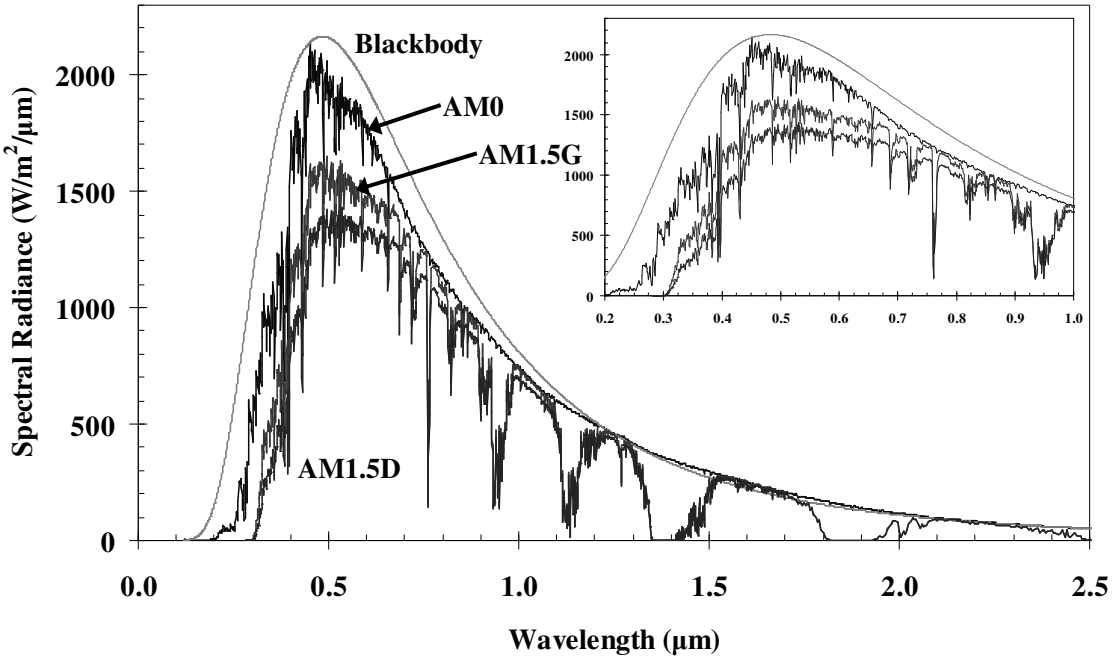

Fig. 5. Comparison of the 6000 K blackbody radiancy with the ASTM solar spectra [16].

1.4 – Nanostructures

A nanostructure can be thought of as some structure that has at least one spatial dimension small enough such that quantum confinement effects become significant. It should be noted that "small" is a relative term and that what may be small enough for one material may very well be too large for another material. Therefore, it is the significance of the quantum effects that determine whether one may call some device structure a nanostructure as it has been defined here.

Perhaps the classic example of a nanostructure is the quantum well. In this example, the material is confined in one spatial dimension while the other two spatial dimensions are of bulk size. One way of realizing such a structure is to grow a thin film of some semiconductor material in-between two other semiconductors of bulk size. This structure is diagramed in Fig. 5.a where the bulk regions are made of the same material which differs

from the quantum well material. Additionally, the quantum well material should exhibit a smaller bandgap than the bulk material; the associated energy band diagram is drawn in Fig. 5.b.

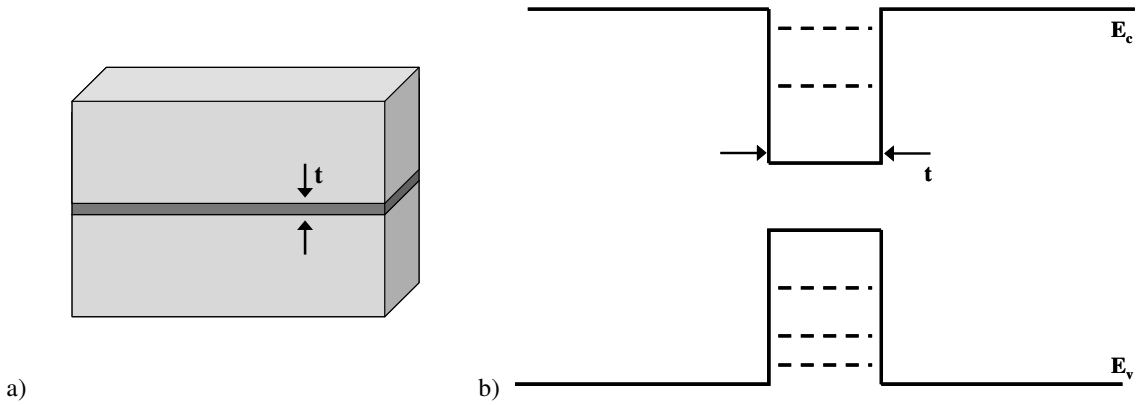

Fig. 5. a) Schematic of a quantum well of thickness *t* dividing a bulk semiconductor of larger bandgap. b) The corresponding energy band diagram. Due to the small value of *t*, quantized energy levels are realized thus making a quantum well.

Referring to Fig. 5, the requirement for a nanostructured quantum well is that the thickness *t* of the well be thin enough for quantization effects to become significant. Usually, this requirement may be observed in the energetics of the system. If *t* is small enough then, as in Fig. 5.b, quantized energy levels will be realized in the well. A consequence of this is that the conduction band minimum and the valence band maximum are no longer realizable states in the quantum well. Instead, the lowest possible energy level in the quantum well for free electrons corresponds with the first quantized eigenstate in the conduction band. Similarly, the highest possible energy level for holes becomes the first quantized eigenstate in the valence band. Following from this discussion, due to the modification of the conduction and valence band ground states, the bandgap of the quantum well is clearly increased to some effective value.

Another low-dimensional nanostructure relevant to this work is the quantum dot. Whereas the quantum well can be thought of as a two-dimensional structure, the quantum dot can be thought of as a zero-dimensional structure. For the quantum dot, all three spatial dimensions are taken to be confined. A single quantum dot placed within a bulk material would exhibit a similar band diagram as in Fig. 5.b. An atomic force micrograph of InAs quantum dots grown atop a GaAs substrate is given in Fig. 6 [71].

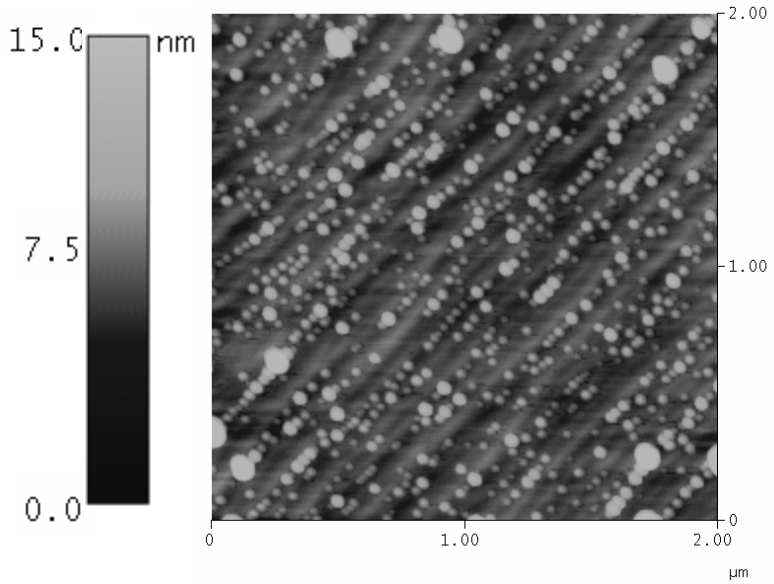

Fig. 6. Atomic force micrograph of 6 nm tall InAs quantum dots epitaxially grown on a GaAs substrate.

The benefit of incorporating nanostructures into solar cells comes due to the superlattice. The superlattice structure is realized by making an array of closely spaced quantum wells [17] or quantum dots; Fig. 7.a shows the energy band diagram for this scheme. If a sufficient amount of wavefunction overlap occurs, i.e. the occurrence of coupling, between adjacent well regions then minibands may form as in Fig. 7.b. These minibands form because the quantum wells or quantum dots form a periodic potential for charge carriers not unlike the periodic potential formed by the crystal lattice. So just as the

crystal lattice induces the formation of the usual energy bands, then the superlattice induces the formation of additional minibands. As implied by Fig. 7.b, the miniband formation may occur within the otherwise forbidden region of the bandgap of the host material. This allows for the standard carrier phenomena to now occur in regions previously inaccessible. Namely, as it is of the utmost importance in the field of photovoltaics, additional photon absorption processes become possible with the introduction of the minibands. This concept plays an important role the discussions to follow.

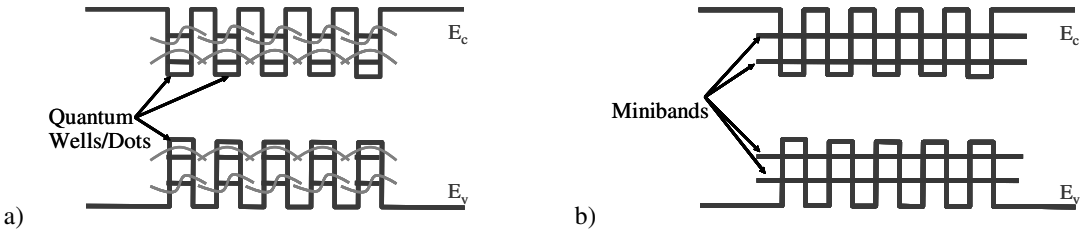

Fig. 7. a) Energy band diagram of an array of quantum wells or quantum dots. The eigenfunction are superimposed over the quantized energy levels. If sufficient coupling, i.e. overlap of wavefunctions, occurs between adjacent well regions then b) miniband formation will result.

Chapter 2

Detailed Balance Models

2.1 – General Theory

The treatment of solar energy conversion by a p-n junction presented by Shockley and Queisser [18] represents the fundamental limits attainable by semiconductor solar cells. This formulation accounts for the blackbody properties of the solar cell and invokes the principle of detailed balance to derive an expression for the operation of a solar cell at the fundamental limit. The theory easily propagates through for use in the analysis of advanced photovoltaic designs and thus serves as the basis for continued research in the field.

Planck's law for blackbody radiation [19], expressed as a photon flux per unit energy flowing out of a blackbody cavity, is

$$\frac{d\Phi}{dE} = \frac{2\pi E^2}{h^3 c^2} \frac{1}{e^{E/kT} - 1} \tag{1}$$

where E is the energy, h is Planck's constant, c is the speed of light, k is Boltzmann's constant, and T is the temperature of the blackbody. In this work, (1) shall be known as the spectral photon flux. Integration of this equation through some energy interval gives the photon flux Φ. Treating the sun as an ideal blackbody, and since the solar absorption of a semiconductor is limited by the bandgap energy E_g, the solar flux that is actually absorbable is

$$\Phi_s\left(E_g, \infty\right) = \int_{E_g}^{\infty} dE \left.\frac{d\Phi}{dE}\right|_{T=T_s} \tag{2}$$

where T_s is the temperature of the sun. Actually, since (1) represents the spectral flux flowing out of the cavity, then (2) represents the absorbed flux at the sun's surface. For the common sun-solar cell system, the solar cell is located near Earth and impingent radiation on the device takes the form of plane waves incident on a planar absorber. Therefore the photon flux absorbed by the solar cell is actually decreased by a factor of

$$f_s = \Omega / \pi \tag{3}$$

where Ω is the solid angle subtended by the sun and the factor of π^{-1} accounts for plane waves impingent on a planar surface [18]. A currently accepted standard value for f_s is 2.1646×10^{-5} [8].

Similarly, the solar cell may be treated as an ideal blackbody at some temperature T_c. Then at thermodynamic equilibrium, the direct recombination of electron-hole pairs gives rises to photon emission with a flux given by

$$\Phi_c\left(E_g,\infty\right) = \int_{E_g}^{\infty} dE \left.\frac{d\Phi}{dE}\right|_{T=T_c} . \tag{4}$$

When perturbed from equilibrium by an applied bias V, the p-n junction will see an increase in radiative recombination proportional to the Boltzmann factor [15, 20]; the expression for radiative recombination is thus given as

$$U = A\Phi_c e^{qV/kT_c} \tag{5}$$

where A is the surface area of the device and q is the elementary charge. Note that the quantity qV is equal to the amount of splitting in the quasi-Fermi levels [15, 18]. Similarly, the recombination rate due to non-radiative transitions is [15, 20]:

$$R = R_0 e^{qV/kT_c} \tag{6}$$

where R_0 is the thermal generation rate. Finally, it is convenient to introduce the inverse of the fraction of the amount of the recombination-generation current that is due to radiative transitions:

$$f_c = \left\{ \frac{A\Phi_c}{A\Phi_c + R_0} \right\}^{-1}. \tag{7}$$

The principle of detailed balance states that, at equilibrium, a time-rate process must be balanced by its inverse; therefore the process and its inverse must proceed at equal rates [21]. Applied to a photovoltaic device, the principle of detailed balance implies that the sum of the time-variances of the electron-hole pair populations must vanish; thus [18]:

$$\begin{aligned} 0 &= Af_s\Phi_s - U + R_0 - R - I/q \\ &= Af_s\Phi_s - A\Phi_c + \left(A\Phi_c - U + R_0 - R\right) - I/q \end{aligned} \tag{8}$$

where I is the current. The term in parentheses is the net generation rate of electron hole pairs when the device is at thermal equilibrium with its surroundings. Substituting the quantity $(A\Phi_c - R_0)$ by (7) into (8) and solving for I yields the expression for the current density of the solar cell:

$$\frac{J}{q} = \left(f_s\Phi_s - \Phi_c\right) - f_c\Phi_c\left(e^{qV/kT_c} - 1\right). \tag{9}$$

It is instructive to compare this result with the photovoltaic form of the Shockley equation [10-11]:

$$I = I_{sc} - I_0\left(e^{qV/kT} - 1\right) \tag{10}$$

where I_{sc} is the short-circuit current and I_0 is the reverse bias saturation current. It is evident that the first term in parentheses in (9) is the short circuit current while the quantity $f_c^{-1}\Phi_c$ is the saturation current. Equation (9) is the fundamental result of the detailed balance

formulation; it is an integral solution that directly gives the current-voltage characteristics of a solar cell. From it, the solar conversion efficiency can be directly extracted.

Although the foregoing theory is thermodynamic by the invocation of the Planck distribution and the principle of detailed balance, no thermodynamics has actually been applied directly to the quantum electronics at play; i.e. the thermodynamics of the electron-photon interaction is not completely considered. By the definition of the chemical potential μ:

$$dE = \mu dN \,, \tag{11}$$

the chemical potential of photons has been considered to be zero since the conservation of photon number N is not required. The notion of a vanishing chemical potential is actually correct for thermal radiation; hence the Planck law. The argument, however, is not compelling in general since photon-photon interaction is non-existent; therefore photons equilibrate by means of atomic interactions that give rise to the possibility of a non-zero chemical potential [22]. Luminescent photon emission, i.e. photon emission due to some other means than thermal, can be shown to exhibit a non-zero chemical potential. This is due to the fact that luminescent radiation is observed to have a threshold frequency, i.e. energy, below which no light emission occurs. Therefore, the presence of a non-zero chemical potential can be thought of as a consequence of this high-pass energy gap. A thorough thermodynamic formulation based on these principles leads to a generalization of (1) [22]:

$$\frac{d\Phi}{dE} = \frac{2\pi E^2}{h^3 c^2} \frac{1}{e^{(E-\mu)/kT} - 1} \,. \tag{12}$$

This formula gives the spectral photon flux exiting from a blackbody cavity; it contains the effects of both blackbody and luminescent radiation. In the limit of a vanishing chemical potential, (12) reduces to the conventional form of the Planck distribution.

The derivation leading to the Shockley-Queisser result can be claimed to be semi-empirical in that the assumptions invoked in (5)-(8) come from inserting blackbody properties in such a way that fits the rectifier model. With the result of (12) and invoking the principles of statistical mechanics, the Shockley-Queisser result is superseded [23-25]:

$$\frac{J}{q} = f_s \Phi_s + (f_c - f_s)\Phi_c - f_c \int_{E_g}^{\infty} dE \left. \frac{d\Phi}{dE} \right|_{T=T_c} , \tag{13}$$

where the spectral flux in the last term is given by the generalized Planck distribution in (12) and where it turns out that the chemical potential of luminescent photons is equivalent to the applied bias:

$$\mu = qV . \tag{14}$$

It should be noted that, except for extreme cases and novel design schemes, both (9) and (13) give almost identical results. Equation (13) has the reassuring property that at the short-circuit condition ($V = 0$), if the solar cell and the sun were at thermal equilibrium, then no current would flow; this is generally lacking from (9).

To compare (9) and (13), the current-voltage results for a 1.46 eV bandgap semiconductor are plotted in Fig. 1.a. The cell is illuminated by a 6000 K blackbody at one-sun and 1000-sun concentrations; f_c is taken to be unity and the cell is at a temperature of 300 K. In Fig. 1.a, there are actually two sets of curves for each concentration level corresponding to either (9) or (13); however, these curves overlap and are not individually visible. The relative error of using (9) instead of (13) is plotted for the two concentration levels in Fig. 1.b. From this plot, it is clear that maximum error occurs at the open-circuit voltage and increases as the open-circuit voltage increases. Note that the data in Fig. 1.b is only plotted for voltages greater than ~0.9 V for the one-sun case and greater than ~1 V for

the 1000-sun case. This is because any error corresponding to smaller voltage values are smaller than the numerical machine precision. Note that the models discussed above require the integration of Bose-Einstein distributions. Care must be taken in handling these functions as singularities are not uncommon. The method used herein makes use of a Gauss-Kronrod quadrature method [26].

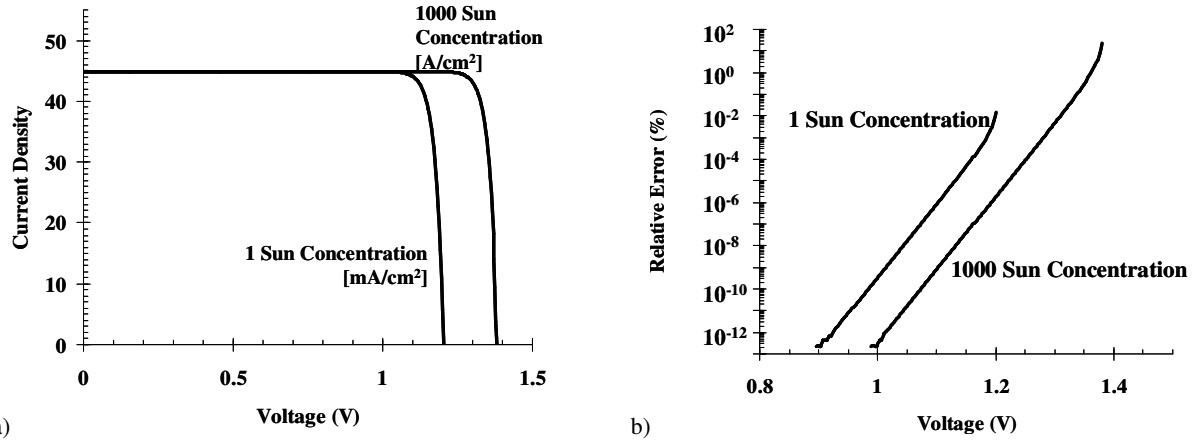

Fig. 1. a) Detailed balance model using the original (9) and statistical (13) formulations at two different concentration levels (E_g = *1.46 eV*). The curves corresponding to the different formulations overlap at both concentrations. b) Relative errors at both concentration levels of using (9) instead of (13).

The plot in Fig. 2 shows the 1000-sun case but at an elevated device temperature of 600 K. As with the foregoing case, the I-V curves corresponding to (9) and (13) overlap enough to not be individually resolvable. In comparison to Fig 1.b, the relative error of using (9) instead of (13) is significantly increased although not to the point to cause great deviation between the results of the two models. Even though the maximum error is somewhat large (~100 %), this occurs at a point where the current levels are very small and vary exponentially. It is clear from Figs. 1-2 that at normal operating conditions either use of (9) or (13) will suffice. Although this is the case, the remainder of this work will concentrate on

the expression in (13) to make sure the results follow from the soundest physical grounds possible. This is also important for the advanced designs to be considered.

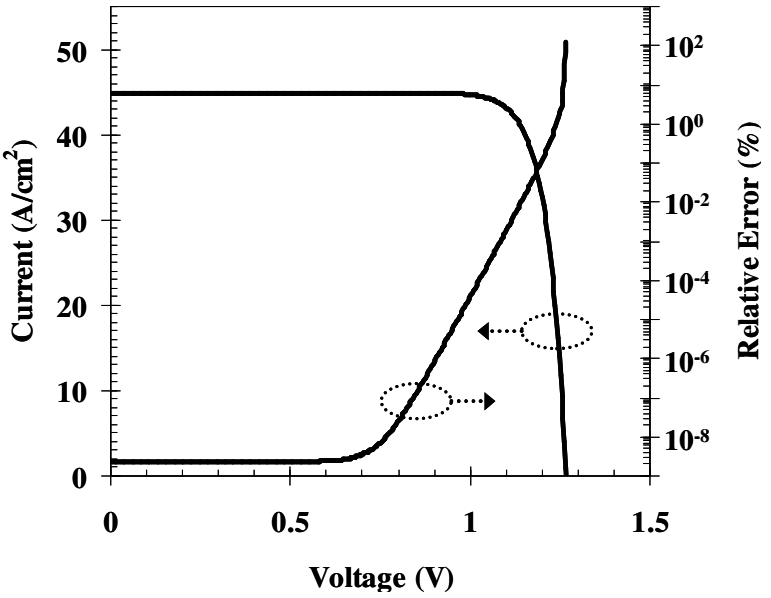

Fig. 2. Detailed balance model using the original (9) and statistical (13) formulations at 1000-sun concentration and at an elevated device temperature of 600 K (E_g = *1.46 eV*). The curves corresponding to the different formulations overlap at both concentrations but the relative error is significantly increased from the corresponding plots in Fig. 1.

2.2 – Single-Junction Solar Cell

In simulating the detailed balance limits of a solar cell, it is common to take the temperature of the sun to be 6000 K and that of the device to be 300 K. The regime of interest is the radiative limit, i.e. $f_c = 1$. At this limit, it is possible to analyze the maximum possible performance of a photovoltaic device without having to consider the confounding of non-idealities brought about by materials growth, device design, etc. Additionally, the geometric parameter f_s has been previously defined to be equal to 2.1646×10^{-5} [8]. This implies that the maximum possible concentration factor is 46,198 suns. Thus the product of f_s

and the maximum concentration factor is unity therefore corresponding to the equivalent case of a solar cell placed at the suns surface.

The detailed balance performance of several of the elemental and binary semiconductors is plotted in Fig. 3 as a set of I-V characteristics. By inputting each individual material's bandgap into the detailed balance model, the fundamental limiting performance is determined. This figure helps to illustrate the tradeoffs inherent in materials selection. The smaller bandgap semiconductors allow for a larger short-circuit current because they are able to absorb a larger portion of the solar spectrum; however, their small bandgap places a fundamental limit on the open-circuit voltage. Therefore it makes sense that there will be an optimum bandgap such that the corresponding I-V characteristic gives the maximum attainable efficiency. As discussed in Section 1.3, the efficiency is defined as the ratio of the maximum power to the irradiance falling upon the solar cell form the sun. In this blackbody analysis, the irradiance P_s is determined by the Stefan-Boltzmann law:

$$P_s = \sigma T^4; \tag{15}$$

which gives a solar constant of 1590.7 W/m^2 when including a prefactor of f_s. σ is the Stefan-Boltzmann constant.

The issue of determining an optimum bandgap corresponding to maximum attainable efficiency is addressed in Fig. 4. Here, the detailed balance efficiency limits are plotted as a function of material bandgap at several different solar concentrations. For each curve, a maximum occurs indicating the optimum bandgap leading to maximized solar efficiency. This plot directly gives the detailed balance limit of 31.0 % efficiency corresponding to a bandgap of 1.31 eV at one sun illumination. For maximum concentration, the detailed balance limit rises to 40.8 % efficiency corresponding to a decreased bandgap of 1.11 eV.

For perspective, the bandgaps of several of the elemental and binary semiconductors are included in Fig. 4.

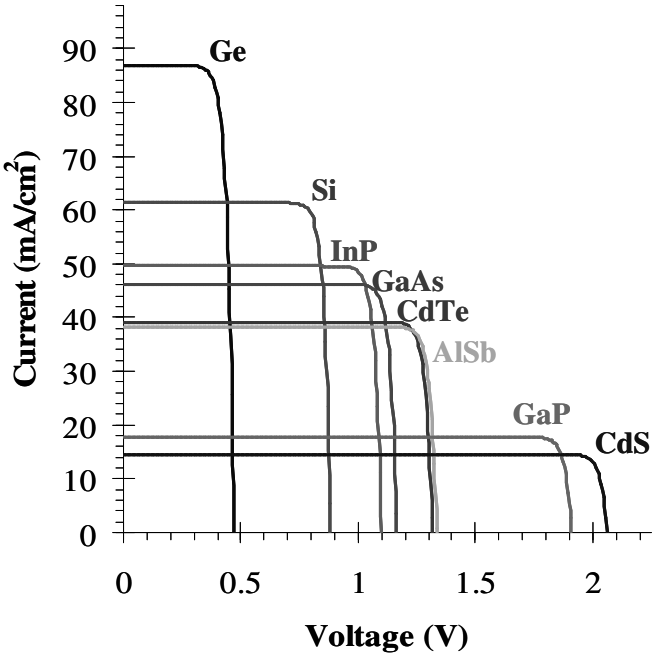

Fig. 3. Electrical characteristics of several semiconductors operating at the detailed balance limit. Larger bandgap materials exhibit larger open circuit voltages but smaller short circuit currents.

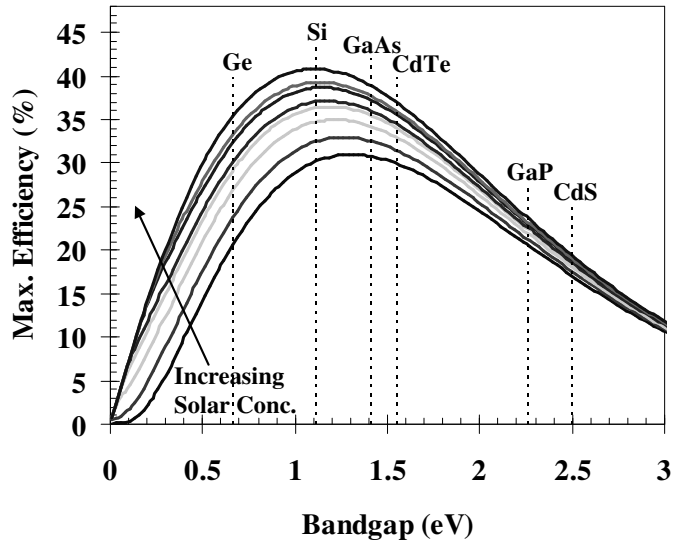

Fig. 4. Detailed balance efficiency limits plotted as a function of material bandgap at solar concentration factors of 1, 10, 100, 518, 1000, 5180, 10000, and 46198.

Although the treatment of the sun as a perfect blackbody in the foregoing discussions provides for an excellent approximation in the analysis for solar efficiency, it is of interest to study the same scenarios but with a more accurate model of the solar flux. This is made possible by the existence of standard data detailing the actual solar spectrum outside the Earth's atmosphere and on its surface [16]. The AM0 and AM1.5 solar spectra were discussed in Section 1.3 and are compared with the 6000 K blackbody spectrum in Fig. 5.

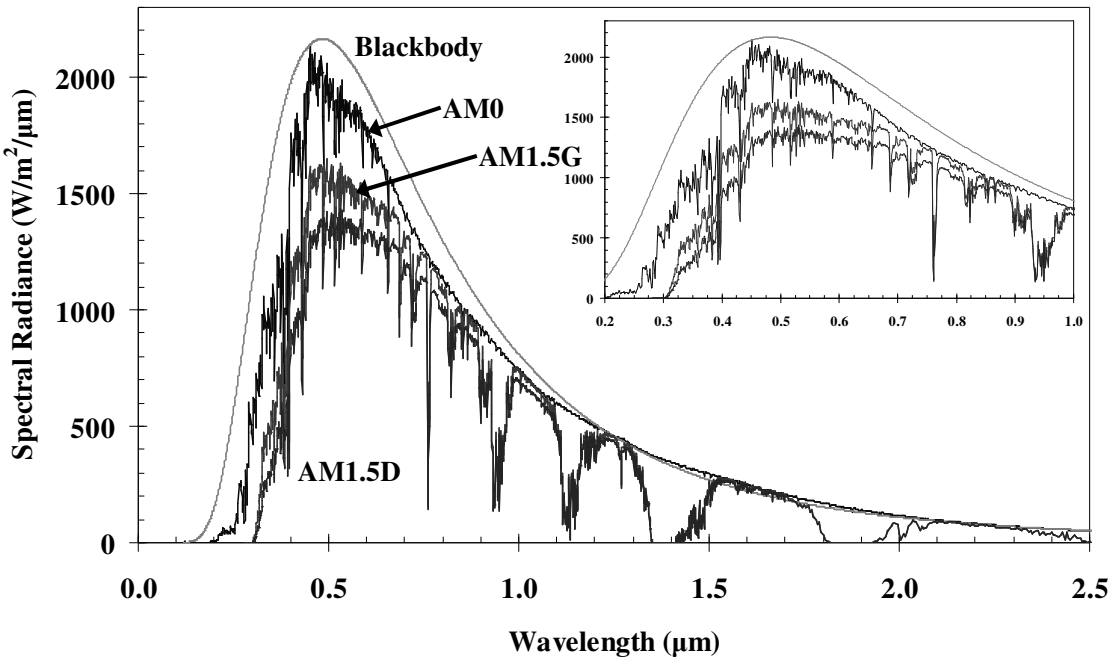

Fig. 5. Comparison of the 6000 K blackbody radiancy with the ASTM solar spectra [16]. The Planck law used to generate the blackbody curve includes f_s as a prefactor.

The blackbody curve in Fig. 5 is the Planck distribution (1) multiplied by f_s and expressed as a spectral radiance. For more realistic modeling of detailed balance performance, the actual solar spectra may be invoked instead of the Planck distribution. Therefore the data plotted in Fig. 5, expressed as a spectral photon flux, may be used directly to determine the absorbed photon flux by quadrature of (2); the remainder of the process to

simulate detailed balance performance remains the same. This method allows for the generation of the plots in Fig. 6 showing the detailed balance efficiency limits vs. material bandgap under either AM0 or AM1.5 illumination.

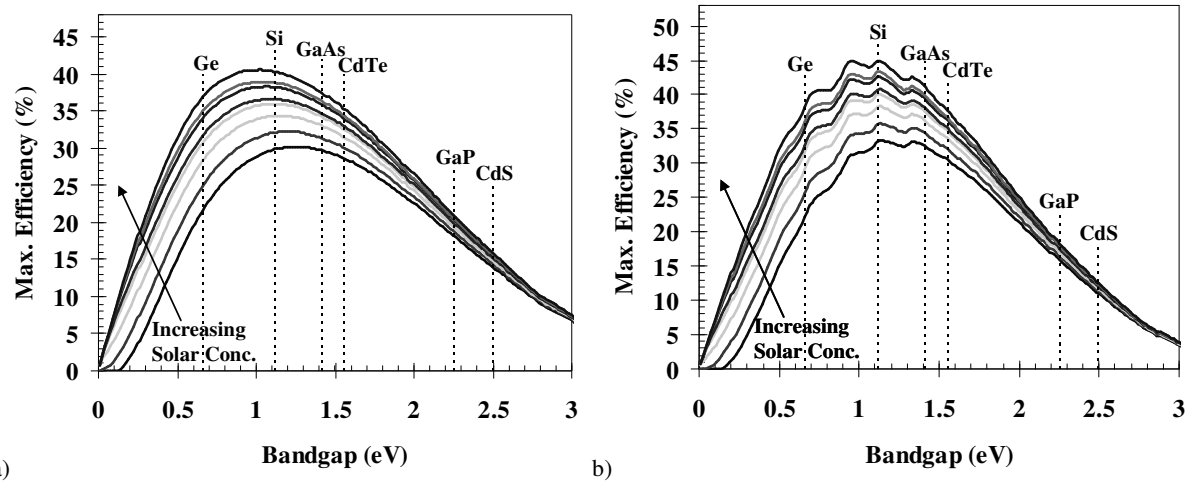

Fig. 6. Detailed balance efficiency limits plotted as a function of material bandgap at solar concentration factors of 1, 10, 100, 518, 1000, 5180, 10000, and 46198. The illumination used is a) the AM0 solar spectrum and b) the AM1.5G spectrum for the one-sun case and the AM1.5D spectrum for the rest.

The AM0 case in Fig. 6.a is similar to the blackbody case in Fig. 4. This is due to the similarity between the blackbody and AM0 spectra. Although the AM0 spectrum is not a smooth function, the attenuation lines are rather narrow and do not have the same effect on the analysis as the irregularity of the AM1.5 spectra. The AM1.5 case in Fig. 6.b is noticeably different than the blackbody and AM0 cases by the presence of several local maxima. As alluded to, this structure in the AM1.5 case is attributable to the occurrence of relatively large attenuation bands in the AM1.5 spectra. For comparative purposes, the three cases are plotted together in Fig. 7 at one-sun and maximum concentrations. Note that the larger peak efficiencies for the AM1.5 cases are due to smaller value of the solar constants (AM1.5G: 1000.4 W/m^2, AM1.5D: 900.14 W/m^2) corresponding to these spectra.

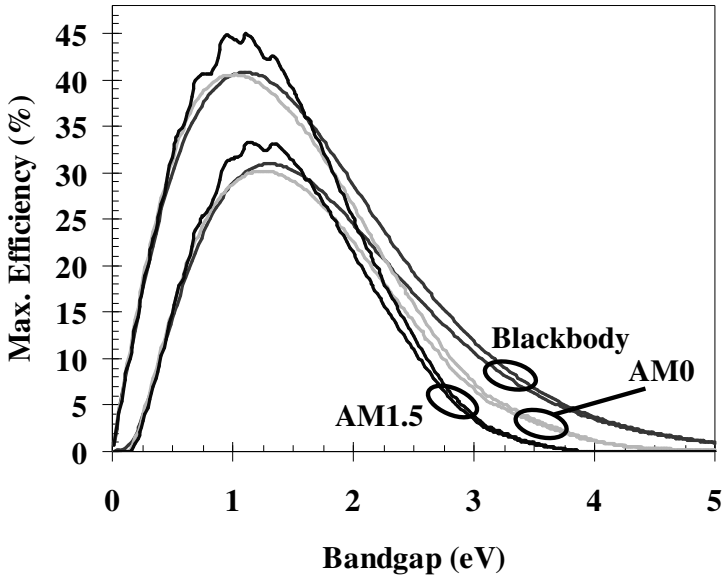

Fig. 7. Comparison of the maximum efficiencies attainable under the detailed balance limit for the three different spectra at one-sun and maximum concentrations. AM1.5G is used for the one-sun case while AM1.5D is used for the maximum concentration case.

From Fig. 7, the detailed balance efficiency limits are summarized in Table I with their respective optimum bandgaps at one-sun and maximum concentrations for the three standard spectra. AM1.5G is used at one-sun while AM1.5D is used at maximum concentration. Plots of this data taken over the entire concentration range are displayed in Fig. 8. These sets of data clearly indicate very different design spaces based on the spectrum of interest. What is an optimum design point under one spectrum is not, in general, an optimum design point under another spectrum. The data in Fig. 8.b is particularly of interest as it indicates a major difference in the analysis using a blackbody spectrum compared to that using an actual spectrum. For the blackbody case, the optimum bandgap, i.e. the design space, follows a logarithmically dependent continuum. For either the AM0 or AM1.5 cases, the optimum bandgap remains relatively constant throughout large ranges of solar concentrations and exhibits step discontinuities at several points. This is attributable to the

irregular roughness of the actual spectra compared to the smoothness of the blackbody spectrum (Fig. 5). It should be noted that, as seen in Fig. 6.b, the maximum efficiency as a function of bandgap for the AM1.5 spectrum exhibits several local maxima. The data used to generate Fig. 8.b considers only the global maximum. Note that in Fig. 6.b, the global maximum eventually shifts from one local maximum to another with increased concentration. This contributes to the relative consistency of the optimum bandgap for the AM1.5 spectrum.

Table I

Detailed Balance Efficiency Limits

	No Concentration		Max. Concentration	
Illumination Spectrum	**Opt. Bandgap**	**Max. Efficiency**	**Opt. Bandgap**	**Max. Efficiency**
Blackbody	1.31 eV	31.0 %	1.11 eV	40.8 %
AM0	1.26 eV	30.2 %	1.03 eV	40.6 %
AM1.5	1.12 eV	33.2 %	1.11 eV	45.0 %

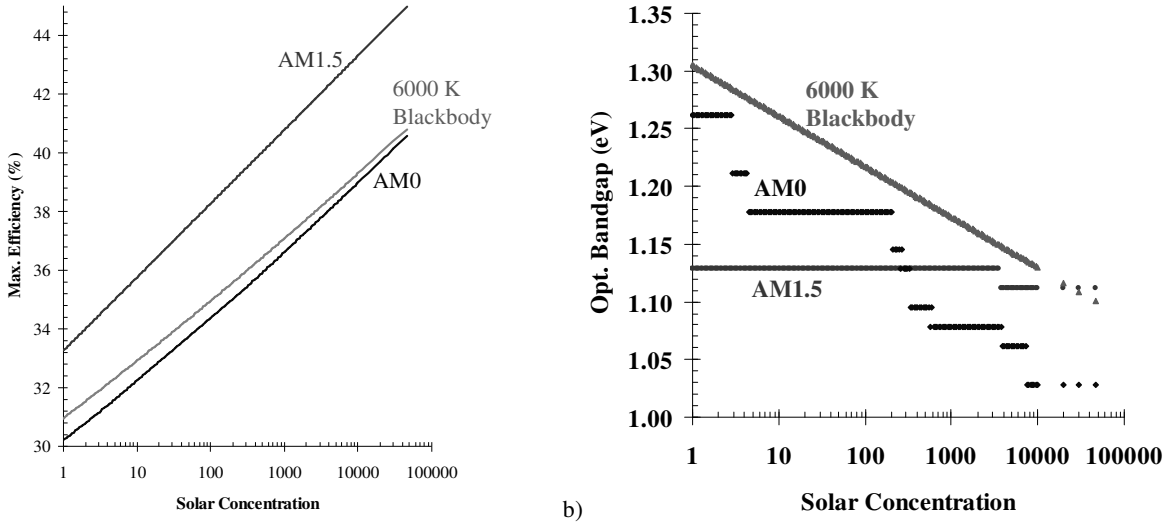

Fig. 8. Comparison between the three standard spectra of a) maximum efficiency and b) corresponding optimum bandgap throughout the range of solar concentrations. This indicates vastly different device design spaces depending on the spectrum of interest.

2.3 – Triple-Junction Solar Cell

From the discussions in the forgoing section, it is clear that the material bandgap plays an essential role in determining the performance of a solar cell. In Fig. 3, this is manifested as different materials exhibiting different open-circuit voltages and different short-circuit currents. Clearly, any single device exhibited in Fig. 3 would be made more efficient simply by extending the I-V curve such that a larger open-circuit voltage is attained. This is the general idea behind the multi-junction solar cell.

As a specific case of the multi-junction solar cell, a triple-junction device is diagramed in Fig. 9.a; this is the InGaP-GaAs-Ge triple junction cell and represents the state-of-the-art in basic multi-junction approaches. This device is grown monolithically by epitaxial means. The materials are chosen to conform to the constraint of lattice matching. In this device, there are actually three separate p-n junctions, each composed of a different material. This constitutes an equivalent circuit of three solar cells connected in series as seen in Fig. 9.b. The materials are placed such that the one with the largest bandgap is located at the top of the stack; the remaining materials follow the trend of decreasing bandgap towards the bottom of the stack. This design allows for the most efficient conversion of higher energy photons by the top cell. The top cell is transparent to sub-bandgap light; this light is then absorbed by one of the remaining cells underneath. This allows for the splitting of the absorption of the solar spectrum into more efficient means; this is diagramed in Fig. 10. Efficiency of this device is enhanced from the single-junction cell due to the photogeneration occurring over several junctions at once. In general, a separate photovoltage will be dropped across each junction at any given time; these voltages add giving the total voltage across the multi-junction device. This is the mechanism which leads to an increased open-circuit

voltage, i.e. the I-V curve is stretched along the voltage axis. The only caveat is that the current will be limited to the lowest output due to the constraint of current matching, i.e. the conservation of charge dictates that the currents running through each junction must be equal. Finally, it should be noted that an actual device will include a backwards connected tunnel junction in-between each sub-cell to properly drive current (this is discussed in further detail in Section 3.18). This reality is not necessary in the analysis that follows thus it suffices to assume that an ideal short exists between each sub-cell as drawn in Fig. 9.b.

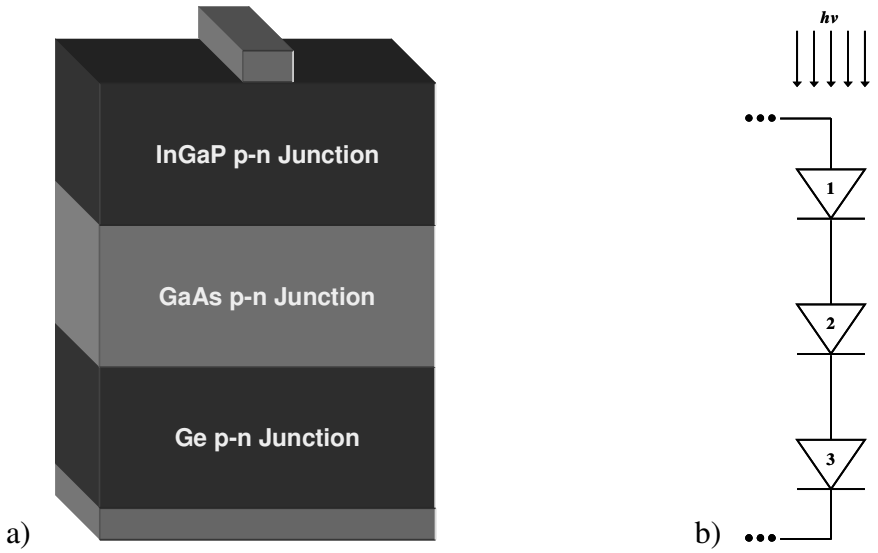

Fig. 9. InGaP-GaAs-Ge triple-junction solar cell a) diagramed to show the proper placement of each layer such that the smallest bandgap material is placed at the bottom with increasing bandgaps towards the top of the stack. The device is b) diagramed as an equivalent circuit with three individual solar cells connected in series representing each of the individual junctions.

A detailed balance analysis of the triple-junction cell in Fig. 9.a. has been previously reported [27]. The remainder of this section elucidates on the mathematical details necessary to perform such an analysis and verifies the published results. Additionally, the solutions obtained in this section give insight to the detailed analysis to follow in Section 2.4 on the intermediate band solar cell.

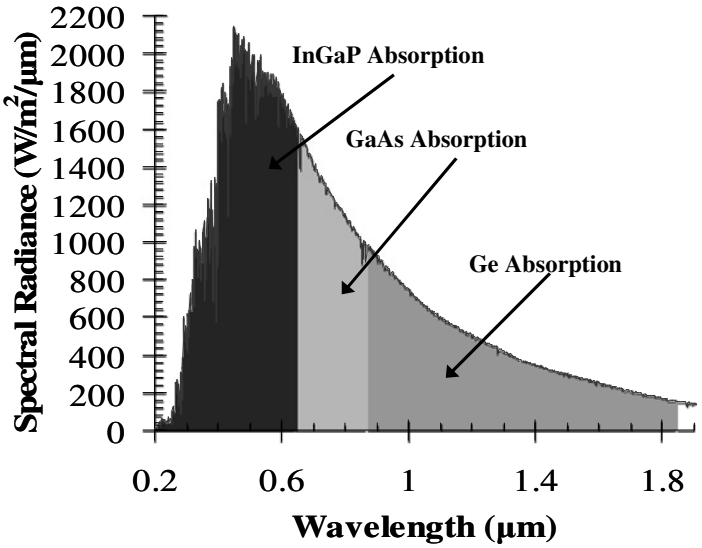

Fig. 10. AM0 solar spectrum split into separate absorption regions corresponding each of the sub-cells in the triple-junction InGaP-GaAs-Ge stack.

The task at hand is to determine the efficiency of the InGaP-GaAs-Ge triple-junction solar cell and to determine which layers should be modified to increase this efficiency. In referencing to Fig. 9.b, the current through cell n, where n runs from 1 to 3, is given by (13). As in the single-junction example, f_c may be taken to be unity. Additionally, the middle term in (13) is only significant as the temperature of the device approaches that of the illuminating body; therefore, it may be ignored. Explicitly, the current through cell n is then

$$J_n = J_{Ln} - J_{Dn} = f_s \frac{2\pi q}{h^3 c^2} \int_{\overline{E}_n} \frac{E^2 dE}{e^{E/kT_s} - 1} - \frac{2\pi q}{h^3 c^2} \int_{\overline{E}_n} \frac{E^2 dE}{e^{(E-\mu_n)/kT_c} - 1} \tag{16}$$

where the first term can be considered to be the short-circuit current J_L of the single-junction cell and the second term can be considered to be the dark current J_D. By (14), μ_n is determined from the voltage that is dropped across cell n. The integrations in (16) are performed over the energy interval ranging from the bandgap of the specified sub-cell up to the bandgap of the next sub-cell such that there is no overlap in the integrated energy ranges of any two sub-cells. Referring to Fig. 9.b, the energy intervals are

$$\begin{aligned}\overline{E}_1 &= [E_{g1}, \infty) \\ \overline{E}_2 &= [E_{g2}, E_{g1}] \\ \overline{E}_3 &= [E_{g3}, E_{g2}]\end{aligned} \tag{17}$$

recalling that the multi-junction design requires that $E_{g1} > E_{g2} > E_{g3}$.

The power of the stack is then

$$P = VJ_n \tag{18}$$

where V is the voltage dropped across the entire stack. In principle, since the currents throughout each sub-cell are equal, any value of n may be chosen. Arbitrarily choosing $n = 1$ and due to the direct relationship between voltage and the chemical potential given by (14), the power may be rewritten as

$$P = J_1 \sum_n \frac{\mu_n}{q}. \tag{19}$$

The condition for maximum power, thus giving cell efficiency, is met by maximizing this expression with respect to the chemical potentials but subject to the following constraints:

$$\begin{aligned}\Phi_1 &= \frac{1}{q}(J_1 - J_2) = 0 \\ \Phi_2 &= \frac{1}{q}(J_2 - J_3) = 0\end{aligned} \tag{20}$$

where the factor of q^{-1} has been placed for convenience. Then by the method of Lagrange multipliers, the maximization of (19) is determined by solving the following:

$$\nabla_\mu P + \lambda_1 \nabla_\mu \Phi_1 + \lambda_2 \nabla_\mu \Phi_2 = 0 \tag{21}$$

where λ are the Lagrange multipliers.

Expanding the pertinent gradients,

$$\nabla_\mu P = \frac{1}{q}\begin{pmatrix} J_1 & J_1 & J_1 \end{pmatrix} + \frac{1}{q}\begin{pmatrix} \frac{dJ_1}{d\mu_1} & 0 & 0 \end{pmatrix}\sum_n \mu_n$$
$$\nabla_\mu \Phi_1 = \frac{1}{q}\begin{pmatrix} \frac{dJ_1}{d\mu_1} & -\frac{dJ_2}{d\mu_2} & 0 \end{pmatrix} \tag{22}$$
$$\nabla_\mu \Phi_2 = \frac{1}{q}\begin{pmatrix} 0 & \frac{dJ_2}{d\mu_2} & -\frac{dJ_3}{d\mu_3} \end{pmatrix},$$

allows for (21) to be written as a set of simultaneous equations:

$$\begin{aligned} \left(\sum_n \mu_n\right)\frac{dJ_1}{d\mu_1} + J_1 + \lambda_1\frac{dJ_1}{d\mu_1} &= 0 \\ J_1 - \lambda_1\frac{dJ_2}{d\mu_2} + \lambda_2\frac{dJ_2}{d\mu_2} &= 0 \\ J_1 - \lambda_2\frac{dJ_3}{d\mu_3} &= 0 \end{aligned} \tag{23}$$

Therefore, the solution is

$$\sum_n \left(\mu_n + \frac{J_1}{dJ_n/d\mu_n}\right) = 0\,. \tag{24}$$

This gives the operating condition of the multi-junction cell at which maximum power is achieved. All that remains is to evaluate the derivative occurring in (24):

$$\begin{aligned} \frac{dJ_n}{d\mu_n} &= -\frac{dJ_{Dn}}{d\mu_n} \\ &= -\frac{2\pi q}{h^3c^2}\frac{1}{kT_c}\int_{\overline{E}_n}\frac{E^2 e^{(E-\mu_n)/kT_c}dE}{\left(e^{(E-\mu_n)/kT_c}-1\right)^2} \\ &= -\frac{2\pi q}{h^3c^2}\frac{1}{4kT_c}\int_{\overline{E}_n} E^2\,\mathrm{csch}^2\left(\frac{E-\mu_n}{2kT_c}\right)dE \end{aligned} \tag{25}$$

It should be noted that even though the example of a triple-junction cell has been chosen for this derivation, the solution may be generalized for any number of *N* sub-cells. This would increase the number of constraints in (20) to a total number of *N-1* with the general form

$$\Phi_n = \frac{1}{q}\left(J_n - J_{n+1}\right) = 0 \tag{26}$$

where *n* ranges from 1 to *N-1*. Then (21) through (23) would be modified accordingly leading to the same result in (24). Therefore, (24) is general for any given number of junctions in the multi-junction stack.

The operating condition for maximum power is given by (24); this is the fundamental equation. To numerically determine the efficiency of a multi-junction stack, the chemical potentials may be varied iteratively until (24) is satisfied. The bandgaps of InGaP, GaAs, and Ge are 1.89 eV, 1.42 eV, and 0.66 eV, respectively. Using these parameters in the model discussed yields a detailed balance efficiency limit of 33.5 % for the triple-junction cell. Holding the bottom cell bandgap constant at 0.66 eV, but allowing the remaining sub-cells to vary in bandgap yields the efficiency contours plotted in Fig. 11. This plot shows that dramatic improvement may be made to the triple-junction cell by lowering the bandgap of the GaAs sub-cell.

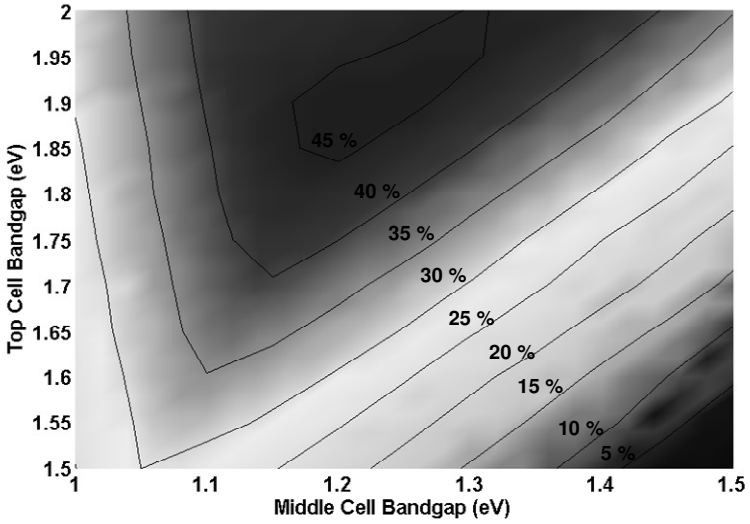

Fig. 11. Efficiency contours of the triple-junction solar cell with variable top and middle cell bandgaps; the bottom cell bandgap fixed to 0.66 eV (germanium).

From Fig. 11, with a top cell bandgap of 1.89 eV (InGaP) and a middle cell bandgap of 1.42 eV (GaAs), the detailed balance efficiency limit of the triple-junction cell is 33.5 %. By decreasing only the middle cell bandgap to 1.20 eV, the detailed balance limit is increased to the maximum point at 47.5 %. The problem that arises is that no material exists that both has this desired bandgap and is latticed matched to InGaP and Ge. As discussed in Section 1.4, the incorporation of a nanostructured array in a host material may induce miniband formation. This can therefore give rise to otherwise sub-bandgap photoconversion of light. A quantum well or quantum dot array placed in the GaAs middle cell may therefore induce an effective bandgap lowering such that the overall triple-junction efficiency limit increases from 33.5 % to 47.5 %.

2.4 – Intermediate Band Solar Cell

The present concept of the intermediate band solar cell was first reported by Luque and Martí [28] while an earlier, related concept was reported by Wolf [29]. The standard concept of the intermediate band solar cell is shown schematically in Fig. 12 as a semiconductor band diagram where the bandgap is represented by $E_{CV} = E_C - E_V$. The standard solar cell would therefore only be able to absorb photons with energy equal to or greater than E_{CV}. Suppose now that an accessible band is located at an intermediate level E_I between E_C and E_V as indicated in Fig. 12. This intermediate band is simply the miniband discussed in Section 1.4. The electronic states in the intermediate band should be accessible via direct transitions. Then the absorption of photon energy E_{IV} will pump an electron from the valence band to the intermediate band. A subsequent photon of energy E_{CI} then pumps an electron from the intermediate band to the conduction band. The increased performance of

this design in comparison to the standard solar cell is obvious; so the final result is to allow for sub-bandgap excitations thereby allowing for the photoconversion of a larger amount of the illuminating solar spectrum.

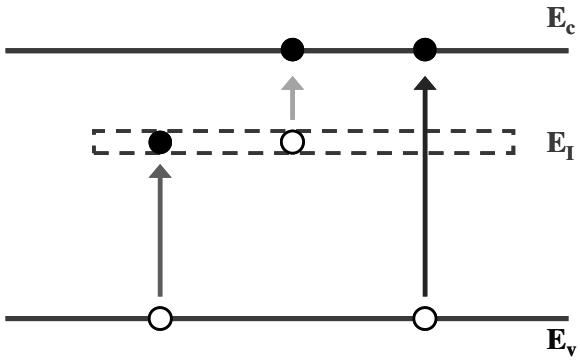

Fig. 12. Energy band diagram showing the operation of the intermediate band solar cell. The standard bulk absorption process is the pumping of an electron from the valence band to the conduction band by a photon with energy greater than E_{CV}. In addition to this, a photon of energy E_{IV} may pump an electron from the valance band to the intermediate band for subsequent excitation to the conduction band by a photon of energy E_{CI}.

In performing a detailed balance analysis of the intermediate band solar cell, three assumptions specific to this design are invoked. The first, there is no overlap of energy transitions for a given photon energy; i.e. if a photon may energetically induce a transition from one band to another, then all photons of the same energy will only cause that specific transition. So, referring to Fig. 12 where E_I is placed arbitrarily closer to E_C than to E_V, there are only three energy ranges of interest: [E_{CI}, E_{IV}], [E_{IV}, E_{CV}], and [E_{CV}, ∞). This assumption is actually similar to the analysis of the multi-junction cell in that each sub-cell was taken to have its own unique energy domain. The second assumption is that no current is able to be extracted from or injected into the intermediate band by means of an electrical contact; i.e. electrons enter the intermediate band only by pumping from the valence band and they leave only by subsequent pumping to the conduction band. Finally, each band must have associated

with it, its own quasi-Fermi level; so the difference in chemical potentials between any two bands is simply the difference between the quasi-Fermi levels of the two bands.

Following from (16), the spectral flux from the sun giving rise to the short-circuit current is

$$\frac{d\Phi_s}{dE} = f_s \frac{2\pi}{h^3 c^2} \frac{E^2}{e^{E/kT_s} - 1} \tag{27}$$

while the spectral flux leaving the solar cell, thus giving rise to the dark current, is

$$\frac{d\Phi_c(\mu)}{dE} = \frac{2\pi}{h^3 c^2} \frac{E^2}{e^{(E-\mu)/kT_c} - 1}. \tag{28}$$

An equivalent circuit of the intermediate band solar cell may be constructed, as in Fig. 13, based on the stated assumptions. As in previous analyses, the chemical potentials correspond to voltage drops across the equivalent circuit elements. In Fig. 13, photodiode 1 corresponds to the standard effect of an electronic transition across the bandgap, photodiode 2A corresponds to the effect of the intermediate-to-conduction band transition, and photodiode 2B corresponds to the valence-to-intermediate band transition. The currents through each of the circuit elements are therefore:

$$\begin{aligned}
J_1 &= q \int_{E_{CV}}^{\infty} \frac{d\Phi_s}{dE} dE - q \int_{E_{CV}}^{\infty} \frac{d\Phi_c(\mu_{CV})}{dE} dE \\
J_{2A} &= q \int_{E_{CI}}^{E_{IV}} \frac{d\Phi_s}{dE} dE - q \int_{E_{CI}}^{E_{IV}} \frac{d\Phi_c(\mu_{CI})}{dE} dE \\
J_{2B} &= q \int_{E_{IV}}^{E_{CV}} \frac{d\Phi_s}{dE} dE - q \int_{E_{IV}}^{E_{CV}} \frac{d\Phi_c(\mu_{IV})}{dE} dE
\end{aligned} \tag{29}$$

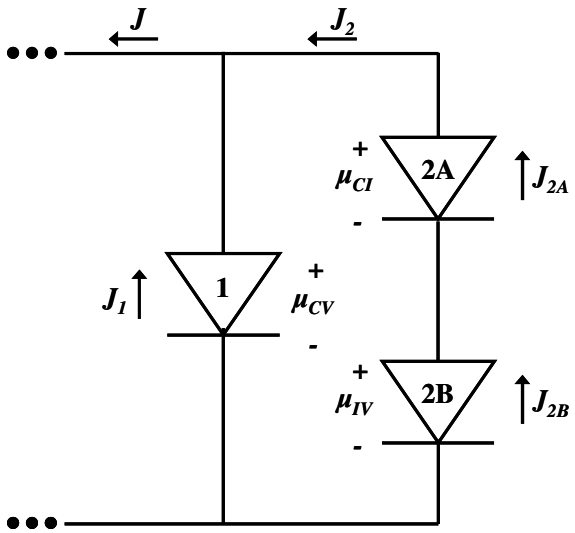

Fig. 13. Equivalent circuit of the intermediate band solar cell. Current J_1 is due to the standard valence-to-conduction band photoabsorption process while current J_2 accounts for the enhancement due to the presence of the intermediate band. These currents add to give the total current J of the intermediate band solar cell. The voltage applied to the device corresponds to the chemical potentials by $V = \mu_{CV} / q$.

From Fig. 13, the currents J_{2A} and J_{2B} must be equal; these may be simply referred to as current J_2. The current J_2 adds with J_1 to give the total current J. As in previous analyses, the applied voltage is dropped such that it corresponds to the chemical potential difference between the conduction and valence bands. This energy splitting then determines the values of the chemical potential differences with respect to the intermediate band. So the current-voltage characteristics of the intermediate band solar cell can be determined by considering the total current

$$J(V) = J_1 + J_2 \tag{30}$$

which is fundamentally a function of the chemical potential such that

$$\mu_{CV} = qV \, . \tag{31}$$

The contribution of current J_1 is straightforward to calculate. The current J_2 must meet the condition

$$J_2 = J_{2A}(\mu_{CI}) = J_{2B}(\mu_{IV}) \tag{32}$$

where the respective chemical potentials are determined at each operation point by

$$\mu_{CI} + \mu_{IV} = \mu_{CV} = qV\ . \tag{33}$$

The methodology outlined here is algorithmically solved by iteration throughout a range of voltages. This allows a maximum power point to be determined thus giving photovoltaic efficiency.

Following the methodology outlined above allows for the generation of efficiency contours as plotted in Fig. 14. These plots show the detailed balance efficiency limit, under 6000 K blackbody illumination, of the intermediate band solar cell as a function of the intermediate band location. In other words, referring to Fig. 12, the values of E_{CI} and E_{IV} determine the limiting efficiency of the photovoltaic device. This is explicitly presented in Fig. 14 for the physically relevant illumination factors of 1, 10, 100, and 1000-sun concentrations. Note that specified values of E_{CI} and E_{IV} set the bulk bandgap E_{CV}.

From Fig. 14.a, the detailed balance efficiency limit under blackbody illumination is 46.8 %. This corresponds to intermediate bandgaps of $E_{IV} = 1.49\ eV$ and $E_{CI} = 0.92\ eV$; the complete bandgap E_{CV} is therefore 2.41 eV. As the solar concentration is increased to 1000 suns, the optimum values of both E_{IV} and E_{CI} decrease monotonically to 1.31 eV and 0.77 eV, respectively. The efficiency at this point is 57.3 %. The corresponding total bandgap is therefore also decreased at 1000 suns to 2.08 eV. This behavior of decreased optimum bandgap with increased solar concentration is comparable to Figs. 4 and 8.b, both of which demonstrate similar behavior for the single junction solar cell. Table II lists the limiting efficiencies and corresponding bandgaps for the plots in Fig. 14.

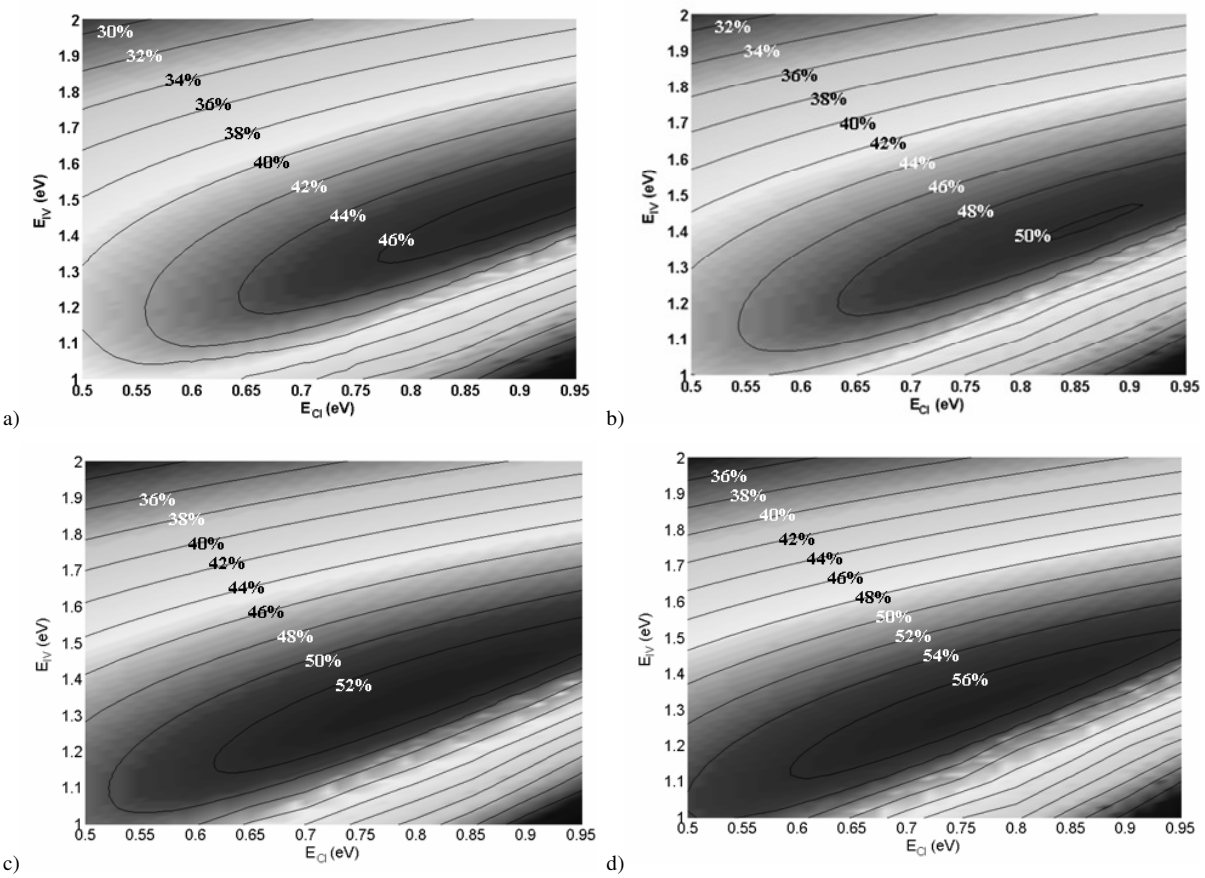

Fig. 14. Contour plots showing the detailed balance efficiency limit of the intermediate band solar cell as it varies with the spacings between the conduction and intermediate bands and between the intermediate and valence bands. The illuminating spectrum is that of a 6000 K blackbody with concentration factors of a) 1 sun, b) 10 suns, c) 100 suns, and d) 1000 suns.

Table II

Detailed Balance Efficiency Limits Under 6000 K Blackbody Illumination

Solar Concentration	1	10	100	1000
Efficiency Limit	46.8 %	50.1 %	53.6 %	57.3 %
E_{IV} (eV)	1.49	1.43	1.36	1.31
E_{CI} (eV)	0.92	0.87	0.81	0.77
E_{CV} (eV)	2.41	2.30	2.17	2.08

Similar to the generation of Fig. 6, the detailed balance analysis of the intermediate band solar cell can be made more realistic by invoking the actual AM0 and AM1.5 solar spectrums which are plotted in Fig. 5. In doing so, the analytic form of (27) is replaced with numerical data from Fig. 5. Efficiency contours for the intermediate band solar cell subject to

AM0 illumination are plotted in Fig. 15 for 1, 10, 100, and 1000-sun concentrations. These plots are similar to those in Fig. 14 due to the similarity between the blackbody and AM0 spectra. Some roughness is seen in the AM0 contours due to the roughness of the AM0 spectrum. The corresponding efficiency limits and optimum bandgaps are listed in Table III.

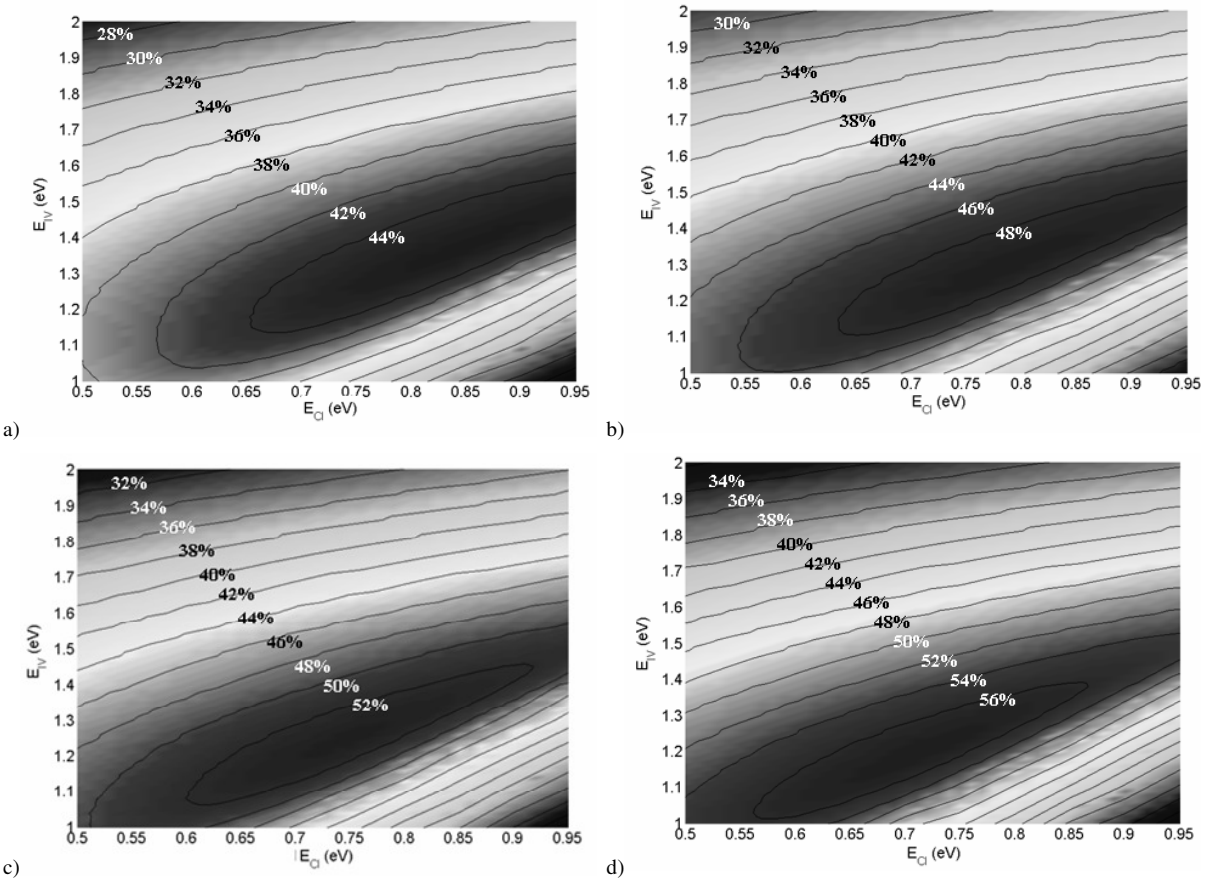

Fig. 15. Contour plots showing the detailed balance efficiency limit of the intermediate band solar cell as it varies with the spacings between the conduction and intermediate bands and between the intermediate and valence bands. The AM0 solar spectrum is used with concentration factors of a) 1 sun, b) 10 suns, c) 100 suns, and d) 1000 suns.

Table III

Detailed Balance Efficiency Limits Under AM0 Illumination

Solar Concentration	1	10	100	1000
Efficiency Limit	45.8 %	49.5 %	53.3 %	57.4 %
E_{IV} (eV)	1.38	1.27	1.27	1.22
E_{CI} (eV)	0.85	0.77	0.77	0.73
E_{CV} (eV)	2.23	2.04	2.04	1.95

The AM1.5 detailed balance efficiency contours are plotted in Fig. 16 for 1, 10, 100, and 1000-sun concentrations. The 1-sun case makes use of the AM1.5G spectrum while the remainder uses the AM1.5D spectrum. The contours in Fig. 16 exhibit a much more irregular structure when compared to the previous examples under blackbody and AM0 illumination. This is due to the large degree of roughness and attenuation lines in the AM1.5 spectra. Of particular interest is the presence of several local maxima in the AM1.5 efficiency contours. This is comparable to Fig. 6.b where the efficiency vs. bandgap plot of the single junction solar cell illuminated by the AM1.5 spectrum exhibited similar behavior. The AM1.5 detailed balance efficiency limits and corresponding optimum bandgaps are listed in Table IV.

Table IV

Detailed Balance Efficiency Limits Under AM1.5 Illumination

Solar Concentration	1	10	100	1000
Efficiency Limit	49.4 %	52.2 %	56.3 %	60.8 %
E_{IV} (eV)	1.50	1.34	1.23	1.22
E_{CI} (eV)	0.93	0.74	0.70	0.69
E_{CV} (eV)	2.43	2.08	1.93	1.91

The vast majority of research work occurring today for the intermediate band solar cell makes use of an InAs quantum dot array placed in the space charge region of a bulk GaAs solar cell [4, 27, 71, 77]. The InAs dot array, being of smaller bulk bandgap than the GaAs host, induces the intermediate band by coupling of confined electronic states in the InAs conduction band; this design scheme is discussed in further detail in Chapter 3. The InAs/GaAs system has the advantage that it is relatively well-studied, it makes use of only binary semiconductors (as opposed to technologically-difficult ternary or higher alloys), and it uses a commercially utilized solar cell material (GaAs).

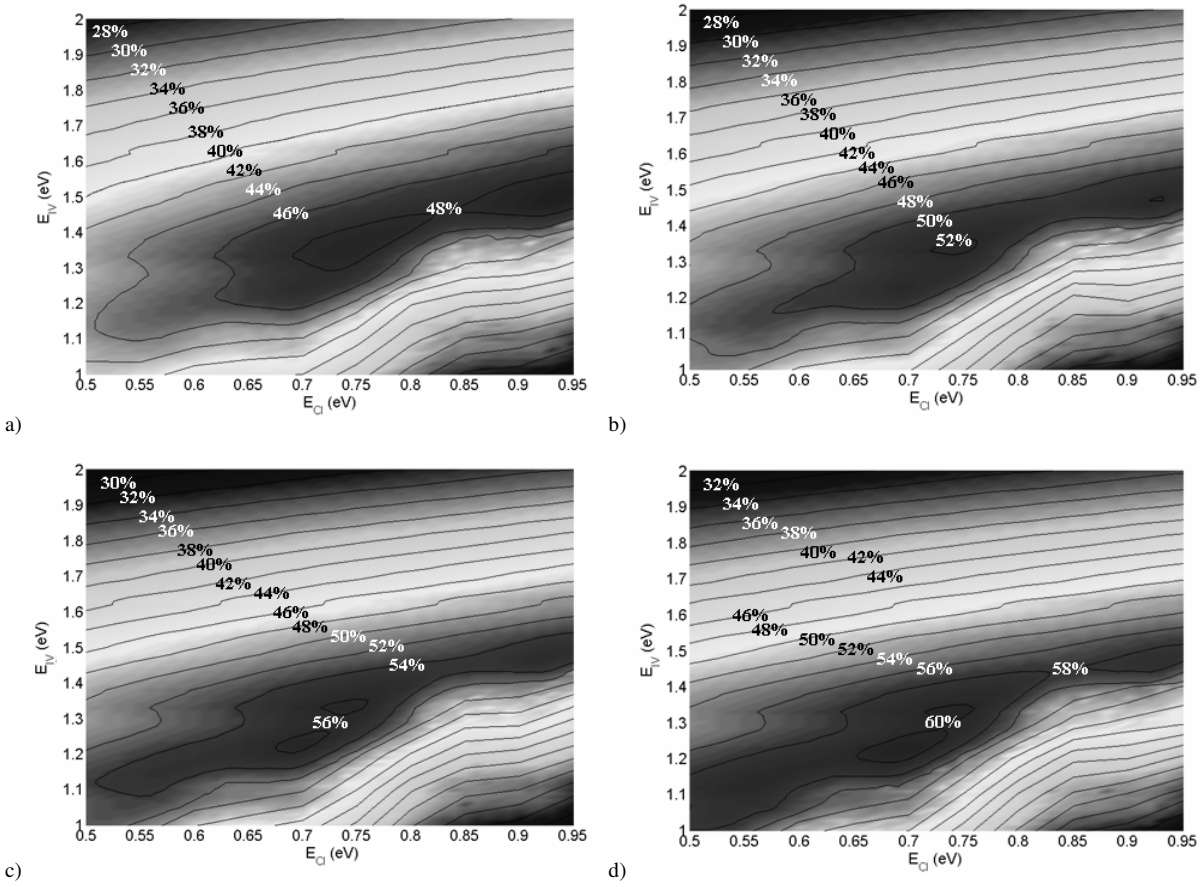

Fig. 16. Contour plots showing the detailed balance efficiency limit of the intermediate band solar cell as it varies with the spacings between the conduction and intermediate bands and between the intermediate and valence bands. In (a), the AM1.5G solar spectrum is used under 1-sun concentration. The remainder makes use of the AM1.5D solar spectrum with concentration factors of b) 10 suns, c) 100 suns, and d) 1000 suns.

This InAs/GaAs (dot/host) system, however, is disadvantaged in that the values of E_{CI} and E_{IV} are approximately 0.4 eV and 1 eV, respectively (see: Section 3.19 and [77]). These intermediate bandgap energies are clearly far from the ideal values determined from Figs. 14-16. Using the models that generated these plots, the detailed balance efficiency limits for the aforementioned system are determined and listed in Table V. A proposed solution is to use a more ideal system based off of technologically difficult antimonide-based ternary systems [78]. This solution, however, only slightly tends towards the optimum intermediate bandgap combinations and does not correspond with the maximum point.

Table V

Detailed Balance Efficiency Limits for the InAs/GaAs System at Several Solar Concentrations

	1x	10x	100x	1000x
Blackbody	36.4 %	41.4 %	46.4 %	51.0 %
AM0	36.6 %	41.6 %	46.7 %	51.3 %
AM1.5	38.6 %	44.1 %	49.6 %	55.0 %

Although the InAs/GaAs system represents a non-ideal combination with respect to the maximum theoretical limits, this system may still be useful when considering the performance enhancement with respect to the single-junction cell. From Figs. 4, 6, and 8, the detailed balance efficiency limits of the single-junction cell are listed in Table VI and are to be compared to the corresponding values from Table V. The single-junction values in Table VI indicate the maximum possible efficiencies, i.e. the efficiencies corresponding to the optimum bandgap, while the intermediate band values in Table V are evaluated at the specific intermediate bandgap combinations of the InAs/GaAs system. From the comparison of the two sets of data, it is evident that the non-ideal intermediate band device still outperforms the optimum single-junction cell at corresponding points. So even though the currently researched intermediate band device does not exhibit ideal parameters, it still represents a significant improvement over the single-junction solar cell.

Table VI

Detailed Balance Efficiency Limits for the Single-Junction Cell at Several Solar Concentrations

	1x	10x	100x	1000x
Blackbody	31.0 %	32.9 %	35.0 %	37.1 %
AM0	30.2 %	32.3 %	34.4 %	36.6 %
AM1.5	33.2 %	35.8 %	38.3 %	40.8 %

Chapter 3

Device Simulations with Silvaco ATLAS

3.1 – Basic Equations

Silvaco ATLAS is a physics-based simulator which has been explicitly designed for the purpose of modeling semiconductor devices [30]. The simulation methodology is physics-based in that the models invoked by the software tend to be derived from first principles or at least empirically derived with careful attention placed to relating such models to the underlying physics. Fundamentally, device operation is governed by and described in a set of two coupled, partial differential equations: the Poisson equation and the equation of continuity.

One may consider two of the axioms to the theory of electrodynamics to be Gauss' law

$$\nabla \cdot \mathbf{E} = \frac{\rho}{\varepsilon} \tag{1}$$

and the Ampère-Maxwell law

$$\nabla \times \mathbf{B} = \mu \mathbf{J} + \frac{1}{v^2} \frac{\partial \mathbf{E}}{\partial t}; \tag{2}$$

these are two of the four Maxwell equations for linear, isotropic media. In the foregoing, E is the electric field, ρ is the charge density, ε is the material permittivity, B is the magnetic field, μ is the material permeability, J is the current density, and v is the speed of light in the medium. Following (1), the relation of the electric field as the negative gradient of the electric potential V yields the Poisson equation:

$$\nabla^2 V = -\frac{\rho}{\varepsilon}. \tag{3}$$

Taking the divergence of (2) yields the equation of continuity:

$$\nabla \cdot \mathbf{J} = -\frac{\partial \rho}{\partial t}. \tag{4}$$

In semiconductor applications, it is customary to modify (4) to include the cumulative effects of the generation G and recombination R of charge carriers [10]. Additionally, separate continuity equations are written for the electron concentration n and the hole concentration p, respectively:

$$\frac{\partial n}{\partial t} = G_n - R_n + \frac{1}{q}\nabla \cdot \mathbf{J}_n \tag{5}$$

$$\frac{\partial p}{\partial t} = G_p - R_p - \frac{1}{q}\nabla \cdot \mathbf{J}_p \tag{6}$$

where q is the elementary charge. Equations (3), (5), and (6) are the governing laws of semiconductor devices. These equations are solved iteratively by ATLAS to obtain a modeled solution of device operation.

3.2 – Carrier Statistics

Additional models that modify the variables in the equations above, or add additional phenomena not yet discussed, may be incorporated; these shall be discussed as necessary. One such model is that of carrier statistics. According to Fermi-Dirac statistics, the electron concentration in the conduction band is given as an integral over energy:

$$n = \int_{E_C}^{\infty} \frac{N(E)dE}{1 + e^{(E-E_F)/kT}} \tag{7}$$

where the density of states is

$$N(E) = M_C \frac{\sqrt{2}}{\pi^2} \frac{m_n^{*3/2} (E - E_C)^{1/2}}{\hbar^3}. \tag{8}$$

In the above, E_F is the Fermi level, E_C is the bottom of the conduction band, k is Boltzmann's constant, T is the temperature, M_C is the number of equivalent minima in the conduction band dispersion, m_n^* is the density of states effective mass for electrons, and $\hbar$ is the reduced Planck's constant. By defining an effective density of states in the conduction band as

$$N_C = 2\left(\frac{2\pi m_n^* kT}{h^2}\right)^{3/2} M_C, \tag{9}$$

where h is the original Planck's constant, (7) may be written as

$$n = N_C \frac{2}{\sqrt{\pi}} \int_{E_C}^{\infty} \frac{[(E - E_C)/kT]^{1/2}}{1 + e^{(E-E_F)/kT}} \frac{dE}{kT}. \tag{10}$$

Although the Fermi-Dirac integral cannot be solved analytically, the form of the integral given in (10) is known as the Fermi-Dirac integral of order one-half and is a well-studied function [31-32]. Solutions to this integral are readily available through look-up tables or by rational Chebyshev approximations [30]. Similarly for holes in the valence band of maximum value E_V with a density of states effective mass m_p^*, the effective density of states in the valence band is defined as

$$N_V = 2\left(\frac{2\pi m_p^* kT}{h^2}\right)^{3/2} \tag{11}$$

and the hole concentration is

$$p = N_V \frac{2}{\sqrt{\pi}} \int_{-\infty}^{E_V} \frac{[(E_V - E)/kT]^{1/2}}{1 + e^{(E_F-E)/kT}} \frac{dE}{kT}. \tag{12}$$

Equilibrium electron and hole concentrations are therefore directly determined by (10) and (12), respectively, and subsequently give the charge density to be used in (3).

For completeness, it should be noted that (10) and (12) are often listed under the Boltzmann approximation:

$$n = N_C e^{-(E_C - E_F)/kT} \qquad p = N_V e^{-(E_F - E_V)/kT} . \tag{13}$$

These expressions tend to be valid as long as the Fermi level lies within the bandgap and is not within ~*3kT* of either band edge. Due to the relatively large dopings used in this work, the Boltzmann approximation is not invoked. By default, the Boltzmann approximation is assumed by ATLAS; the Fermi-Dirac expressions are invoked in the ATLAS syntax by calling *FERMI* in the *MODELS* statement.

3.3 – Finite Element Analysis

The simulation methodology used by ATLAS is a form of finite element analysis. A device structure is defined throughout a rectangular mesh consisting of gridlines that vary in their spatial separation. At each nodal point (i.e. at each intersection of two gridlines), (3), (5), and (6) are iteratively solved until a self-consistent solution is obtained. Any other pertinent models are also included at each nodal point and supplement the fundamental equations.

As an example of a device mesh, a simple p-i-n diode, as created in ATLAS, is shown in Fig. 1. The p-, i-, and n-regions are explicitly shown in Fig. 1.a and the device's underlying mesh is shown in Fig. 1.b. The line spacings within the mesh must be fine enough to adequately resolve the device structure; however, a greater number of nodal points leads to a greater amount of computation time. Typically, the computation time is proportional to N^m,

where N is the number of nodes and m ranges from 2 to 3 depending on the complexity of the problem [30]. The maximum number of nodes allowed by ATLAS is 20,000. In Fig. 1, the mesh spacing is made finer in regions of large electric fields (i.e. near junctions) and is made especially coarse in the quasi-neutral region of the base. This scheme allows for the maximum compromise between computational accuracy and speed.

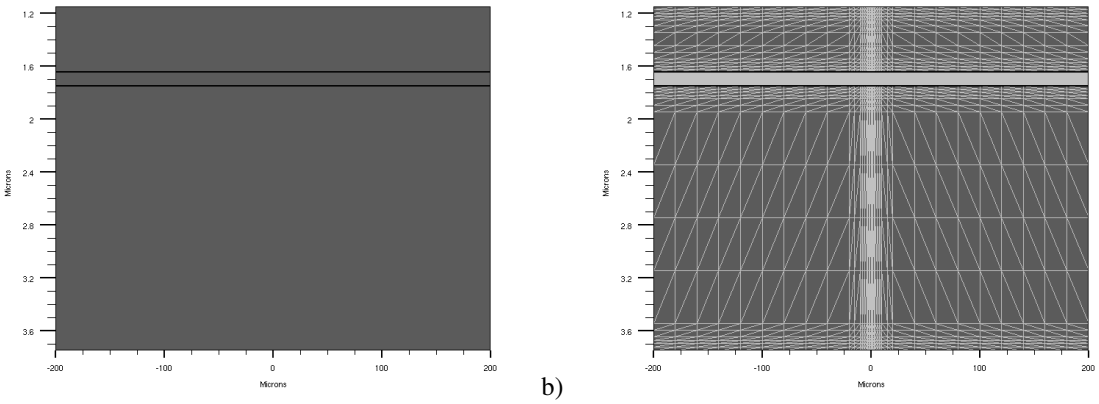

Fig. 1. Device structure of a) a simple homojunction p-i-n diode as created in ATLAS and b) the same structure with an overlaid mesh used for finite element analysis. The top layer represents the emitter, the thin middle layer represents the intrinsic region, and the larger bottom layer represents the base. This shows an example of abrupt junctions as can be realized through epitaxy. The mesh spacings become finest in the high-field area of the space charge region and much coarser in the quasi-neutral region of the base. Fine mesh spacings near the top and bottom of the device are due to foresight in creating an optimized p-i-n structure as discussed in Section 3.17. Fine mesh spacing of vertical gridlines near the middle account for current transport to the top contact.

3.4 – Additional Models

Although the Poisson and continuity equations represent the fundamental laws governing the operation of a semiconductor device, additional models are often necessary to properly account for the dynamic nature of electrons and holes and to elaborate on the rich theory of device physics. These models supplement the Poisson and continuity equations by determining or modifying the variables contained in those laws. An example of this,

previously discussed, is the carrier statistics model based off of the Fermi-Dirac distribution. In this model, carrier concentrations are determined from the Fermi-Dirac theory and are directly used in the charge density portion of Poisson's equation (3). Other models usually dictate specific values of carrier generation and recombination or place modifiers into the current densities of (5) and (6), the continuity equations.

3.5 – Shockley-Read-Hall Recombination

According to the Shockley-Read-Hall hall model [33-35], the recombination of charge carriers can be treated as the separate capture of electrons and holes by trap centers and their subsequent annihilation at the trap center. This recombination mechanism, diagramed in Fig. 2.a, is indirect in k-space and occurs due to the presence of a bulk trap density N_t energetically located at a value E_t within the semiconductor bandgap. Statistically, the net recombination rate may be expressed as

$$R_{SRH} = \frac{\sigma_n \sigma_p v_{th} N_t (np - n_i^2)}{\sigma_n (n + n_i e^{(E_t - E_i)/kT}) + \sigma_p (p + n_i e^{(E_i - E_t)/kT})}, \tag{14}$$

where σ_n and σ_p are the capture cross-sections for electrons and holes, respectively, n_i is the intrinsic carrier concentration, and v_{th} is the thermal velocity. From an experimental and modeling perspective, it may be difficult to determine several of the parameters in (14); however, the difficulty is resolved by defining electron and hole lifetimes, respectively:

$$\tau_n = \frac{1}{\sigma_n v_{th} N_t} \qquad \tau_p = \frac{1}{\sigma_p v_{th} N_t}; \tag{15}$$

so that the net recombination rate may be expressed as

$$R_{SRH} = \frac{np - n_i^2}{\tau_p (n + n_i e^{(E_t - E_i)/kT}) + \tau_n (p + n_i e^{(E_i - E_t)/kT})}. \tag{16}$$

This form of the Shockley-Read-Hall model is utilized by ATLAS by calling *SRH* in the *MODELS* statement; it acts as an input into the carrier continuity equations (5) and (6). The carrier lifetimes may be regarded as empirical parameters and are set in the *MATERIALS* statement by the *TAUN0* and *TAUP0* parameters for electrons and holes, respectively. Unless otherwise noted, these two parameters are both universally set to 50 ns. This lifetime represents a mediocre value that allows for a realistic device simulation. The quantity E_t-E_i is set in the *MATERIALS* statement by the parameter *ETRAP*; in this work, this parameter is set equal to zero because mid-gap traps represent the most effective, and hence most relevant, trapping centers [10, 30].

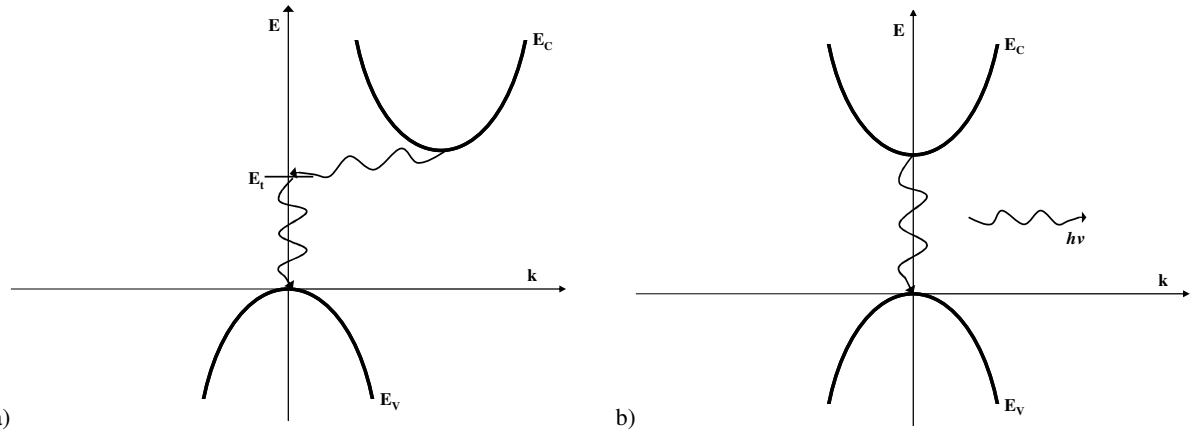

Fig. 2. Electron energy dispersions diagramming a) an indirect electron-hole recombination via a trap state and b) a direct electron-hole recombination culminating in a photon emission.

3.6 – Surface Recombination

In addition to the recombination process due to bulk trapping discussed in the previous section, there also exist the propensity for an additional trapping mechanism due to surface states; this additional process is termed surface recombination. The term “surface” is used to mean any aerial region where the semiconductor lattice terminates. This puts

different general situations on an equal theoretical basis, e.g. insulator-semiconductor interfaces and semiconductor-semiconductor hetero-interfaces.

Simplifications may be made to the carrier continuity equations and give rise to the well-known transport equations [30]; these are sometimes referred to in the literature as the minority carrier diffusion equations [37]. Solutions to these equations for surface recombination due to an aerial surface state density $N_{st}^{'}$ yields the concept of surface recombination velocities for electrons and holes, respectively:

$$S_n = \sigma_n v_{th} N_{st}^{'} \qquad S_p = \sigma_p v_{th} N_{st}^{'}. \tag{17}$$

The standard method for modeling the effects of surface recombination [30, 38] is then given by an expression very similar to (16):

$$R_{surf} = \frac{np - n_i^2}{\tau_p^{eff}(n + n_i e^{(E_t - E_i)/kT}) + \tau_n^{eff}(p + n_i e^{(E_i - E_t)/kT})}. \tag{18}$$

The parameters in (18) are the same as in (16) except for the effective lifetimes which are modeled by ATLAS for electrons and holes, respectively, as

$$\frac{1}{\tau_n^{eff}} = \frac{1}{\tau_n} + \frac{d_m}{A_m} S_n \qquad \frac{1}{\tau_p^{eff}} = \frac{1}{\tau_p} + \frac{d_m}{A_m} S_p, \tag{19}$$

where τ_n and τ_p are the bulk Shockley-Read-Hall lifetimes and d_m and A_m are the length and area, respectively, of the surface corresponding to node m.

This model adds to the recombination terms of the continuity equations and is invoked by including the *INTERFACE* statement in the ATLAS deck. In this statement, S_n and S_p are set by the parameters *S.N* and *S.P*, respectively. At heterojunction interfaces, these parameters are found to be on the order of unity [56, 58, 61]. At the free surfaces of AlAs, GaAs, and InGaP, these parameters are set to 10^8 cm/s. This number is somewhat large

compared to reported values [56, 57, 61]. This increased value, however, seems to give the best simulation results with ATLAS when comparing to experiment; a similar effect has been observed using another device simulator [59].

3.7 – Radiative Recombination

The recombination models discussed in the foregoing section dealt with the indirect process by which electrons and holes recombine due to the presence of traps within the semiconductor bandgap (Fig. 2.a). The other recombination process that tends to be very prevalent in semiconductor work is that of radiative recombination. In this process, an electron in the conduction band directly recombines with a hole in the valence band with no aiding agent nor variance in wavevector as diagramed in Fig. 2.b. This process releases a photon with energy equal to the bandgap and is strongest in direct-gap semiconductors. Although a formal treatment of this process is best done by considering Einstein's theory of spontaneous emission, in practice it is often preferred to use an empirically determined radiative recombination coefficient C [30, 36] such that the radiative recombination rate is then

$$R_{rad} = C(np - n_i^2)\,. \tag{20}$$

This process is invoked in ATLAS in the *MODELS* statement by calling *OPTR* and by defining *COPT* in the *MATERIALS* statement. The *COPT* parameter is defined in this work for GaAs as 7.2×10^{-10} cm^3/s [60]. The only other direct-gap semiconductor considered in this work, InAs, makes use of a separate model discussed in Section 3.13.

3.8 – Thermionic Emission

Local band bending will tend to occur at isotype heterojunctions due to the different material properties of the two semiconductors. This band bending will usually create a potential barrier which may partially impede current flow. It is important to note that current may still flow due to thermionic emission over the barrier or by thermionic field emission through the barrier as diagramed in Fig. 3. It has been found that the standard theory does not properly describe thermionic emission at isotype heterojunctions thus separate expressions must be utilized [39]. There are several alternate theories modeling the phenomena of thermionic emission [39-42]; the expressions used by ATLAS for the electron and hole currents, respectively, due to thermionic emission are [41-42]:

$$J_n = qv_n(1+\delta)\left(n_2 - n_1 e^{-\Delta E_C / kT}\right) \tag{21}$$

$$J_p = -qv_p(1+\delta)\left(p_2 - p_1 e^{-\Delta E_V / kT}\right) \tag{22}$$

where δ is a parameter that includes the effect of thermionic field emission and v_n and v_p are the electron and hole thermal velocities, respectively. ΔE_C and ΔE_V are the maximum energy differences in the conduction band and valence band, respectively, due to the heterojunction. The subscripts on the carrier concentrations denote the two sides of the heterojunction.

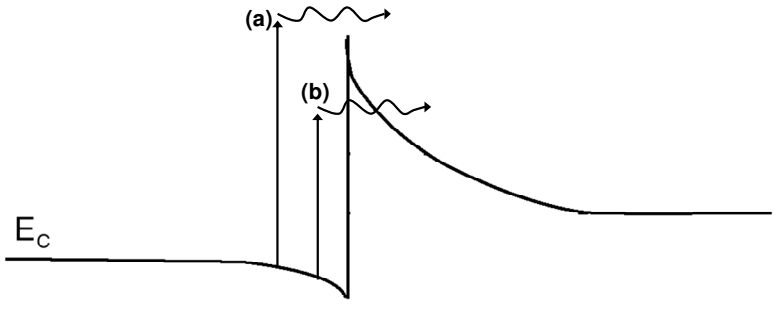

Fig. 3. Conduction band diagram at an abrupt heterojunction showing a) standard thermionic emission and b) thermionic field emission.

Usually the thermal velocities follow from the equipartition theorem [10, 30]; however, in this thermionic emission model, the thermal velocities are determined by

$$v_n = \frac{A_n^* T^2}{qN_C} \qquad\qquad v_p = \frac{A_p^* T^2}{qN_V}, \tag{23}$$

where

$$A_n^* = \frac{4\pi q k^2 m_n^*}{h^3} \qquad\qquad A_p^* = \frac{4\pi q k^2 m_p^*}{h^3} \tag{24}$$

are the electron and hole effective Richardson's constants, respectively. The minimum valued Richardson's constants between region 1 and region 2 are used in the determination of the thermal velocities [42].

Finally, if the barrier width is thin enough, then field emission may supplement the thermionic emission, i.e. thermionic field emission is said to occur. This is included in the thermionic emission model by the δ-parameter:

$$\delta = \frac{1}{kT} \int_{E_m}^{E_C(0^+)} dE \exp\left(\frac{E_C(0^+) - E}{kT} \right) \exp\left(-\frac{2}{\hbar} \int_0^{x_E} dx \sqrt{2m_n^* \left(E_C(0^+) - E(x) \right)} \right), \tag{25}$$

which follows from the Wentzel-Kramers-Brillouin approximation. The parameters in (25) are schematically described in Fig. 4 and $E_m = max\{E_C(0^+), E_C(W)\}$. A similar expression exists for holes by making use of the valence band and hole effective mass instead of the conduction band and electron effective mass.

Use of this thermionic emission model determines the current densities at heterojunction interfaces for subsequent use in the continuity equations. This model is invoked in the ATLAS deck in the *INTERFACE* statement by specifying *THERMIONIC S.S* for standard thermionic emission or *THERMIONIC TUNNEL S.S* for thermionic field emission.

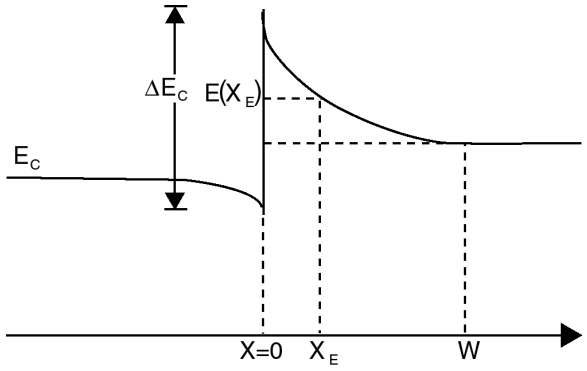

Fig. 4. Conduction band diagram of an isotype heterojunction. The parameters schematically define those used in (25). ΔE_C is the same as that used in (21). (After [30].)

3.9 – Luminous Module

The operation of a solar cell is heavily dependant on the light that impinges onto it as well as the subsequent propagation of electromagnetic radiation throughout the device. How much light is able to transmit through each layer of the device and the propensity for that light to be absorbed and induce carrier photogeneration all play important roles in a solar cell's ultimate performance. Therefore it is paramount to device modeling that the electrodynamics of the incident light as well as its interaction with the semiconductor are properly accounted for.

The Luminous module supplements the ATLAS framework by including ray tracing and photoabsorption algorithms [30]. After inputting any variant of a monochromatic or spectral light source, Luminous determines the intensity of the optical field throughout the device and determines photogeneration rates for use in the carrier continuity equations. Luminous is invoked by specifying a light source in the *BEAM* statement. This light source is monochromatic; its wavelength is determined by setting a value to the *LAMBDA* parameter of the *SOLVE* statement. The light source can be made spectral in the *BEAM* statement by including a data file specified by the *POWER.FILE* parameter. In this chapter the AM0 solar

spectrum (Fig. 5), as discussed in Section 1.3, is utilized to obtain device I-V characteristics. A spectrally varying monochromatic source is used to obtain a short-circuit current spectral response.

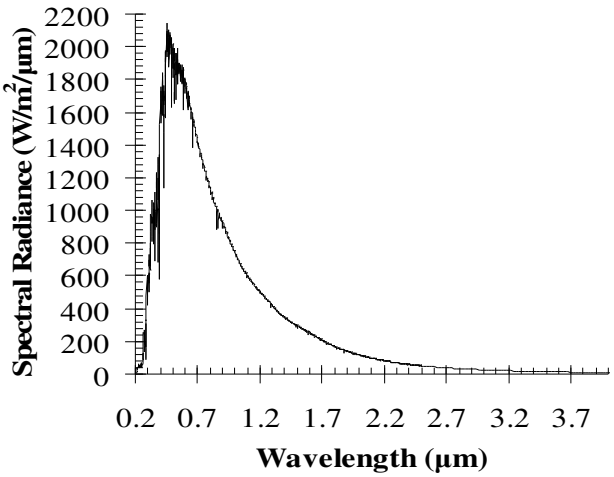

Fig. 5. The ASTM standard air mass zero (AM0) solar spectrum [16]; this is used as the spectral illumination source in the device simulations.

3.10 – Fresnel Coefficients

An electrodynamic treatment of the reflection and transmission of light at an interface gives rise to the Fresnel equations [43]:

$$r_s = -\frac{\sin(\theta_i - \theta_t)}{\sin(\theta_i + \theta_t)} \tag{26}$$

$$r_p = \frac{\tan(\theta_i - \theta_t)}{\tan(\theta_i + \theta_t)} \tag{27}$$

$$t_s = \frac{2\sin\theta_t \cos\theta_i}{\sin(\theta_i + \theta_t)} \tag{28}$$

$$t_p = \frac{2\sin\theta_t \cos\theta_i}{\sin(\theta_i + \theta_t)\cos(\theta_i - \theta_t)} \tag{29}$$

where r and t are the amplitude coefficients of the reflected and transmitted light, respectively; i.e. these values multiplied by the amplitude of the incident optical field gives the amplitudes of the reflected and transmitted optical fields. The subscripts s and p indicate the polarization. θ_i is the angle of incidence and θ_t is the angle of transmission, both with respect to the surface normal (Fig. 6) and related by Snell's law

$$n_i \sin\theta_i = n_t \sin\theta_t . \tag{30}$$

In (30), n_i is the index of refraction in the medium of the incident wave and n_t is the index of refraction in the medium of the transmitted wave; both of which may either be real or complex quantities.

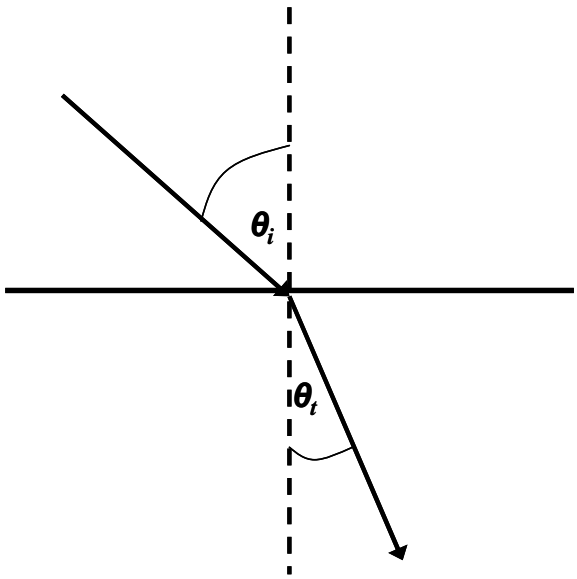

Fig. 6. Diagram of a light ray incident on a surface and refracting at the interface; this defines the angles used in (26)-(30).

The square of each of (26)-(29) gives the corresponding intensity coefficients; i.e. the square of these values multiplied by the intensity of the incident light wave gives the intensities of the reflected and transmitted light waves. For the special case of normal incidence $\theta_i = \theta_t$ and the reflection and transmission intensity coefficients, respectively, are

$$R = r_s^2 = r_p^2 = \left(\frac{n_t - n_i}{n_t + n_i} \right)^2 \tag{31}$$

$$T = t_s^2 = t_p^2 = \frac{4 n_t n_i}{\left(n_t + n_i \right)^2}. \tag{32}$$

The Fresnel model is automatically solved by ATLAS at every material interface whenever light propagation is included [30]. It gives a physics-based modification to the light beam as it traverses through the device structure and impinges upon an interface. The model does not take into account the wave nature of electromagnetic radiation as the material dimensions approach the wavelength of light culminating in the phenomenon of interference.

3.11 – Photogeneration

When photons with sufficient energy impinge onto a semiconductor, those photons may excite valence electrons up to the conduction band thus photogenerating an electron-hole pair. This is the basis on which a solar cell operates upon. The photogeneration rate is modeled in ATLAS as [30]:

$$G_{ph} = \eta_0 \frac{P \lambda}{hc} \alpha e^{-\alpha y} \tag{33}$$

where η_0 is the internal quantum efficiency of an absorbed photon, λ is the optical wavelength, α is the absorption coefficient, y is the relative distance for the ray in question, and P is a coefficient that tracks the cumulative effects of transmission, reflection, and loss throughout the device. The absorption coefficient, sometimes called the attenuation coefficient, is given as [30, 43]:

$$\alpha = \frac{4 \pi k}{\lambda}. \tag{34}$$

In (34) k is the extinction coefficient; it is the imaginary part of the complex index of refraction.

The model for photogeneration is solved by ATLAS at every node located in a semiconductor material; it is automatically invoked whenever a light source is included. The value determined at each node for (33) then becomes an input for the carrier continuity equations.

As light propagates through a material, a loss in the optical intensity will usually be incurred. This is given by a simple exponential law [43]:

$$I(y) = I(0)e^{-\alpha y} \tag{35}$$

where I is the optical intensity. Application of this law is explicitly seen in (33). ATLAS also accounts for (35) by the P factor which modifies the optical ray as it traverses the device through any type of material.

3.12 – Quantum Effects

Additional models are necessary to account for the quantum effects that occur in nanostructures. InAs quantum wells will be considered as an approximation to InAs quantum dots. In this work, the epitaxial growth direction is taken to be along the y-axis; this is the axis along which quantum confinement is considered.

The defining feature of a quantum well is the realization of a two-dimensional electron gas (2DEG); this is in contrast to the three-dimensional electron gas of a bulk material. Due to quantum confinement of the 2DEG, the carrier statistics theory represented by (8)-(13) breaks down and must be superseded by a two-dimensional model.

In two-dimensions the density of states is constant at each energy eigenvalue E_i and is given as [44]:

$$N(E) = 2\frac{m_n^*}{\pi\hbar^2}\sum_i \Theta(E - E_i) \tag{36}$$

where Θ is the Heaviside step function. Substituting into (7) yields the two-dimensional electron concentration

$$n = 2\frac{m_n^* kT}{\pi\hbar^2}\sum_i \ln\left(1 + e^{-(E_i - E_F)/kT}\right). \tag{37}$$

To account for charge localization throughout the width of the quantum well, and assuming uniformity in the growth plane, (37) is modified to include the corresponding eigenfunctions Ψ_i [30]:

$$n(y) = 2\frac{m_n^* kT}{\pi\hbar^2}\sum_i \left|\Psi_i(y)\right|^2 \ln\left(1 + e^{-(E_i - E_F)/kT}\right). \tag{38}$$

Similarly for the two-dimensional hole concentration:

$$p(y) = 2\frac{m_p^* kT}{\pi\hbar^2}\sum_j \left|\Psi_j(y)\right|^2 \ln\left(1 + e^{-(E_F - E_j)/kT}\right). \tag{39}$$

Evaluation of (38) and (39) requires knowledge of the conduction band and valence band eigenstates; this obtained by solving the effective mass Schrödinger equation for electrons

$$-\frac{\hbar^2}{2}\nabla\cdot\frac{1}{m_n^*}\nabla\Psi_i + E_C\Psi_i = E_i\Psi_i \tag{40}$$

and for holes

$$-\frac{\hbar^2}{2}\nabla\cdot\frac{1}{m_p^*}\nabla\Psi_j - E_V\Psi_j = E_j\Psi_j. \tag{41}$$

Justification for these equations is given in Appendix I. Note that there will actually be two sets of solutions for (41); one for heavy holes and one for light holes, with the appropriate use of effective mass. Although not considered in this work, it is mentioned for completeness that multiple sets of solutions will occur for (40) when considering indirect band semiconductors to account for the directionality of the effective mass.

3.13 – Spontaneous Emission

The radiative recombination model described by (20) only accounts for the reduction of electron-hole pairs for use in the continuity equations. In reality, the direct relaxation of an electron to the valence band culminates in the emission of light. Analysis of this feature can be very enlightening; this is even more so for quantum wells since quantization of energy levels will lead to an emission spectrum differing from the bulk scenario.

Following from Fermi's golden rule, an $\boldsymbol{A}\cdot\boldsymbol{p}$ analysis leads to a spectrally-dependent spontaneous emission rate [45]:

$$r(E) = \frac{\pi\hbar q^2}{m_0 \varepsilon E} \left| M(E) \right|^2 \rho D(E) f_i(E) \left(1 - f_j(E)\right) \tag{42}$$

where E refers to the emitted photon energy, m_0 is the free electron mass, and the electron relaxation occurs between the i^{th} conduction band eigenlevel and the j^{th} valence band eigenlevel. The optical density of modes is [46]:

$$D(E) = \frac{n^3 E^2}{\pi^2 \hbar^3 c^3} \tag{43}$$

where n is the index of refraction and c is the speed of light. The reduced mass density of states is given as [30]:

$$\rho = \frac{m_r}{\pi\hbar^2 t} \tag{44}$$

where t is the quantum well thickness and the reduced mass is

$$m_r = \frac{m_n^* m_p^*}{m_n^* + m_p^*}. \tag{45}$$

The Fermi-Dirac distribution in the quantum well for electrons in the conduction band is

$$f_i = \left(1 + \exp\frac{E_i - \frac{m_r}{m_n^*}\left(E - E_{ij}\right) - E_F}{kT}\right)^{-1} \tag{46}$$

and similarly for holes,

$$f_j = \left(1 + \exp\frac{E_j - \frac{m_r}{m_p^*}\left(E - E_{ij}\right) - E_F}{kT}\right)^{-1} \tag{47}$$

where $E_{ij} = E_i - E_j$ is the transition energy from the i^{th} conduction band eigenlevel to the j^{th} valence band eigenlevel.

In (42), the momentum matrix element $M(E)$ is used instead of the electric dipole moment matrix element as a result of the $\boldsymbol{A}\cdot\boldsymbol{p}$ derivation [45]. This quantity is calculated as [30, 47]:

$$M(E) = AM_0\left\langle \Psi_i \middle| \Psi_j \right\rangle \tag{48}$$

where A is an anisotropy factor and M_0 is the bulk momentum matrix element. Models exist to calculate M_0 [30, 45]; however, empirically tabulated values exist for the common direct-gap semiconductors [36]. The anisotropy factors are dependent on the type of holes being considered as well as the polarization of the electromagnetic field; for heavy holes subject to TE polarization:

$$A = \begin{cases} \dfrac{3 + 3E_{ij} / E}{4} & E > E_{ij} \\ 3/2 & E < E_{ij} \end{cases}, \tag{49}$$

for light holes and TE polarization:

$$A = \begin{cases} \dfrac{5 - 3E_{ij} / E}{4} & E > E_{ij} \\ 1/2 & E < E_{ij} \end{cases}, \tag{50}$$

for heavy holes and TM polarization:

$$A = \begin{cases} \dfrac{3 - 3E_{ij} / E}{2} & E > E_{ij} \\ 0 & E < E_{ij} \end{cases}, \tag{51}$$

and for light holes and TM polarization:

$$A = \begin{cases} \dfrac{1 + 3E_{ij} / E}{2} & E > E_{ij} \\ 2 & E < E_{ij} \end{cases}. \tag{52}$$

Note that (42) remains valid for bulk material; however, *M(E)* is substituted by M_0, the energy eigenvalues are replaced by the conduction and valence band edges, E_{ij} becomes the bandgap E_g, and (44) is replaced by

$$\rho(E) = \frac{\sqrt{2}}{\pi^2} \frac{m_r^{3/2} (E - E_g)^{1/2}}{\hbar^3}. \tag{53}$$

3.14 – Band-to-Band Tunneling

In the presence of sufficiently large electric fields or sufficiently thin potential barriers, band to band tunneling may occur. This effect is modeled in ATLAS as an additive generation term to the carrier continuity equations as [30, 69, 70]:

$$G = AE^{\gamma} e^{-B/E} \tag{54}$$

where E is the magnitude of the local electric field and A, B, and γ are adjustable fitting parameters. For direct-gap semiconductors, A, B, and γ are usually given as 9.6615×10^{18} V^{-1}-s^{-1}-cm^{-2}, 30 MV/cm, and 2, respectively [66]. For indirect-gap semiconductors, these parameters are usually given as 4×10^{14} V^{-1}-s^{-1}-cm^{-2}, 19 MV/cm, and 2.5, respectively [69-70].

It should be noted that in ATLAS this model is outside the framework of and separate from the quantum effects module. It is invoked in the *MODELS* statement by specifying *BBT.STD* for direct-gap transitions and *BBT.KL* for indirect-gap transitions.

3.15 – Material Parameters

To accurately simulate a semiconductor device, the correct fundamental material parameters must be provided for use in the models previously discussed. ATLAS contains a vast library of the most recently accepted values of many of these parameters [30]; these have been compared to the literature for correctness [10, 36, 48, 49]. The majority of the fundamental parameters are listed in Table I for AlAs, GaAs, Ge, $In_{0.48}Ga_{0.52}P$, and InAs; these semiconductors will be the focus for the remainder of this chapter.

Table I

Material Parameters for Selected Semiconductors

	ε_r	E_g (eV)	χ (eV)	N_C (cm^{-3})	N_V (cm^{-3})	n_i (cm^{-3})	m_n^*/m_0	m_p^*/m_0	A_n^* (A/cm^2-K^2)	A_p^* (A/cm^2-K^2)
AlAs	10.3	2.16	3.50	1.50×10^{19}	1.81×10^{19}	11.6	0.710	0.804	85.3	96.6
GaAs	13.2	1.42	4.07	4.35×10^{17}	1.29×10^{19}	2.67×10^{6}	0.0670	0.642	6.29	105
Ge	16.0	0.663	4.00	1.05×10^{19}	3.95×10^{18}	1.73×10^{13}	0.559	0.292	67.4	35.0
InGaP	11.8	1.89	4.08	9.26×10^{17}	8.87×10^{18}	391	0.111	0.500	13.3	60.1
InAs	14.6	0.350	4.67	9.33×10^{16}	8.12×10^{18}	1.00×10^{15}	0.0240	0.471	2.88	56.6

The effective masses listed in Table I are the density of states effective masses; these are the necessary values as discussed for the foregoing models. In addition to the above effective masses, it is will also be necessary to obtain the specific valence band effective masses of InAs for use in quantum effects modeling. These values are $0.57m_0$ for heavy holes and $0.025m_0$ for light holes [30, 36, 49].

In addition to the parameters summarized above, the mobilities of electrons and holes must also properly be accounted for to accurately determine carrier transport. These values are dependent on dopant concentration and are therefore very important since dopant concentration tends to vary throughout a device. Mobility values are summarized in Fig. 7 [50-52]. The data for InGaP represents an In:Ga ratio of 1:1.

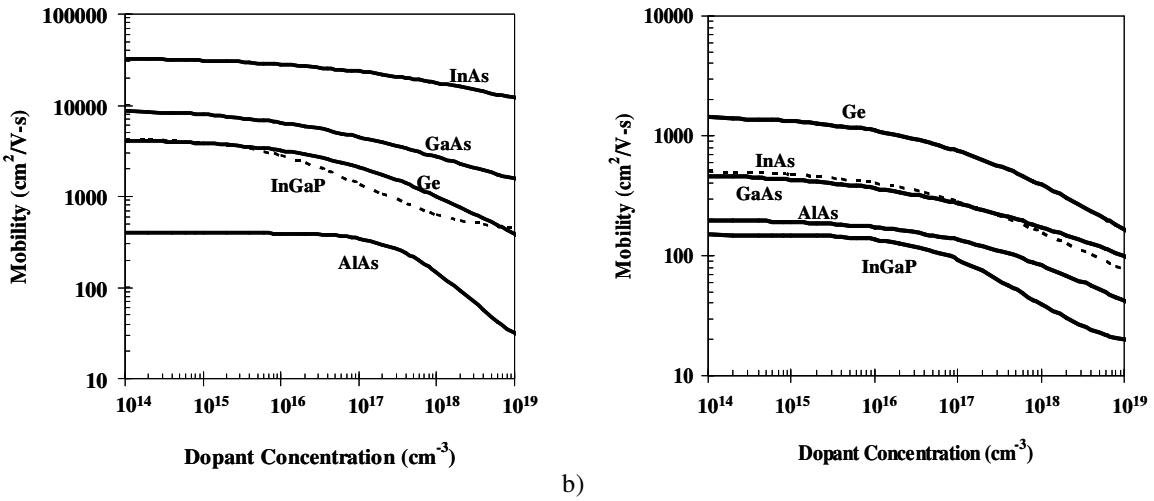

Fig. 7. Concentration-dependent mobilities for a) electrons and b) holes in selected semiconductors.

To make proper use of the optics-based models, the material-specific dispersions of the refractive index and extinction coefficient must be provided; these are summarized in Fig. 8 [30, 53-55]. These parameters are very prevalent within the optical models especially

in dictating light transmission and reflection at an interface and in determining the photo-generation of charge carriers. The data for InGaP represents an In:Ga ratio of 1:1.

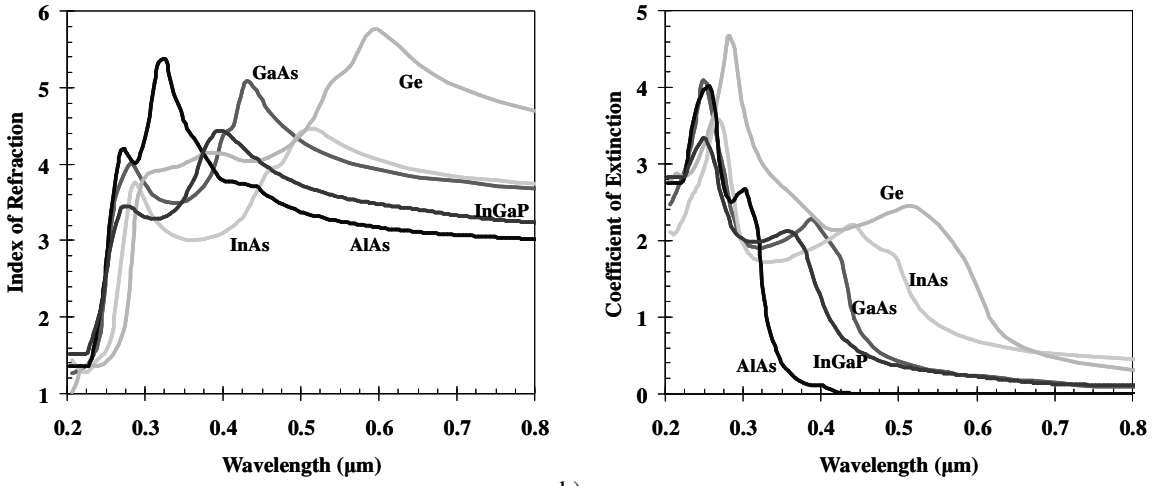

a) b)

Fig. 8. Optical parameter dispersions for selected semiconductors: a) index of refraction and b) coefficient of extinction.

3.16 – General Simulation Methodology

As previously discussed, the ATLAS simulation methodology is a form of finite element analysis. A mesh defines the device structure and the physical models are solved at each nodal point throughout that mesh. The mesh must be spatially fine enough to adequately resolve the device structure and accurately determine the physics thereof; however, an extremely large number of nodes will greatly slow down computation time and there is also a maximum limit programmed into ATLAS.

The issue of mesh resolution poses a problem for solar cell modeling. ATLAS was originally designed for traditional microelectronics such as the transistors used in integrated circuits. In such devices, the dimensions under consideration tend to all be of the same order of magnitude; this is ideal for finite element meshing. In solar cells, however, the top wafer

area may be several square-centimeters, if not larger, while the actual device may only extend several microns deep into the wafer. Add to this the fact that the feature size of the contact grid may also be on the order of micron width but have centimeter lateral extent. Also, even though the actual device depth may only be several microns, these devices are usually fabricated on the top portion of a substrate with a thickness of hundreds of microns. Clearly, the varying dimensions in the common solar cell are not well-suited for finite element meshing. Due to this, careful thought must be put into the simulation methodology.

The device design considered in this work is a rectangular solar cell with regularly spaced contact grid fingers; these grid fingers run parallel to two edges of the solar cell. This device is modeled in ATLAS as a two-dimensional structure consisting of only a portion of the width of an actual device as shown in Fig. 9.a. Note that this model contains the cross-section of one full finger of the contact grid. The substrate is also truncated so that its thickness is on the order of that of the other layers (this is allowed because photogeneration is negligible in this region; a lumped series resistance may be added to the model to account of transport through the substrate if necessary).

The structure as shown in Fig. 9.a is what is actually simulated in ATLAS. Results that are geometry dependent (e.g. current) are normalized to 1 μm of depth into the page. Such results may then be multiplied by appropriate scaling factors so that they are comparable to the results from actual devices. Multiplying by the actual length of the grid finger scales the results as if they were for a three-dimensional structure as in Fig. 9.b. Finally, multiplying by the number of similar regions that make up an actual device scales the results so that they are comparable to experiment; Fig. 9 summarizes this methodology.

Using this method allows for the simulation of a solar cell without running into the problems arising due to the varying dimensions within an actual device.

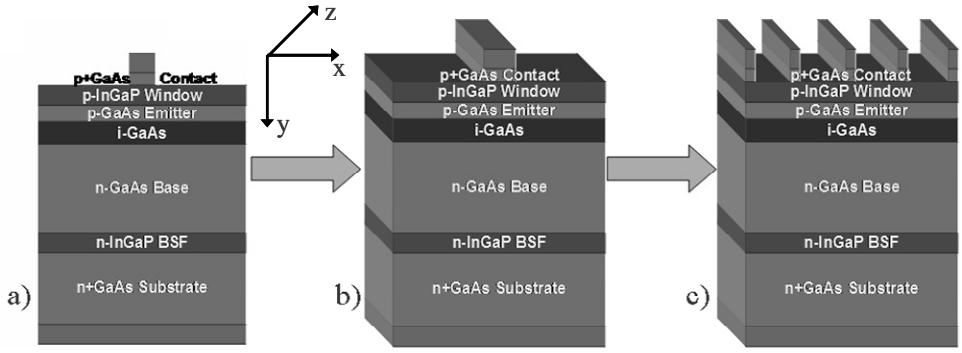

Fig. 9. The solar cell is modeled as a) a two-dimensional structure using only one grid finger. These approximations keep computation time to a minimum. Final results that are dependent on geometry, e.g. current, are modified by a scaling factor to account for b) the three-dimensional nature of an actual device. An additional factor is included to c) account for the desired number of grid fingers to make the model comparable to an actual device. The coordinate axes are those referenced by ATLAS.

3.17 – Unoptimized Single-Junction Solar Cell

Although the solar cell device structure diagramed in Fig. 9 represents the main focus of this work, it is instructional and worthwhile to introduce photovoltaic device simulation with a relatively unoptimized and simple device structure. The device discussed in this section is a simple GaAs p-i-n solar cell as shown in Fig. 10. The i-layer is actually not necessary for this specific device but is included because it will become a necessity in the discussion to follow. The emitter is doped at 10^{18} acceptors/cm^3 and the base at 10^{17} donors/cm^3. The analyzed structure is 400 μm wide with an 8 μm contact centered atop. The nominal layer thicknesses are 500 nm, 100 nm, and 2,000 nm for the emitter, i-layer, and base, respectively. This structure is scaled, post-processing, to simulate a 25 grid finger, 1x1 cm^2 solar cell.

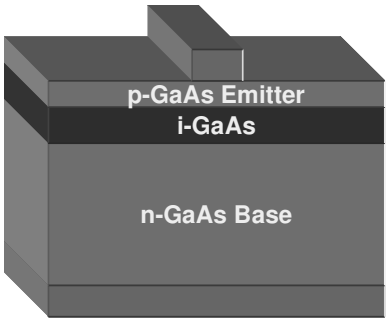

Fig. 10. Simulated GaAs p-i-n solar cell.

The main device characterization methods for a solar cell are to analyze its current-voltage characteristics under illumination and also to determine the cell's spectral response to pertinent wavelengths. These tests are therefore simulated for the defined dive structure; important device metrics are also extracted from the I-V curve. Simulated results for the open-circuit voltage V_{oc}, short-circuit current I_{sc}, maximum power P_m, fill factor FF, and device efficiency η are summarized in Table II. The significant digits of the reported values are taken so as to be comparable to experimental data [4, 71]. This data indicates a relatively low efficiency due primarily to the small amounts of current being driven through the device. The poor performance indicated here is due to the fact that the device structure is unoptimized.

Table II

Device Metrics for the Unoptimized p-i-n Device

V_{oc}	I_{sc}	P_m	FF	η
0.93 V	9.4mA	7.5 mW	86 %	5.5 %

Although the optimization of the device structure in Fig. 10 is not of great importance for this work, it is exemplary to perform further analysis for the sake of illustrating the power of device simulation. Current-voltage characteristics are shown in Figs. 11.a-c for cases of varying the individual layer thicknesses from the nominal values. In all three cases, there is

negligible variance in the open-circuit voltage. Increasing the thicknesses of either the i-layer (Fig. 11.b) or base (Fig. 11.c) leads to very small enhancements in device performance. This indicates that the increased thicknesses allow for the increased photogeneration of charge carriers; however, the increase is minute. It can be inferred from this observation that the vast majority of light incident on to the cell is absorbed since the increased base or i-layer thicknesses do not lead to large increases in device performance.

In sharp contrast to the behavior of varying the thicknesses of the base and i-layer, it is rather a decrease in the emitter thickness that leads to increased device performance. Also in contrast to the previous discussion, the increased device performance due to the decreased emitter thickness is much more prominent as indicated by Fig. 11.a. From this data, it is clear that the smaller emitter thicknesses allow for a larger amount of current to be extracted from the device. The interpretation of these results is that the effect of the thinner emitter is to mask the effect of surface recombination. As the emitter becomes thinner, more photons are able to reach the base, where surface recombination is not an issue, thus leading to the increased currents. More explicitly, after the photogeneration of an electron-hole pair in the n-type base, the electron will preferentially stay in the base and propagate towards the cathode while the hole will be swept by the contact potential to the p-type emitter and towards the anode. For either the electron or the hole, surface recombination becomes a non-issue since they are majority carriers in their current respective locations. The dramatic increase in device performance due to the emitter variation is compared to the small increase observed for base variation in Fig. 11.d.

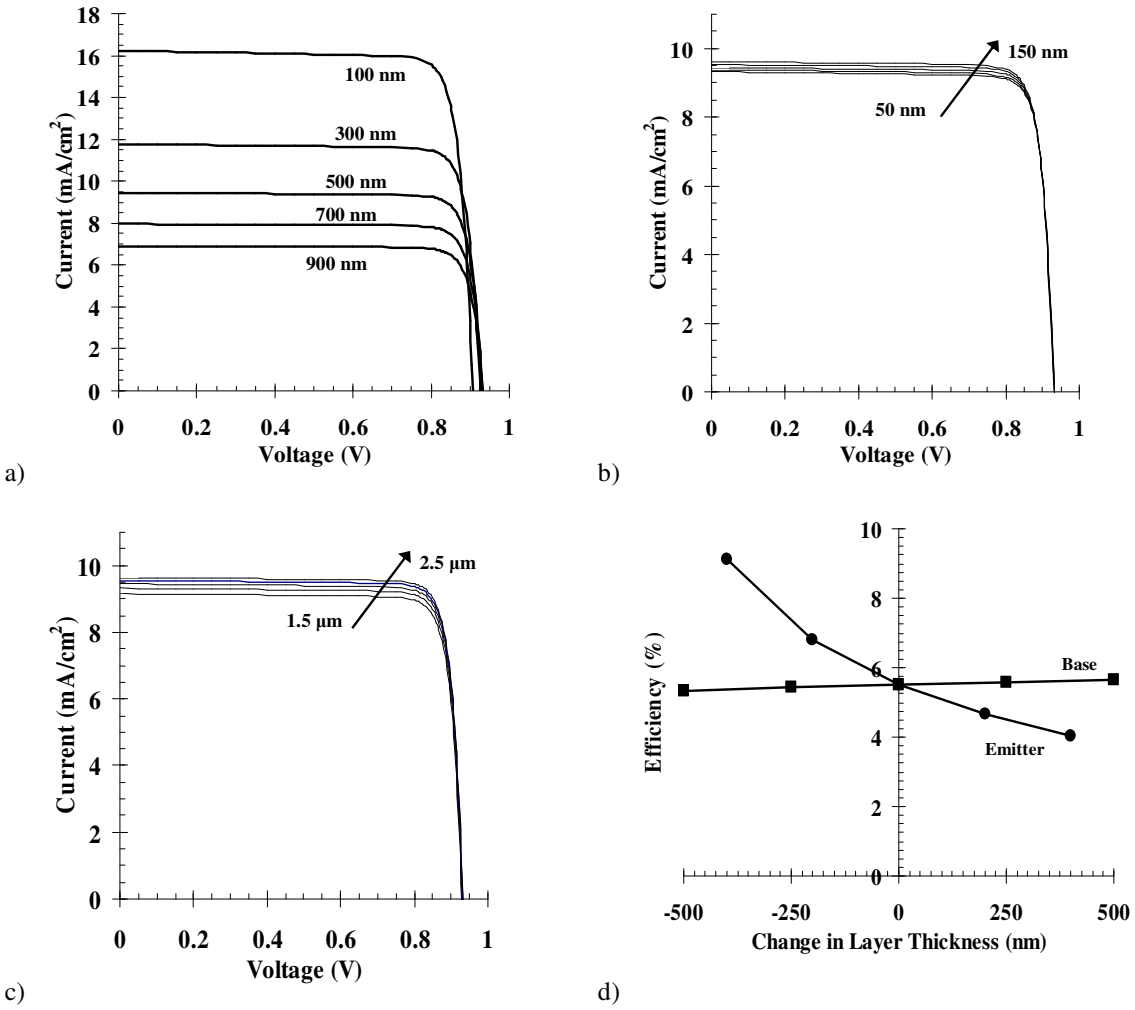

Fig. 11. Current-voltage characteristics for deviations from the nominal thicknesses: a) varying emitter thickness, b) varying i-layer thickness, and c) varying base thickness. d) Simulated efficiencies comparing the effect of varying the base and emitter thicknesses from nominal values.

Also analyzed was the spectral response under the conditions of varied layer thicknesses; this data is plotted as quantum efficiency as a function of wavelength in Fig. 12. The results back up the previously drawn conclusions as well as serve to elucidate on the wavelength-dependent performance of the device. This data shows that the slight increase in device performance due to the increased i-layer or base thicknesses is due to increased absorption at longer wavelengths (Figs. 12.b-c). In distinct contrast to this, the decreased emitter thickness leads to an increased quantum efficiency throughout the super-bandgap part

of the spectrum (Fig. 12.a). In addition, the peak photogeneration shifts from near the bandgap wavelength to shorter wavelengths. These observations indicate that, for decreased emitter thicknesses, a larger amount of photons throughout the entire spectrum are able to reach the base as previously hypothesized; this includes higher energy photons which are often readily absorbed by thicker emitters.

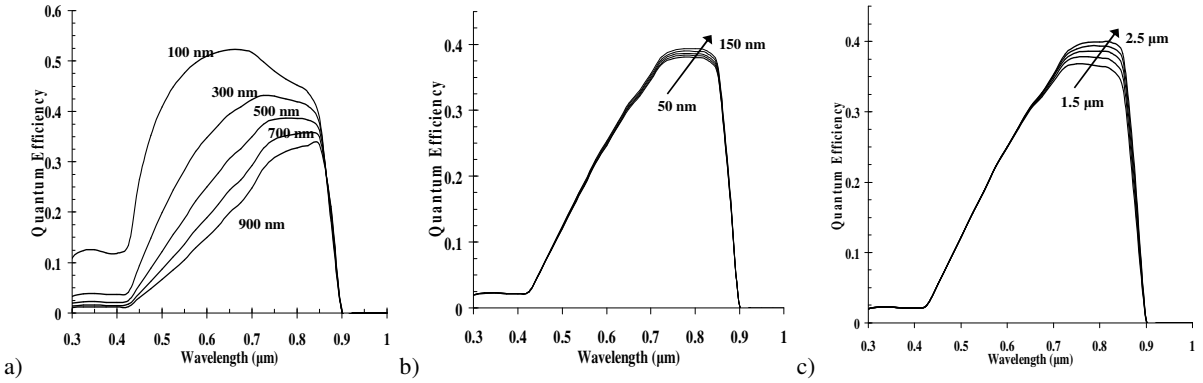

Fig. 12. Spectral responses for varied a) emitter thicknesses, b) i-layer thicknesses, and c) base thicknesses. These results give spectral information lacking in the I-V characteristics and further elaborate on conclusions drawn from those characteristics.

3.18 – Optimized Single-Junction Solar Cell

The device structure shown in Fig. 13 represents a p-i-n solar cell optimized with respect to the device considered in the foregoing section. The device is optimized by the inclusion of two $In_{0.48}Ga_{0.52}P$ layers; one acting as a back surface field (BSF) and the other as the top window (sometimes called a front surface field). These two layers, being of larger bandgap than GaAs and appropriately doped, provide for large electric fields at the two ends of the active portion of the device. These electric fields reflect and accelerate minority carriers towards the junction thus reducing surface recombination effects and increasing solar efficiency. Conversely, one may speak of the potential that arises due to the electric field. From this point of view, the window and BSF layers introduce large potential barriers for

minority carriers thus reflecting them towards the junction. This is clearly seen in the simulated band diagram in Fig. 14. Note that the larger bandgap of InGaP with respect to GaAs allows for the most pertinent portion of the incident light spectrum to reach the GaAs layers unattenuated.

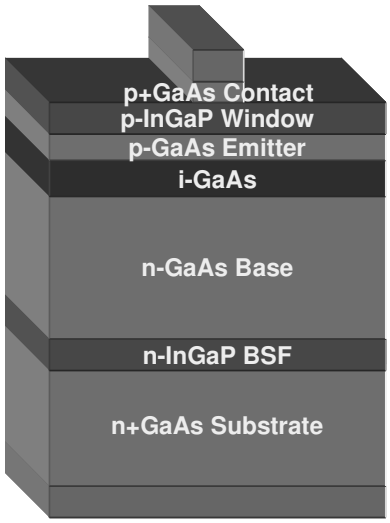

Fig. 13. Simulated GaAs p-i-n solar cell; the device is optimized with respect to that of Fig. 10.

The emitter, i-layer, and base retain the nominal thicknesses and dopings from the foregoing discussion of the unoptimized device. The InGaP layers are both 50 nm thick with a 2×10^{18} cm^{-3} acceptor concentration in the window and 1×10^{18} cm^{-3} donor concentration in the BSF layer. The contact layer is highly doped at an acceptor concentration of 1×10^{19} cm^{-3} and with a thickness of 10 nm. This layer is etched away to exist only under the metal finger; this allows incident light to proceeded to the remainder of the device unattenuated. The purpose of the i-layer is to eventually host a nanostructure array as discussed in Section 3.19.

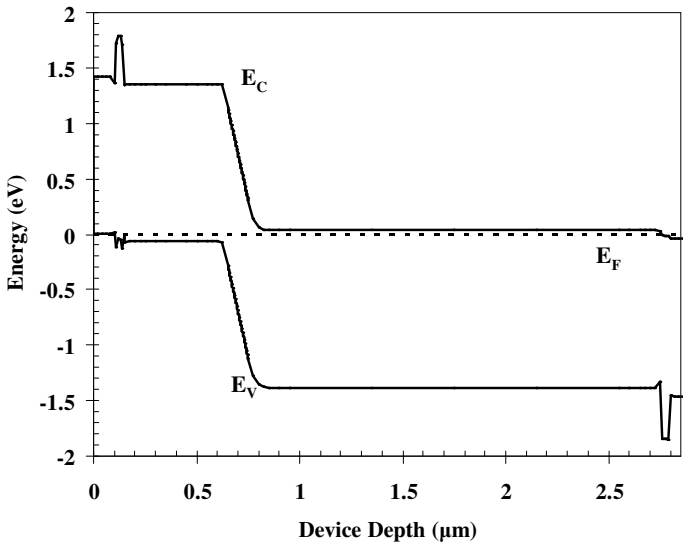

Fig. 14. Simulated band diagram of the optimized p-i-n GaAs cell at thermodynamic equilibrium. The window and BSF layers introduce large potential barriers for minority carriers at either end of the device; this causes photogenerated minority carriers to preferentially traverse towards the junction. The energy axis is taken with reference to the Fermi level.

In simulating the optimized p-i-n solar cell, it was found that the results were very dependent on the optical parameters of the materials considered. This was especially noted in comparing the complex index of refraction of InGaP from a commercial database [55] and from another device simulator [59] as shown in Fig. 15. Although the data from these two sources follow similar trends, they are fundamentally different. Additionally, a slight modification to the commercial data was made at long wavelengths in order to create a more accurate model. The physical effect of this modification, as seen in Fig. 15, is to reduce the long wavelength reflection at the InGaP surface but to increase the reflection at the InGaP-GaAs interface. The modification of such a fundamental material property is justified because InGaP is not a simple chemical compound but rather a more complex alloyed material. The variable ordering of Ga and In atoms will very well have an effect on the bulk

properties of the alloyed material. Long range ordering may even lead to InP-GaP superlattices [62-65].

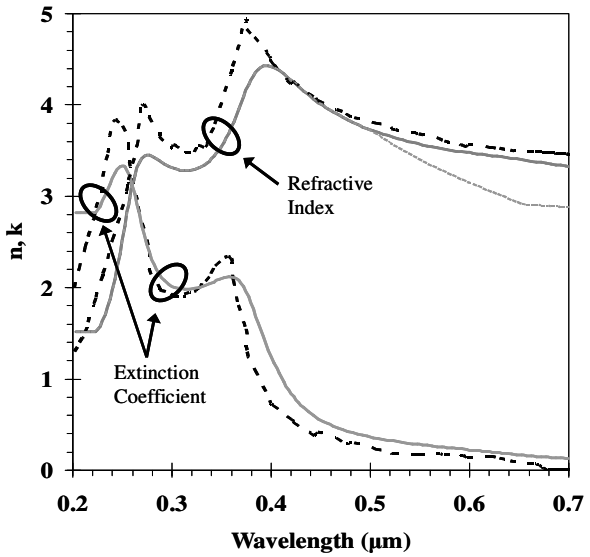

Fig. 15. Index of refraction and coefficient of extinction of $In_{0.5}Ga_{0.5}P$ from two sources: sold curve [55], dark dashed curve [59]. The lighter dashed curve shows a modification made to the data from [55] in order to more accurately model the device.

Simulated results comparing the use of the two sets of InGaP optical parameters are summarized in Table III and Fig. 16 along with experimental data. Following from Fig. 16.a, between all three examples, the open-circuit voltages V_{oc} and the fill factors FF are approximately equal. The only discrepancy that arises is in the short circuit currents I_{sc} (i.e. although some deviation also arises in the maximum powers P_m and in the efficiencies η, these quantities may be derived from the three foregoing metrics). Additional information, directly relating to I_{sc} can be obtained from the spectral response in Fig. 16.b. This clearly indicates that the use of the database values [55] for InGaP leads to device simulations that accurately model the spectrally-dependent nature of the solar cell considered here. It has also been acknowledged that the three short-circuit currents listed in Table III are all within the

experimental error observed in testing solar cells at two different test sites. Additional error may be present in experimentally simulating the AM0 solar spectrum by a Xe arc lamp whereas modeling results make use of standard accepted data for the actual spectrum. Details of the fabrication of the experimental device are found in Ref. [71].

Table III

Device Metrics of the Optimized p-i-n Cell

Ref. for InGaP n, k	V_{oc}	I_{sc}	P_m	FF	η
[55] (Modified)	1.04 V	23.7 mA	20.3 mW	82.4 %	14.9 %
[59] (As Is)	1.04 V	24.5 mA	21.4 mW	83.9 %	15.7 %
N/A (Experiment)	1.04 V	24.7 mA	21.6 mW	83.7 %	15.8 %

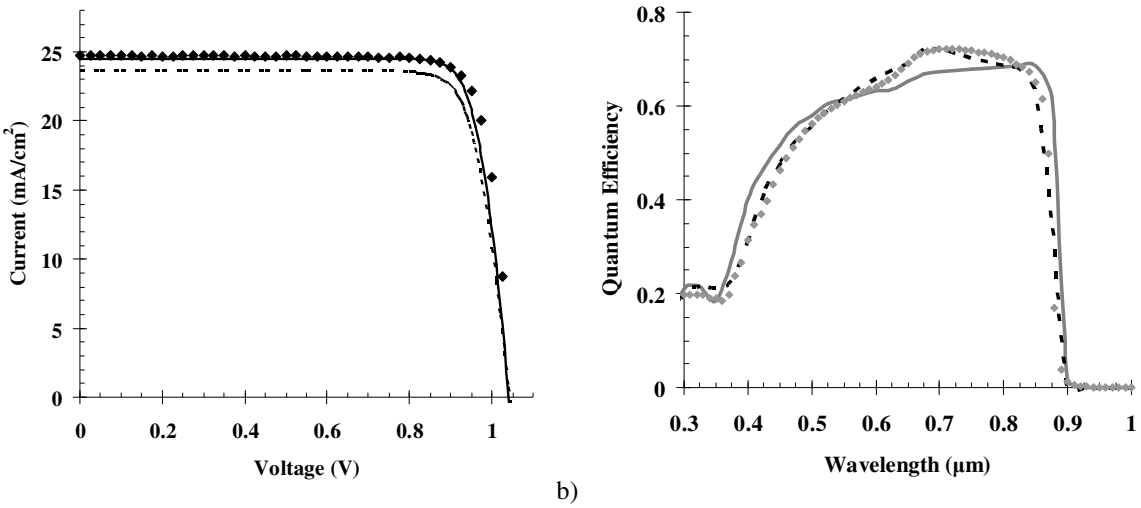

Fig. 16. Electrical results of the optimized p-i-n solar cell. In both plots, the solid curves use the InGaP optical data from [59] while the dashed curves use the modified data from [55]; the individual data points represent experimentally obtained data.

Part of the allure of using a device simulator is to look at physical properties not easily investigated under experimental conditions. As an example of this, Fig. 17.a shows a surface plot of the photogeneration rate throughout the device under AM0 illumination and at zero bias. The plot indicates that the majority of photogeneration does, in fact, occur within

the first micron of depth. To better see the photogeneration throughout the device, Fig. 17.b plots this data as a function of depth on a logarithmic scale. Discontinuities in this plot occur at GaAs-InGaP interfaces. Additionally, the substantial decrease in photogeneration at the BSF layer indicates that the vast majority of photons of 656 nm wavelength and shorter have already been absorbed by that point. In Fig. 17.a, it appears that no photogeneration occurs down the center of the device; this is because the metal finger screens most of the light that impinges onto that area (cf. Fig. 13).

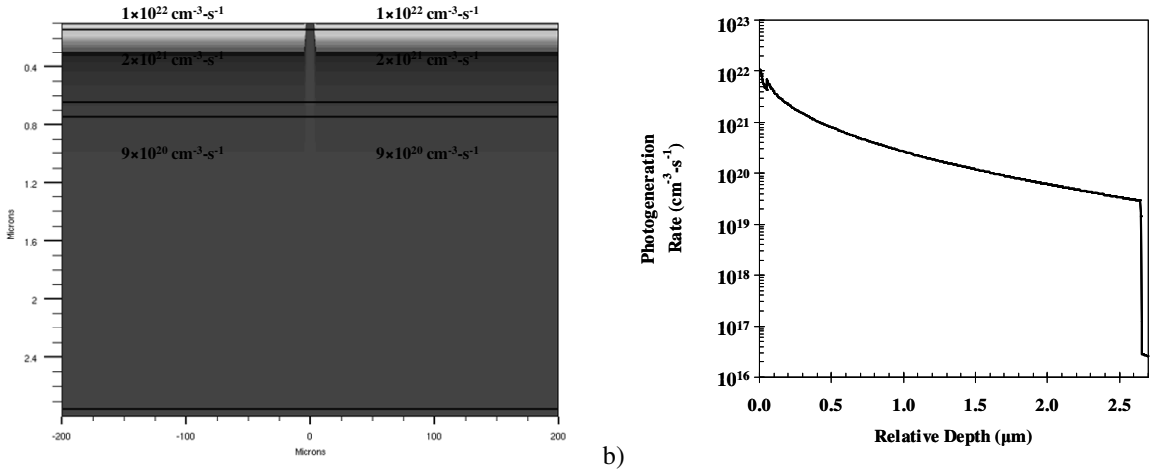

a) b)

Fig. 17. Carrier photogeneration rate plotted a) as a surface plot throughout the device structure and b) logarithmically as a function of device depth. The device layer shown in the surface plot, from top to bottom, are the window, emitter, i-layer, base, and BSF layer. No photogeneration occurs down the center of the device because impingent light is blocked by the metal finger. Discontinuities occur in the semi-log plot at GaAs-InGaP interfaces.

Device simulations also allow for the analysis of device performance under non-ideal or degraded conditions. This allows one to determine possible process tolerances and also enables the testing of hypotheses regarding possible degradation mechanisms. The effect on the I-V characteristics of a non-negligible contact resistance is shown in Fig. 18.a. In these simulations, a non-zero contact resistance was placed on each electrode to show the importance of good metallization. This data indicates that the negative effects of a non-zero

contact resistance, namely an increased solar cell series resistance, become non-negligible when this value is on the order of 10^{-2} Ω–cm^2. Increased contact resistances above that value lead to even more dramatic degradations in device performance. Device metrics extracted form the data in Fig. 18.a are listed in Table IV.

Device degradation due to increased carrier recombination is shown in Fig. 18.b. In these simulations, carrier recombination is increased by decreasing the lifetimes used in the Shockley-Read-Hall recombination model. In contrast to Fig. 18.a where the degradation originally occurs at the knee of the I-V curve, the increased carrier recombinations in Fig. 18.b immediately begin to degrade both I_{sc} and V_{oc}; this is indicative of a shunting mechanism. Pertinent device metrics are listed in Table V. The numerical values in Tables IV-V are taken out to several significant digits for fine comparison and are within the limits of computer precision.

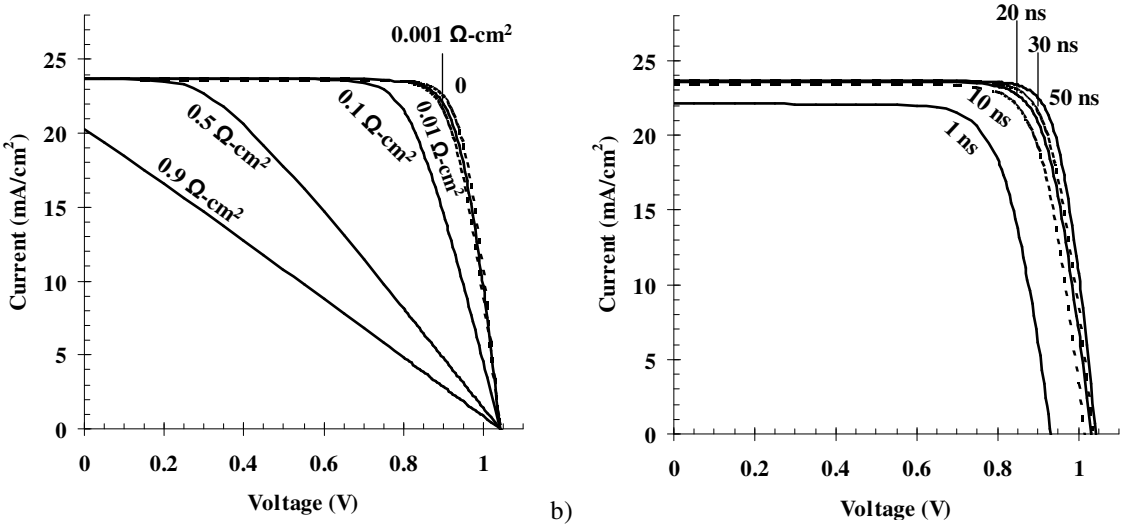

Fig. 18. Current-voltage characteristics showing device degradation due to a) non-negligible contact resistance and b) increased carrier recombination. Increases in contact resistance, placed on both electrodes, leads to an increase in the series resistance of the solar cell thus affecting the overall shape of the I-V characteristics. Increased carrier recombination, modeled as a decrease in Shockley-Read-Hall carrier lifetime, immediately hits both I_{sc} and V_{oc} indicating a shutting mechanism.

Table IV

Device Metrics for Different Contact Resistances

ρ_c	V_{oc}	I_{sc}	P_m	FF	η
0	1.043 V	23.65 mA	20.32 mW	82.38 %	14.87 %
0.001 Ω-cm^2	1.043 V	23.69 mA	19.98 mW	80.86 %	14.63 %
0.01 Ω-cm^2	1.043 V	23.69 mA	19.74 mW	79.89 %	14.45 %
0.1 Ω-cm^2	1.043 V	23.69 mA	17.27 mW	69.89 %	12.64 %
0.5 Ω-cm^2	1.043 V	23.67 mA	8.935 mW	36.19 %	6.541 %
0.9 Ω-cm^2	1.043 V	20.25 mA	5.390 mW	25.52 %	3.956 %

Table V

Device Metrics for Different Carrier Lifetimes

τ_n, τ_p	V_{oc}	I_{sc}	P_m	FF	η
50 ns	1.043 V	23.65 mA	20.32 mW	82.38 %	14.87 %
30 ns	1.037 V	23.64 mA	19.67 mW	80.24 %	14.40 %
20 ns	1.030 V	23.58 mA	19.43 mW	80.00 %	14.22 %
10 ns	1.015 V	23.42 mA	18.63 mW	78.37 %	13.64 %
1 ns	0.9318 V	22.13 mA	15.45 mW	74.92 %	11.31 %

Finally, as was done in Section 3.16, it is important to check that the device structure is, in fact, optimized for device performance. By varying the emitter and base thicknesses, simulations showed very little change in device performance. To best show this, variations in device efficiency due to varied layer thicknesses is plotted in Fig. 19. In regards to emitter thickness, the nominal value is clearly the optimum value; however, it is noted that the degraded performance due to either an increased or decreased thickness occurs over a very small range. With regards to the base, the device efficiency is much less sensitive to thickness variation in this layer. A small increase in the base thickness will actually lead to an increase in efficiency; however, the performance gain is small and negligible. From Fig. 19, the nominal device design can be considered to be optimized. Comparing this to the device design in Section 3.16, it is evident that the InGaP window and BSF play a large role in improving the performance of a solar cell.

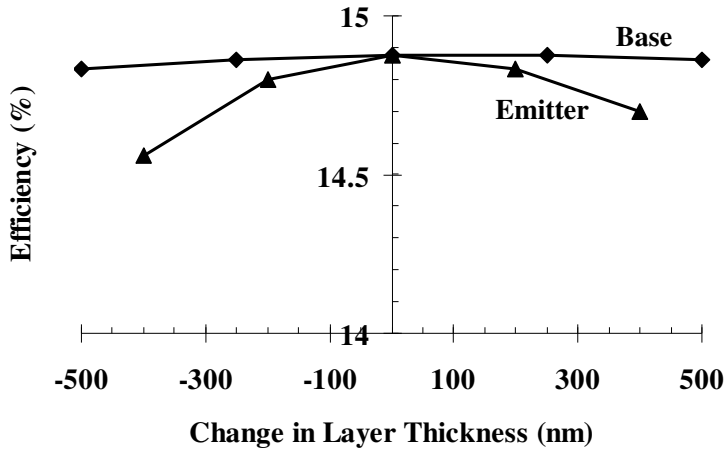

Fig. 19. Simulated efficiencies comparing the effect of varying the base and emitter thicknesses from nominal values. This indicates that the nominal design is already an optimized device.

3.19 – Dual-Junction Solar Cell

Although the purpose of studying the p-i-n solar cell in the previous discussions was for the eventual incorporation of nanostructures in the i-layer, it is beneficial to first evaluate the ability to model a dual-junction solar cell. As discussed in Section 2.3, the dual-junction device, or more generally a multi-junction device, increases solar efficiency by enabling additional and more efficient absorption throughout the solar spectrum. In regards to nanostructured photovoltaics, the incorporation of nanostructures in the multi-junction device may also allow for an effective bandgap tuning as discussed in Section 2.3. Therefore the ability to model such devices would prove useful in the analysis of both present and future solar cell designs.

The device considered in this section is the dual-junction, InGaP-GaAs, tandem solar cell as diagramed in Fig. 20. This design places an InGaP solar cell atop the GaAs solar cell studied in Section 3.17. From top to bottom, the InGaP design is a 100 nm GaAs contact layer doped at 1×10^{19} acceptors/cm^3, 30 nm AlAs window doped at 1×10^{18} acceptors/cm^3,

100 nm InGaP emitter doped at 1×10^{18} acceptors/cm^3, 1 μm InGaP base doped at 1×10^{17} donors/cm^3, and a 100 nm InGaP BSF doped at 1×10^{18} donors/cm^3. In between the InGaP and GaAs solar cells is an n-on-p GaAs tunnel junction; 5×10^{19} cm^{-3} donor concentration and 2×10^{19} cm^{-3} acceptor concentration. This layer allows for electrons in the top cell to recombine with holes in the bottom cell by means of internal field emission thus driving the current; this is easily seen in the device's band diagram (Fig. 21). Similar to the design of the bottom cell, the AlAs window and InGaP BSF of the top cell serve to reflect and accelerate minority carriers towards the top cell junction.

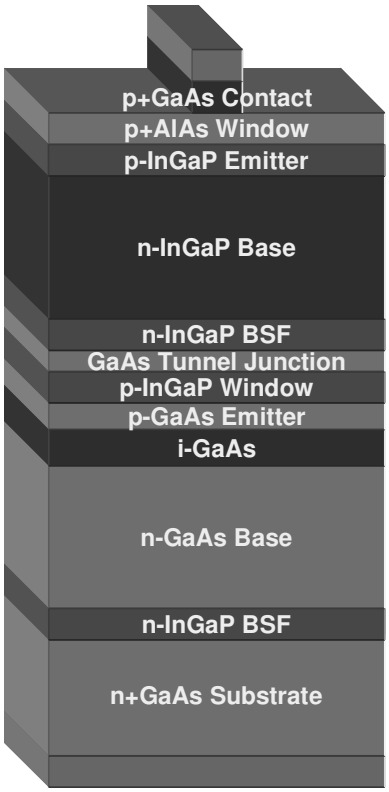

Fig. 20. Device structure of the InGaP-GaAs tandem solar cell considered in this work. The InGaP top cell more efficiently collects short-wavelength light while remaining transparent to the light more efficiently collected by the GaAs bottom cell.

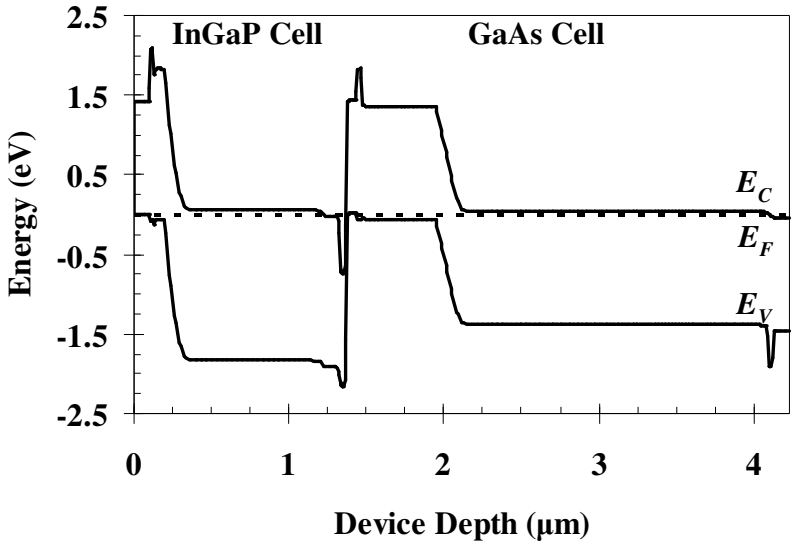

Fig. 21. Band diagram of the InGaP-GaAs solar cell drawn in Fig. 22. This clearly shows how the window and BSF layers act as potential barriers that reflect minority carriers towards their respective junctions. Also observable from this diagram, at ~1.35 μm, is the tunneling region that drives current between the two sub-cells.

A challenge simulating the device as shown in Fig. 20 arises due to the presence of the tunnel junction. As previously reported [67-68], the ATLAS framework is not well suited to handle tunneling problems. Even though such a model exists, as described in Section 3.13, the model is semi-empirical at best and fails to extend upon that quantum effects simulator described in Section 3.11. In practice, this model has been found to be unstable and tends to cause the device solutions to diverge.

Due to the issue of a poorly implemented tunneling model, a convergent simulation was unable to be obtained using the pertinent material parameters described in Section 3.14. However, a simulation did converge by modifying the material parameters of the tunnel junction layer as summarized in Table VI. Optical properties were kept the same; however, the donor and acceptor concentrations were both modified to 1×10^{19} cm^{-3}. These modifications do not imply actual physical conditions but rather are imposed simply to obtain a convergent solution. The purpose of the tunnel junction is simply to drive current between

the two sub-cells. In an equivalent circuit, this can be replaced by a perfect conductor. Therefore the modifications made in order to converge onto a solution are justified.

Table VI

Modified Material Parameters in the Tunnel Junction

	ε_r	E_g (eV)	χ (eV)	N_C (cm^{-3})	N_V (cm^{-3})	n_i (cm^{-3})	m_n^*/m_0	m_p^*/m_0
GaAs	13.2	1.42	4.07	4.35×10^{17}	1.29×10^{19}	2.67×10^{6}	0.0670	0.642
Modified	14.6	0.350	4.67	9.33×10^{16}	8.12×10^{18}	1.00×10^{15}	0.0240	0.471

Another possible method to get around the problems with the tunneling model is to replace the tunnel junction with a perfect conductor. From an equivalent circuit perspective, this would allow current to flow freely between the two sub-cells. This is, however, unfeasible in ATLAS. The ATLAS framework requires that all conductor regions be defined as electrodes; therefore placing a conductor instead of the tunnel junction would not lead to valid results.

The results of simulating the tandem cell with the discussed modifications are shown in Fig. 22 along with experimentally obtained results. Extracted device metrics are listed in Table VII. The data indicates that the modifications made in the tunnel junction yield results that serve as an excellent approximation for actual devices.

Table VII

Device Metrics of the Simulated InGaP-GaAs Solar Cell

V_{oc}	I_{sc}	P_m	FF	η
2.474 V	10.65 mA	22.87 mW	86.80 %	16.74 %

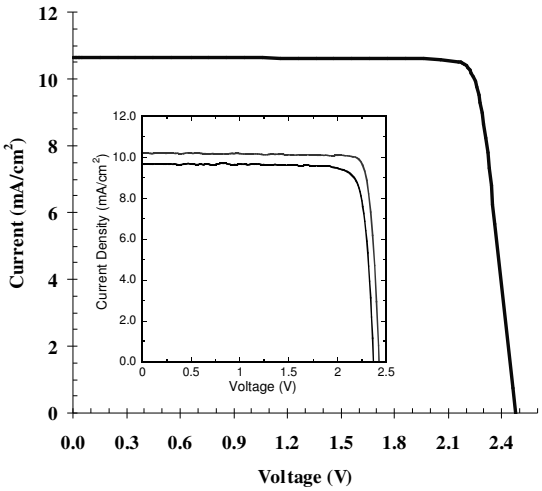

Fig. 22. Simulated I-V characteristic of the InGaP-GaAs tandem cell. The inset shows two separate experimental results of the same type of device thus verifying the simulation method.

Due to the instability of the tunneling model, it proved to be difficult to run optimization tests on the device structure as in the previous discussions. However, a different method, in which the tunneling model may be disregarded, does prove useful. Based upon the analyses in Sections 3.16 and 3.17, it is clear that variations in the thicknesses of the device layers, as long as they are not overly dramatic, have a much larger effect on I_{sc} than on V_{oc}. Therefore, to a very good approximation, it is sufficient to gauge relative variations in device efficiency by relative variations in I_{sc}. One such way to do this, while not having to worry about the troublesome tunneling model, is to look at the spectral response of each sub-cell in the tandem device. The general scheme for doing this is diagramed in Fig. 23. The GaAs tunnel junction is replaced by a void in the form of a "pseudomaterial" of the same thickness but with the refractive index and extinction coefficient of GaAs. The optical parameters are kept to properly account for attenuation of the light ray as it traverses through the space and for reflections at the interfaces. The device in Fig. 23 is then spectrally illuminated with different currents individually extracted from each sub-cell; this leads to the

spectral response in Fig. 24 for the nominal design. Note that interference effects are not observed since they are not accounted for in the physical models.

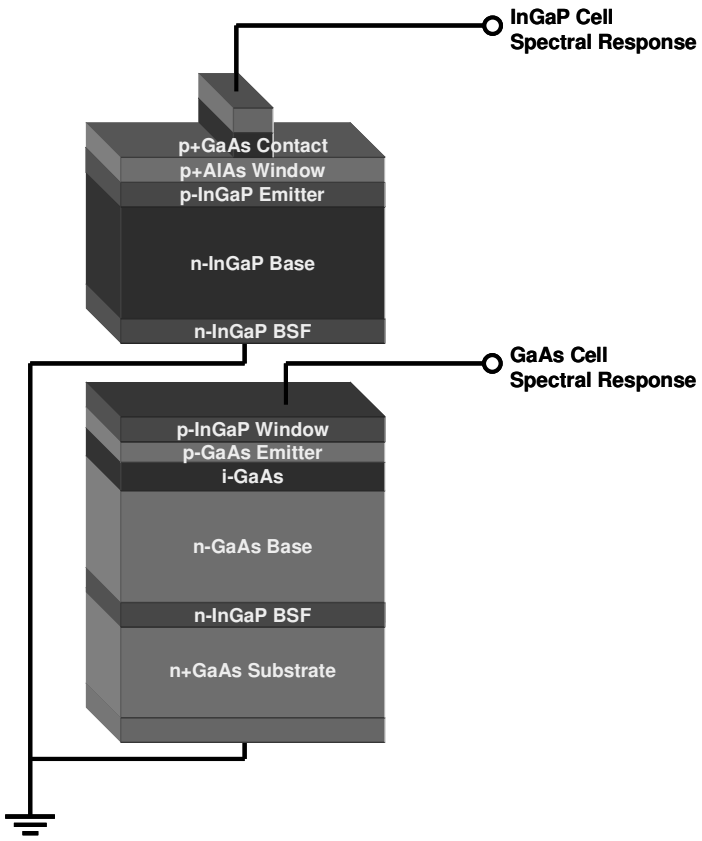

Fig. 23. Simulation scheme for analyzing the spectral response due to either sub-cell. A void replaces the GaAs tunnel junction; however, light traverses through the void as if GaAs were present. Currents are then individually extracted from each sub-cell while illuminated.

In comparing Fig. 24 to Fig.16.b, it is clear that the tandem cell is better suited to perform photoconversion throughout a wider range of wavelengths. This is by virtue of each sub-cell being situated such that they are able to more effectively convert a certain section of the solar spectrum. The photogeneration throughout the device is displayed in Fig. 25.a for a 550 nm light source. This indicates that, at this wavelength, the vast majority of photogeneration occurs due to the InGaP cell; this corresponds with Fig. 24. Similarly, at

800 nm, as shown in Fig. 25.b, InGaP is transparent to the incident light thus allowing the GaAs cell to be the primary current source.

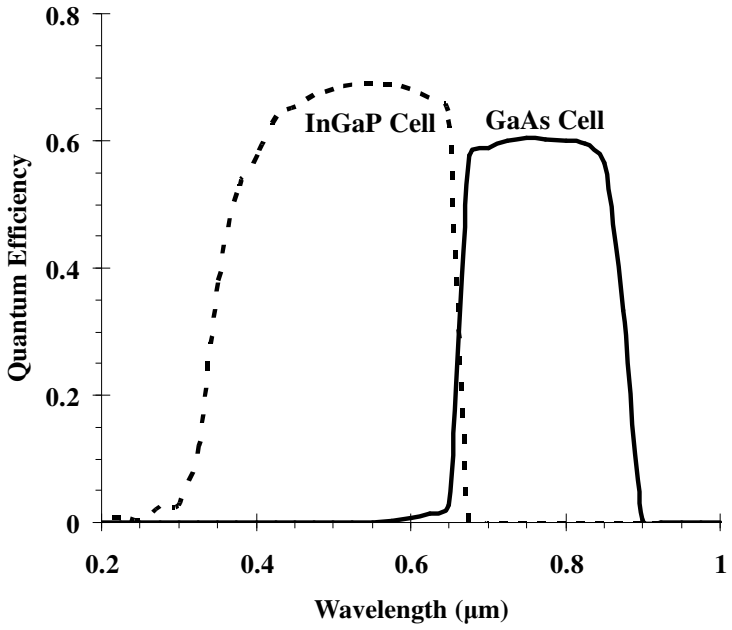

Fig. 24. Spectral response of the InGaP-GaAs tandem cell showing the contributions of each sub-cell.

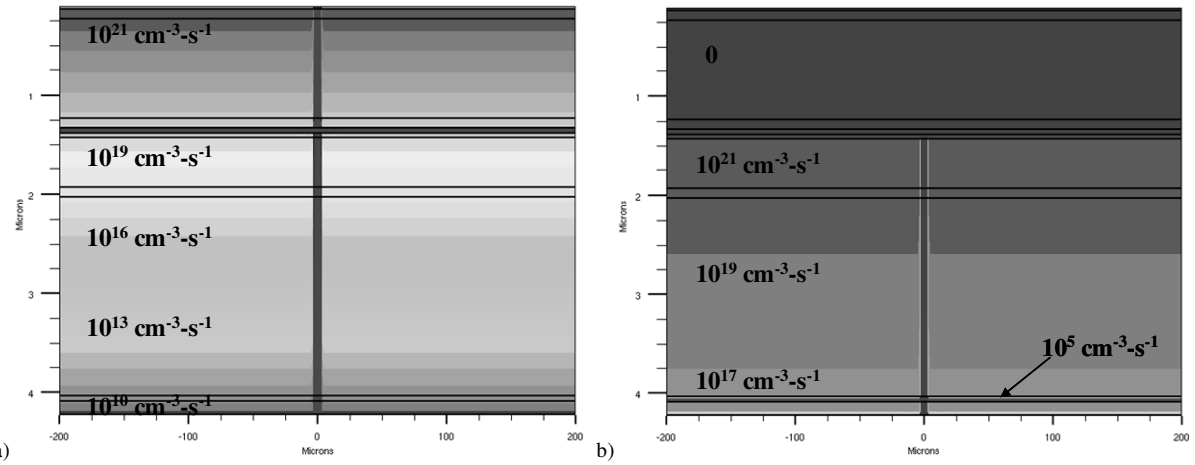

Fig. 25. Photogeneration rate throughout the device for a) a 550 nm and b) 800 nm light source. For the 550 nm illumination, the photogeneration occurs primarily in the InGaP sub-cell; no photogeneration occurs in that cell at 800 nm.

As stated, the spectral response in Fig. 24, being free from the troubles presented by the tunneling model, becomes the primary analysis tool in this section. In fact, the short-circuit current density J_{sc} can be determined from the spectral response as the overlap integral between the wavelength-dependent quantum efficiency $QE(\lambda)$ and the spectral photon flux from the sun $d\Phi/d\lambda$ [10-11]:

$$J_{sc} = q\int QE(\lambda)\frac{d\Phi}{d\lambda}d\lambda \tag{55}$$

where $d\Phi/d\lambda$ can be determined from the ASTM solar spectrum (Fig. 5). For the 1 cm × 1 cm cell characterized by Fig. 24, this gives a short-circuit current of 14.67 mA due to the InGaP cell and 9.615 mA due to the GaAs cell. Therefore, due to the physical constraint of current-matching, the GaAs sub-cell is the current limiting cell under this design.

The effects on the spectral response due to variations in the InGaP base and emitter thicknesses are plotted in Fig. 26. This data indicates that an increase in either layer thickness will lead to a slight improvement in the InGaP spectral response. This improvement, however, is not helpful for the tandem cell because the overall current will be limited by the current generated by the GaAs cell. It is important to note though, as best seen in Fig. 26.b, that a decrease in either the InGaP emitter or base thicknesses, although decreasing the near-bandgap response of the InGaP cell, will lead to a slight increase in the spectral response of the GaAs cell in the same spectral region. This alludes to the possibility of degrading the InGaP current response in favor for boosting that for the current-limited GaAs cell.

Although the isolated GaAs device was determined to already be optimized in Section 3.17, it is worth it to take a look at the GaAs cell as a component of the tandem cell since the absorption primarily occurs in a somewhat narrower portion of the spectrum when compared to Section 3.17. The effect on the spectral response due to variations in the GaAs

sub-cell base and emitter are plotted in Fig. 27. From Fig. 27.a, it can be seen that an increase in the emitter thickness to 750 nm would give an increase in device performance, albeit very small. The base already seems to be at an optimum thickness (Fig. 27.b).

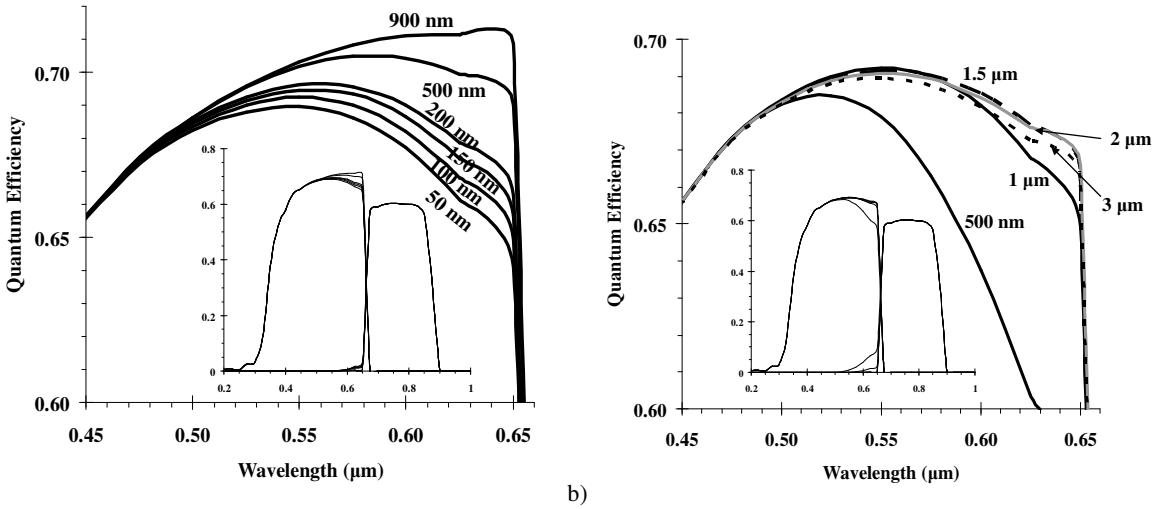

Fig. 26. Effects on the spectral response due to varying the a) emitter thickness and b) base thickness of the InGaP sub-cell. The insets show the full spectral response.

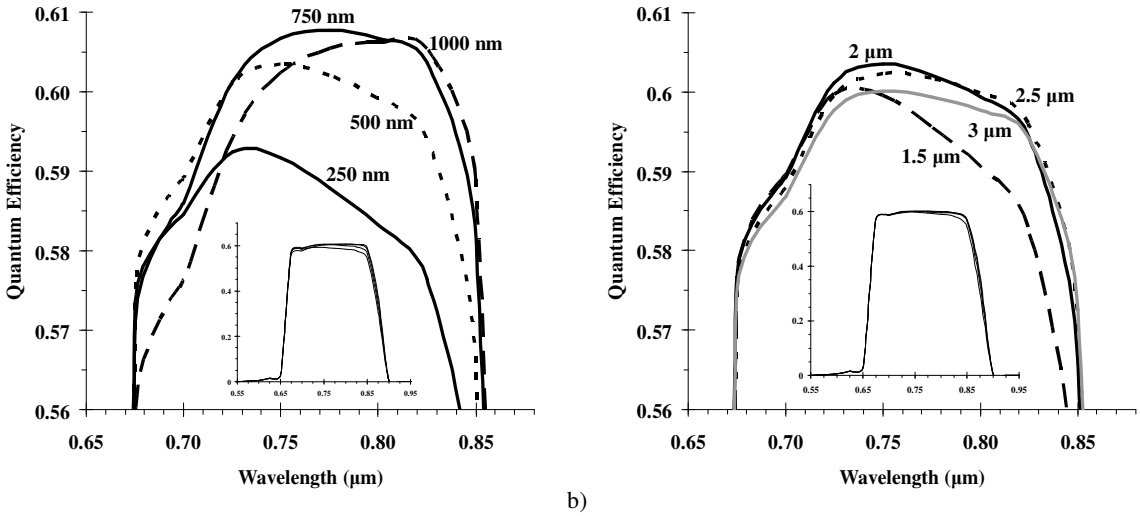

Fig. 27. Effects on the spectral response due to varying the a) emitter thickness and b) base thickness of the GaAs sub-cell. The insets show the full spectral response of the GaAs sub-cell; the InGaP sub-cell is not included because it is not dependent on the properties of the layers below it.

Based on the foregoing analysis from this section, it is apparent that a boost in the spectral response of the GaAs cell may be advantageous to the overall device performance albeit at the expense of a portion of the InGaP spectral response. Modifying the thickness of the InGaP emitter to 50 nm and the GaAs emitter to 750 nm, the InGaP base thickness was varied to find an optimum design. As seen in Fig. 28, the thinner InGaP layers allow for more light to reach the GaAs cell; this culminates in less photogeneration in the InGaP cell but more in the GaAs cell. Table VIII lists the short circuit currents extracted from Fig. 28 by use of (55). The first entry in Table VIII refers to the nominal device. From this data, it would seem that the optimal InGaP base thickness is between 100-250 nm. Such a design would allow for the largest possible current drive with the constraint of a current-limiting sub-cell.

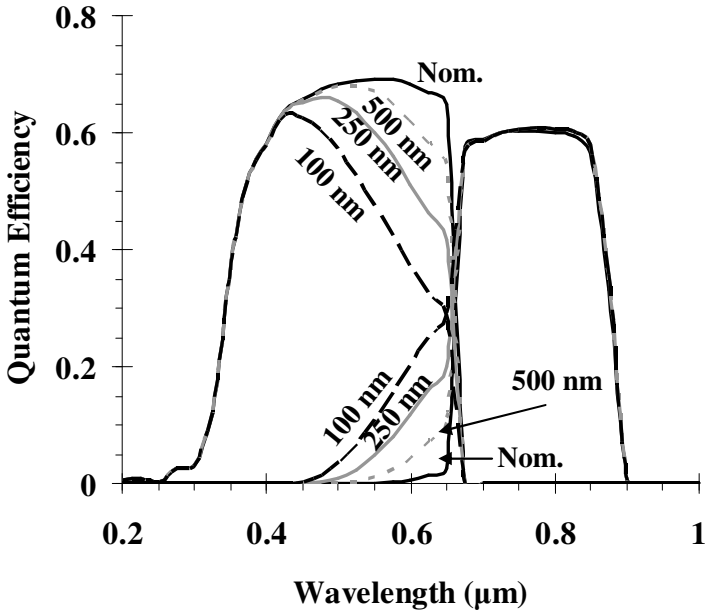

Fig. 28. Effects on the spectral response due to varying the InGaP base thickness compared to the nominal device design. The modified designs use a 50 nm InGaP emitter and 750 nm GaAs emitter.

Table VIII

Short-Circuit Currents Extracted from Fig. 28

InGaP Emitter Thickness	InGaP Base Thickness	Sub-Cell I_{sc}	
		InGaP Cell	GaAs Cell
100 nm	1 μm	14.57 mA	9.615 mA
50 nm	500 nm	13.91 mA	10.17 mA
50 nm	250 nm	12.63 mA	10.94 mA
50 nm	100 nm	10.71 mA	11.98 mA

3.20 – Nanostructured Device

Returning to the p-i-n cell of Section 3.17, the proposed scheme for increasing device efficiency is by the incorporation of a nanostructured array in the i-layer. Such nanostructures may come in the form of planar quantum wells or three-dimensional quantum dots. A nanostructured array of a material with smaller bandgap than the host material (in this case GaAs) would allow for additional absorption of and photogeneration by light of sub-host-bandgap energy. This has two possible outcomes: 1) this would lead to an effective bandgap tuning as is necessary to increase the efficiency of the multi-junction solar cell (Section 2.3) and 2) the nanostructured array may lead to the realization of the intermediate band solar cell as discussed in Section 2.4. For these reasons, it is beneficial to evaluate the abilities and limitations of simulating such a device in ATLAS.

The current research effort at the Nanopower Research Laboratories is in the fabrication of InAs quantum dot GaAs solar cells [4, 27, 71]. In this device, an InAs quantum dot array is placed in the i-layer of a GaAs p-i-n cell. Unfortunately the ability to simulate quantum dots is not present in ATLAS; however, quantum wells may be simulated. Therefore InAs quantum wells were placed in the i-layer of the device presented in Section 3.17 as an approximation for the quantum dots in the experimental device. As an approximation, this is justifiable since the main dimension of interest is the growth axis

which is also the direction of current flow. Since the quantum well model solves for quantization in this direction, use of the model gives an excellent approximation to the experimental situation.

An array of 6 nm InAs quantum wells with 7 nm barrier spacing was placed symmetrically in the center of the i-layer of the p-i-n device. The band diagram of this region in plotted in Fig. 29.a with a close-up of two of the wells plotted in Fig. 29.b. Also displayed in Fig. 29 are the energy eigenvalues that arise due to quantization in the wells; accordingly, one electron eigenstate is realized in the conduction band while in the valence band there are five heavy hole eigenstates and one light hole eigenstate. The corresponding eigenfunctions are plotted in Fig. 30.

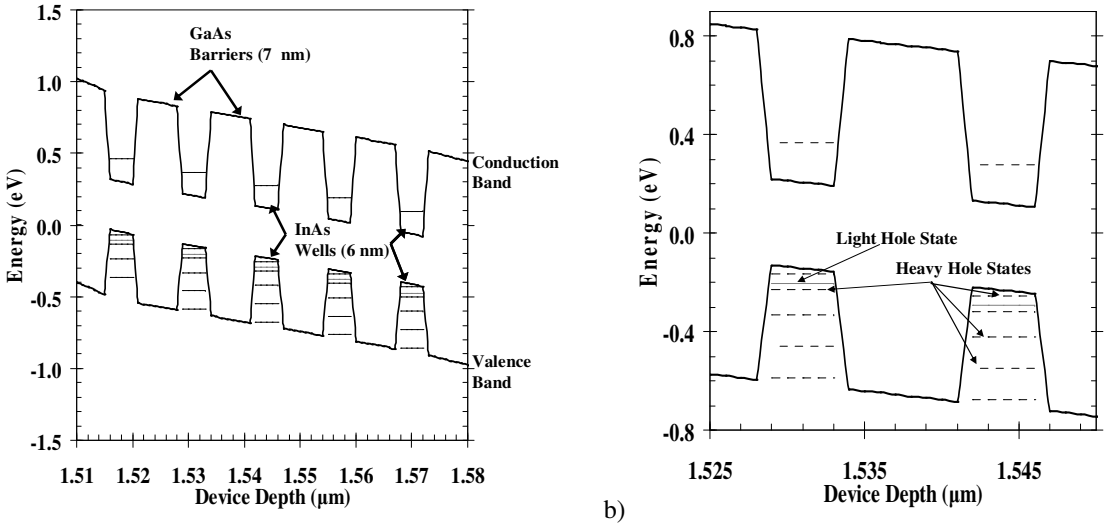

a) b)

Fig. 29. Band diagrams of InAs quantum wells in the i-layer of the GaAs p-i-n device. The following eigenstates are realized: one for conduction electrons, one for light holes, and five for heavy holes. The energy axis is referenced to the Fermi level.

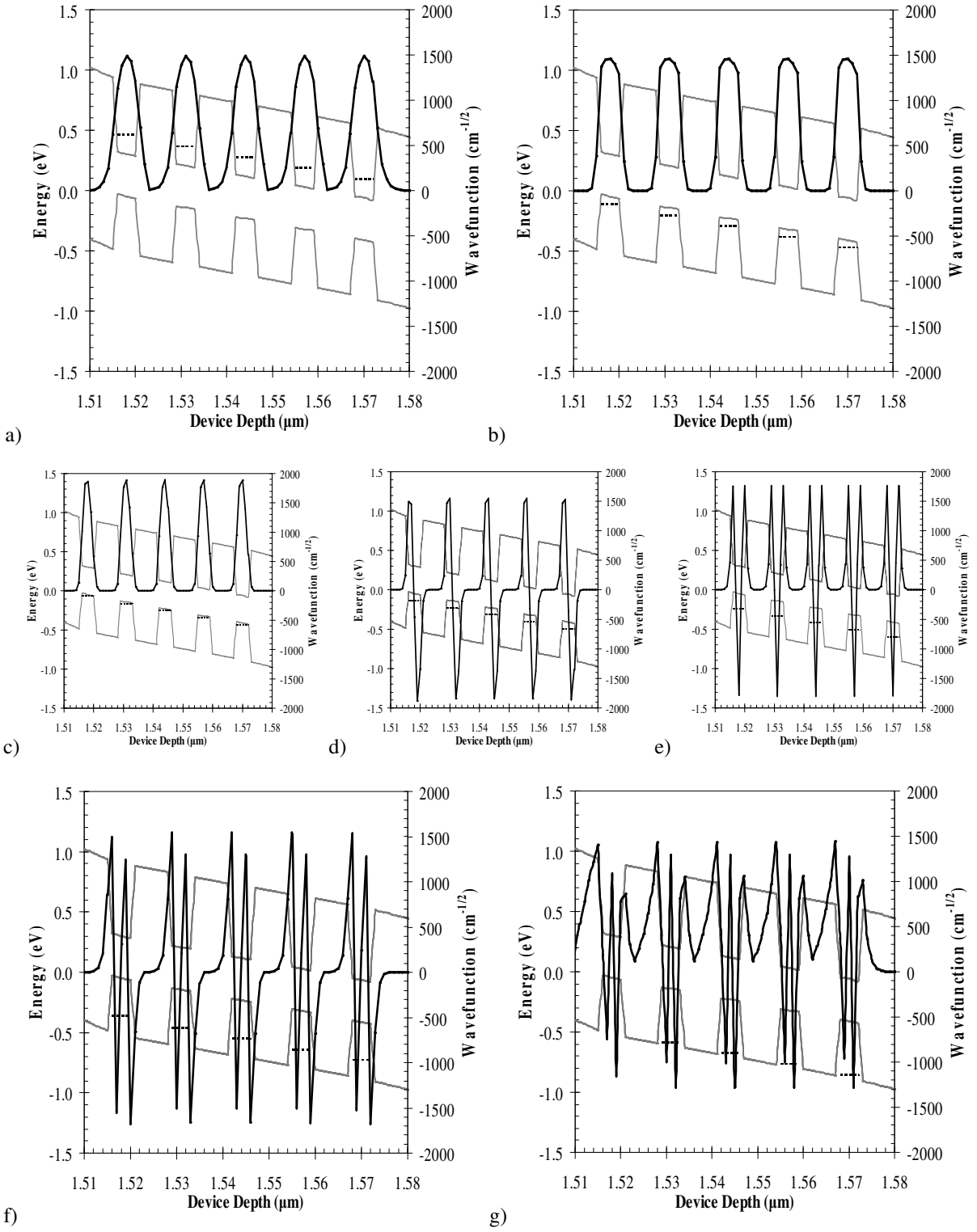

Fig. 30. Eigenfunctions superimposed over the band diagram corresponding to a) the single conduction electron state, b) the single light hole state, and c-g) each of the five heavy hole states.

It is interesting to compare the eigenvalue results of Fig. 29, which were obtained by solving the Schrödinger equation in each quantum well separately, with energy dispersions obtained by solving a Kronig-Penny like model (discussed in further detail in Appendix II). By solving for an energy dispersion, it is assumed that a mini-band forms due to the presence of the quantum wells. The electron energy dispersions for the 6 nm/7 nm well/barrier scheme (as in Fig. 29) is plotted in Fig. 31; the energy axis is with respect to the bottom of the bulk InAs conduction band. This indicates that there are, in fact, two bound states in the conduction band compared to the single bound state realized in Fig. 29. It is noted, however, that the second band in Fig. 31 is energetically located very close to the bottom of the GaAs conduction band at ~0.59 eV. Therefore, it is expected that this second band is effectively a quasi-continuum with the GaAs scattering states; this brings the results diagramed by Figs. 29 and 31 in very close agreement.

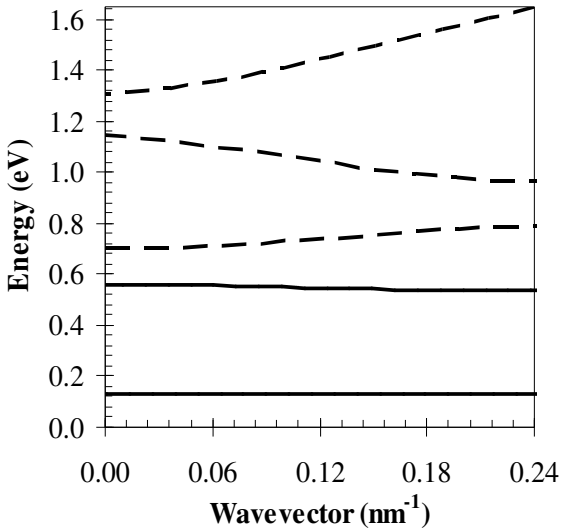

Fig. 31. Electron energy dispersion of the InAs superlattice formed by 6 nm InAs wells and 7 nm GaAs barriers. The solid bands indicate orbitals that fall within the GaAs bandgap; dashed bands indicate orbitals that overlap with the GaAs continuum. The energy axis is with respect to the bottom of the bulk InAs conduction band.

Regarding the realization of the intermediate band solar cell, it is important that there is a sufficient amount of coupling between the eigenstates of adjacent quantum structures. This coupling gives rise to a superlattice with its own energy dispersion [10, 17]. Therefore, the proper formation of a superlattice gives rise to an intermediate band within the bandgap of the host semiconductor as described in Section 2.4. A metric to determine possible formation of an intermediate band is by analyzing the overlap of wavefunctions between adjacent wells. Substantial overlap of carrier wavefunctions implies that a superlattice mini-band may form [10] thus acting as the desired intermediate band.

The electron wavefunction for 6 nm InAs wells is plotted in Fig. 32 while varying the barrier thickness from 10 nm to 2 nm. For the 10 nm and 9 nm trials, no wavefunction overlap is numerically visible; i.e. no overlap is seen down to ~10^{-6} $cm^{-1/2}$. At 8 nm and below, however, a substantial increase (at least eight orders of magnitude) in the amount of wavefunction overlap is observed. This indicates that for 6 nm InAs quantum confined structures in a GaAs host, a barrier of 8 nm or thinner is necessary for the formation of an intermediate band.

One of the standard methods for characterizing quantum dots is by analyzing their luminescent emissions. Based on the spontaneous emission model, Fig. 33 shows the electroluminescence of the p-i-n device due to varying thicknesses of the InAs wells. It is interesting to note that the literature indicates an electroluminescence of ~1050 nm for 6 nm quantum dots [4, 71]. The discrepancy arises, in part, due to the high strain inherent in quantum dots; however, this can be partially accounted for by the effective mass.

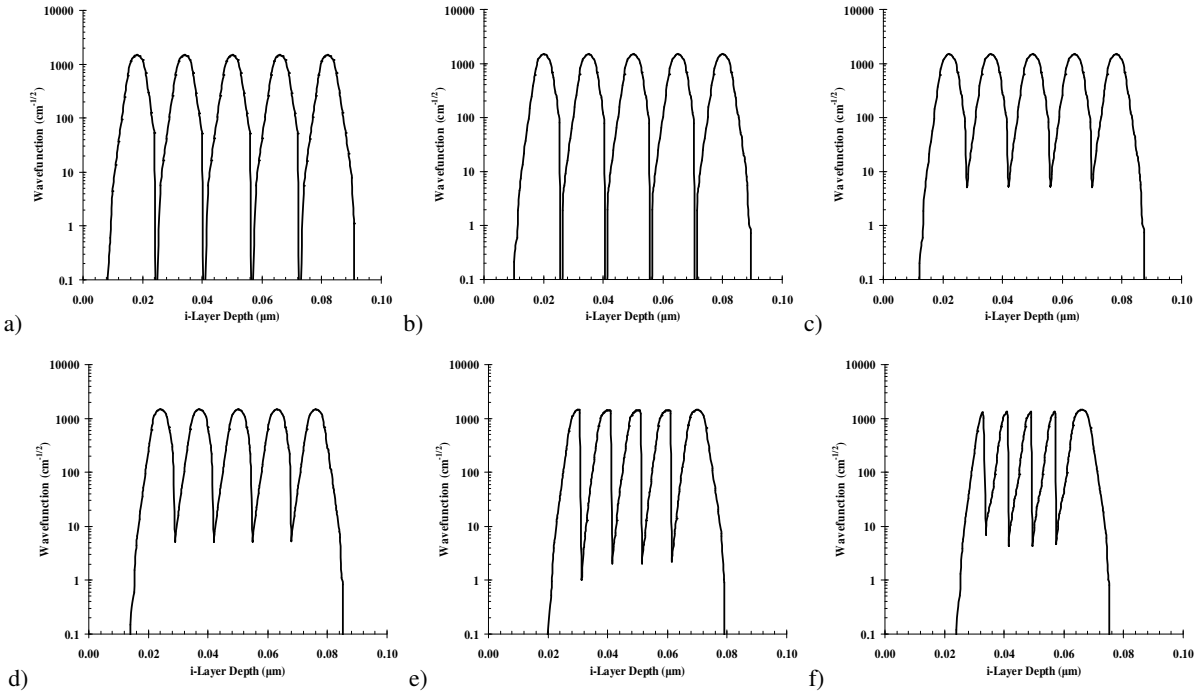

Fig. 32. Electron wavefunctions for 6 nm InAs quantum wells with a GaAs barrier thickness of a) 10 nm, b) 9 nm, c) 8 nm, d) 6 nm, e) 4 nm, and f) 2 nm. These plots imply that a barrier thickness of 8 nm or less is necessary for the formation of a superlattice mini-band.

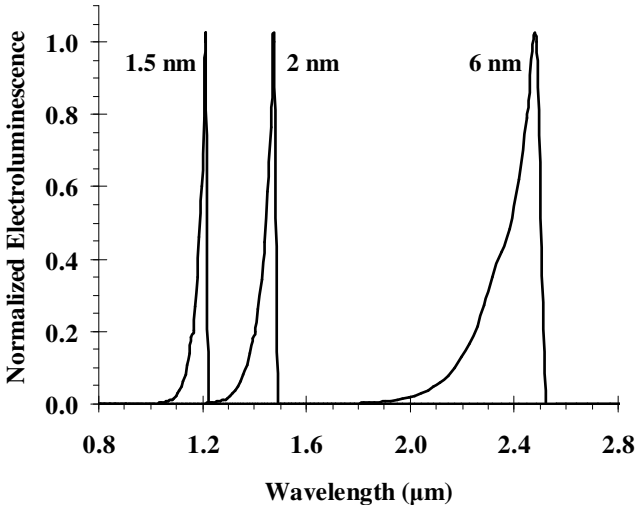

Fig. 33. Simulated electroluminescent spectra for several different InAs well thicknesses.

Chapter 4

Conclusion

In this work, modeling solutions necessary for the analysis of next generation photovoltaic devices have been presented. Specifically, the type of devices that are most relatable to this work will be made of inorganic semiconductors and will incorporate the use of nanostructures such as quantum wells and quantum dots. The detailed balance approach to solar photovoltaic efficiency, originated by Shockley and Queisser, has been invoked in this work to analyze and present the physical limits inherent to these novel devices. For a practical approach, the use of a commercially available device simulator was evaluated for the possible analyses of novel solar cell schemes.

The discussion of the detailed balance approach began with an overview of the original theory as formulated by Shockley and Queisser. The theory is thermodynamic in nature and has been amended throughout the years to conform to proper accounts of the non-equilibrium thermodynamics of the electron-photon interaction. This led to a generalization of the Planck law for blackbody radiation to also include the phenomena of luminescent radiation. This generalization along with the fundamental ideas put forth by Shockley and Queisser were invoked in this work to simulate the limiting performance of photovoltaic devices.

Using the detailed balance model, several examples were created to show the performance limits of the most basic solar cells and how such cells may be improved by innovative designs. A pedagogical analysis of the singe-junction solar cell was first presented to demonstrate the fundamental performance limits attributable to this simple design. This

culminated in showing the vast importance of materials selection as the detailed balance efficiency limit was shown to be strongly dependent on the semiconductor bandgap. The dependence of the detailed balance limit on solar concentration was also explored showing a logarithmic relation. A feature of this work, not seen in most treatments of the detailed balance analysis, is the use of the AM0, AM1.5G, and AM1.5D solar spectra, in addition to the standard use of the blackbody spectrum. Thus, the detailed balance limit was analyzed as it differs under different illuminating spectra.

The detailed balance model was then used in the analysis of a multi-junction solar cell. A method was derived in this work to numerically find the detailed balance limit of any given multi-junction cell. As a specific example, the triple-junction solar cell composed of InGaP, GaAs, and Ge sub-cells was introduced. The analysis showed that the efficiency limit could be significantly increased by simply reducing the bandgap of the GaAs sub-cell. It is, of course, not feasible to just switch the GaAs for a lower bandgap material due to the constraint of lattice matching; however, an effective reduction of bandgap may be possible by the introduction of a nanostructured array into the GaAs sub-cell. Therefore, this analysis serves as motivation for the implementation of such a design scheme.

The detailed balance model was finally used in the analysis of the intermediate band solar cell. Such a device can only be feasibly realized by means of nanostructures; specifically, quantum dots. As with the single-junction case, the analysis for the intermediate band solar cell was performed using the blackbody, AM0, AM1.5G, and AM1.5D solar spectra. This analysis showed how the detailed balance limit varies with the placement and location of the intermediate band within the bulk semiconductor bandgap. This information

serves as an indicator of the beneficial design space available in the implementation of an intermediate band device.

The detailed balance model has been successfully implemented in the analyses of the single-junction, triple-junction, and intermediate band solar cells. In regards to the triple-junction and intermediate band devices, the algorithm developed for this work is accurate albeit slow. Future work extending that which is presented here may focus on making the algorithms more efficient in their calculations. Such work would allow for rapid analysis of novel devices with the detailed balance method. Note that extra care must be paid attention to when dealing with Bose-Einstein integrals; it is not uncommon to witness shifts of several orders of magnitude in these integrals for milli-electron volt steps of the chemical potential. It may also be of interest to apply the detailed balance methodology to other novel solar cell design schemes such as hot carrier cells, multiple-carrier-generation devices, thermo-photovoltaics, *etc*. The effects of solar cell temperature dependence should also be investigated since it is sure to significantly increase under increased solar concentration.

The commercial device modeling package, Silvaco ATLAS, was utilized in the simulation of photovoltaic devices. This work evaluated the ability to use this software package for such simulations and relevant examples have been presented. The examples in this work aimed to simulate devices that are currently being fabricated at the Nanopower Research Laboratories. Optimum design of these devices has therefore been confirmed or recommended. Discussion of the device simulations began with an introduction and overview of the specific models that were invoked and the physics that they aim to describe. A discussion of the parameters of pertinent semiconductors was also presented.

The simulation of a GaAs single-junction solar cell was performed since it represents the baseline device that is being fabricated at the Nanopower Research Laboratories. For exemplary and pedagogical purposes, the device was presented before and after the inclusion of performance enhancing layers; namely, InGaP font and back surface fields. These layers have been shown to provide a significant enhancement to the device. The current solar cell design has also been shown to be currently optimized.

Building upon the single-junction device, the simulation of a dual-junction device was also performed. The design of this device added an InGaP sub-cell atop of the GaAs cell and was based off of devices fabricated at the Nanopower Research Laboratories. Unfortunately, the tunneling model provided does not seem able to properly handle the tunneling current necessary for the operation of the dual-junction device. This is in confirmation of previously reported work. In lieu of the weak tunneling model, a scheme has been presented to use the spectral response of the solar cell as the main simulation method. This has proved to be successful in this work and recommendations have been presented on the optimization of the InGaP-GaAs dual-junction cell.

Finally, a nanostructured solar cell was simulated by building upon the single-junction model. As an approximation to the InAs quantum dot devices currently being investigated, a quantum well model was invoked; i.e. InAs quantum wells were placed in the space charge region of the GaAs device model. This approach was justified and useful results were obtained and presented. Specifically, the properties of the eigenstates that arise due to quantum confinement were obtained giving rise to recommendations on the design of the nanostructured array. Unfortunately, a quantum mechanical model of photoabsorption does not exist in the software package. Such a model, rigorously derived from Fermi's golden

rule, would be necessary for the proper simulation of a nanostructured solar cell. Fortunately, a quantum mechanical model of spontaneous emission is present in the software package; thus electroluminescence arising from the quantum confined layers was presented as another possible analysis tool.

The Silvaco ATLAS device simulator has been shown to be able to simulate basic solar cell performance. From this, confirmation of and recommendations for device optimization have been presented. Challenges arise in the simulation of more advanced design schemes; this includes the ability to properly simulate tunneling effects, quantum mechanical photoabsorption, three-dimensional quantum effects (i.e. the zero-dimensional electron gas), *etc*. The ability to model such phenomena are necessary for the analyses of novel devices. In this regard, the software package utilized in this work is limited. Future work in device modeling and simulation may look into the tools being developed by the Computational Fluid Dynamics Research Corporation since their software is developed for the purpose of nano-device modeling. With that said, it may still be beneficial and worthwhile to reinvestigate certain aspects of the ATLAS simulations to see how far the software can be pushed. Such possible avenues to investigate include device simulation under increased solar concentration and the associated increased in device temperature.

This work has presented the use of computer-assisted numerical modeling for the simulation and analysis of novel solar cell design concepts. Such an approach is beneficial for two primary reasons. First, it is important to know the theoretical limits towards which one is working towards. This helps to support motivation for the experimental work to be undertaken and gives an accurate gauge of how the work is progressing. Second, realistic, physical device simulations enable for the analysis and possible optimization of experimental

devices without the need for physically making said devices. This allows for the crucial saving of resources by performing only the experiments and fabrications that are truly necessary. It is hopeful that this work may serve as a guide to the next series of modeling and simulation efforts that will aid in the development of novel photovoltaic devices and that the analyses performed herein will aid in their experimental realization.

Appendix I

Justification of the Effective Mass Schrödinger Equation

In Section 3.11, the effective mass Schrödinger equation was introduced:

$$-\frac{\hbar^2}{2}\nabla\cdot\frac{1}{m}\nabla\Psi+V\Psi=E\Psi\,. \tag{1}$$

where $\hbar$ is the reduced Planck's constant, m is the effective mass, V is the potential energy, and E is the total energy. This differs from the usual form of the time-independent Schrödinger equation

$$-\frac{\hbar^2}{2m}\nabla^2\Psi+V\Psi=E\Psi \tag{2}$$

by breaking apart the Laplacian into two separate differential operators and by the differentiation of the effective mass. The justification for doing so is that the kinetic energy term in (2) is no longer Hermitian when the problem at hand presents a spatially-varying effective mass; the kinetic energy term in (2) is therefore not physically plausible. The form of the kinetic energy in (1), however, is Hermitian and is widely employed in the analysis of semiconductor heterostructures where a spatially-variant effective mass is common [72-74].

Consider the form of the kinetic energy given in (2):

$$T=-\frac{\hbar^2}{2m}\nabla^2\,. \tag{3}$$

This is the usual form of the kinetic energy and will now be shown to be non-Hermitian in the presence of a spatially-dependant effective mass. In general, the reciprocal effective mass is tensorial; so (3) in tensor notation is

$$T = -\frac{\hbar^2}{2} m_{ij}^{-1} \frac{\partial^2}{\partial x_i^2} \tag{4}$$

where m^{-1}_{ij} is the reciprocal effective mass tensor and Einstein summation is invoked. Then for arbitrary states $|f>$ and $|g>$ the following inner product may be calculated:

$$\langle f | Tg \rangle = -\frac{\hbar^2}{2} \int f^* m_{ij}^{-1} \frac{\partial^2 g}{\partial x_i^2} dx_i \,. \tag{5}$$

Integrating by parts and over all space:

$$\langle f | Tg \rangle = \frac{\hbar^2}{2} \int \left(\frac{\partial f^*}{\partial x_i} m_{ij}^{-1} + f^* \frac{\partial m_{ij}^{-1}}{\partial x_i} \right) \frac{\partial g}{\partial x_i} dx_i \tag{6}$$

where the boundary term has been excluded since it vanishes. A second integration yields

$$\begin{aligned} \langle f | Tg \rangle &= -\frac{\hbar^2}{2} \int \frac{\partial^2}{\partial x_i^2} \left(m_{ij}^{-1} f^* \right) g dx_i \\ &= \left\langle mT \frac{f}{m} \middle| g \right\rangle \\ &\neq \langle Tf | g \rangle \end{aligned} \tag{7}$$

QED.

Now consider the form of the kinetic energy given by (1):

$$T = -\frac{\hbar^2}{2} \nabla \cdot \frac{1}{m} \nabla \,, \tag{8}$$

or in tensor notation:

$$T = -\frac{\hbar^2}{2} \frac{\partial}{\partial x_i} \left(m_{ij}^{-1} \frac{\partial}{\partial x_i} \right). \tag{9}$$

This form of the kinetic energy operator will now be shown to be Hermitian. For arbitrary states $|f>$ and $|g>$ the following inner product may be calculated:

$$\begin{aligned} \langle f | Tg \rangle &= -\frac{\hbar^2}{2} \int f^* \frac{\partial}{\partial x_i} \left(m_{ij}^{-1} \frac{\partial g}{\partial x_i} \right) dx_i \\ &= -\frac{\hbar^2}{2} \int f^* \left(\frac{\partial m_{ij}^{-1} \partial g}{\partial x_i^2} + m_{ij}^{-1} \frac{\partial^2 g}{\partial x_i^2} \right) dx_i \end{aligned} \tag{10}$$

Integrating the second term, by parts, over all space and excluding the vanishing boundary term yields

$$\langle f | Tg \rangle = \frac{\hbar^2}{2} \int \frac{\partial f^*}{\partial x_i} m_{ij}^{-1} \frac{\partial g}{\partial x_i} dx_i \, . \tag{11}$$

Integrating once more by parts:

$$\begin{aligned} \langle f | Tg \rangle &= -\frac{\hbar^2}{2} \int \frac{\partial}{\partial x_i} \left(m_{ij}^{-1} \frac{\partial f^*}{\partial x_i} \right) g dx_i \\ &= \langle Tf | g \rangle \end{aligned} \tag{12}$$

QED.

Appendix II

Bandstructure Calculations with a Kronig-Penny–Like Model

In Section 3.19 the energy eigenvalues that were obtained by the ATLAS device simulator were compared to the energy dispersion obtained by solving the Schrödinger equation for a simple periodic potential. The following elaborates on the method specific to this work for performing such calculations of the energy dispersion.

The celebrated Kronig-Penney model [75] presents a solution to the Schrödinger equation

$$-\frac{\hbar^2}{2m}\nabla^2\Psi + V\Psi = E\Psi \tag{1}$$

for a simple periodic potential as diagramed in Fig. 1. The textbook solutions [13, 44] to this model take the form of two transcendental equations:

$$\begin{aligned} \cos k(a+b) &= \frac{Q^2-K^2}{2QK}\sinh(Qb)\sin(Ka) + \cosh(Qb)\cos(Ka) \qquad E < V_0 \\ \cos k(a+b) &= -\frac{\beta^2+K^2}{2\beta K}\sin(\beta b)\sin(Ka) + \cos(\beta b)\cos(Ka) \qquad E > V_0 \end{aligned} \tag{2}$$

where K, Q, and β are local wavevectors such that

$$\begin{aligned} K^2 &= \frac{2mE}{\hbar^2} && V = 0, \quad \forall E \\ Q^2 &= \frac{2m(V_0-E)}{\hbar^2} && V = V_0, \quad E < V_0 \\ \beta^2 &= \frac{2m(E-V_0)}{\hbar^2} && V = V_0, \quad E > V_0 \end{aligned} \tag{3}$$

and k is the wavevector of the Bloch function such that the energy dispersion is

$$E(k) = \frac{\hbar^2 k^2}{2m}. \tag{4}$$

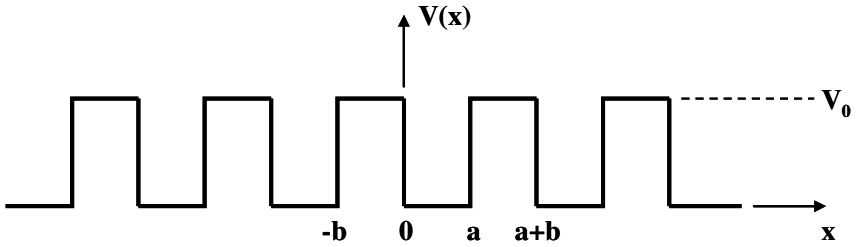

Fig. 1. Kronig-Penney square well potential that gives rise to energy bands in the solution of the Schrödinger equation. The potential is periodic to ±∞.

Therefore, an energy bandstructure *E(k)* may be constructed from (4) where *k* is determined by (2) and the dimensions of the potential given in Fig. 1. This potential is clearly an oversimplification for the situation of a real crystal and therefore would not be useful in such an analysis. The case of a nanostructured superlattice, however, can be approximated by this relatively simple potential. This has previously been presented in Section 1.4. Therefore, the Kronig-Penney model becomes useful to approximate a superlattice and lends itself to such analysis as is necessary for the consideration of minibands or intermediate bands.

The problem with the textbook solutions of the Kronig-Penny model is that the mass in (1) is inherently assumed to be constant. In the analysis of a real nanostructured system, the effective masses of charge carriers will generally differ whether one is concerned with the nanostructured well region or the quasi-bulk barrier region. As discussed in Appendix I, (1) becomes invalid in the presence of a spatially-varying effective mass and is thus superseded by the effective mass wave equation

$$-\frac{\hbar^2}{2}\nabla\cdot\frac{1}{m^*}\nabla\Psi + V\Psi = E\Psi \tag{5}$$

where the effective mass has the value $m^* = m_w$ when then wavefunction is analyzed in a well region ($V = 0$) and the value $m^* = m_b$ when then wavefunction is analyzed in a barrier

region ($V = V_0$). Therefore, with the modified form of the wave equation in place, it is not unreasonable to suspect that the textbook solutions of (2) do not properly address the case of a real nanostructured superlattice and that a different solution must be derived.

First consider the case that $E < V_0$. For the potential specified in Fig. 1, the solution of (5) takes the form

$$\begin{aligned} \Psi &= Ae^{iKx} + Be^{iKx} \qquad 0 < x < a \\ \Psi &= Ce^{Kx} + De^{Kx} \qquad -b < x < 0 \end{aligned} \tag{6}$$

where the wavevectors are modified from (3) as

$$\begin{aligned} K^2 &= \frac{2m_w E}{\hbar^2} \\ Q^2 &= \frac{2m_b (V_0 - E)}{\hbar^2} \end{aligned} \tag{7}$$

At $x = 0$, the standard quantum mechanical boundary condition, continuity of Ψ, is invoked yielding

$$A + B = C + D\,. \tag{8}$$

The other usual boundary condition, continuity of $d\Psi/dx$, is, however, invalid. In using the effective mass equation, the boundary condition requires the continuity of $(m^*)^{-1}d\Psi/dx$ [72-73]. This yields

$$i\frac{KA}{m_w} - i\frac{KB}{m_w} = \frac{QC}{m_b} - \frac{QD}{m_b}\,. \tag{9}$$

The wavefunction in the region $a < x < a+b$ is given by (6) and the Bloch theorem:

$$\Psi(a < x < a + b) = \Psi(-b < x < 0)e^{ik(a+b)} \tag{10}$$

Then by invoking the proper quantum mechanical boundary conditions at $x = a$:

$$Ae^{iKa} + Be^{-iKa} = Ce^{-Qb}e^{ik(a+b)} + De^{Qb}e^{ik(a+b)} \tag{11}$$

$$i\frac{KA}{m_w}e^{iKa} - i\frac{KB}{m_w}e^{-iKa} = \frac{QC}{m_b}e^{-Qb}e^{ik(a+b)} - \frac{QD}{m_b}e^{Qb}e^{ik(a+b)}. \tag{12}$$

Equations (8), (9), (11), and (12) represent four equations containing four unknowns (*A, B, C,* and *D*). These equations may be written homogeneously; then a theorem from linear algebra states that for a non-trivial solution to occur, the determinant of the coefficients of *A, B, C,* and *D* must vanish; very tedious algebra yields

$$\cos k(a+b) = \frac{Q^2m_w^2 - K^2m_b^2}{2QKm_wm_b}\sinh(Qb)\sin(Ka) + \cosh(Qb)\cos(Ka). \tag{13}$$

For the case $E > V_0$, the wavefunction in (6) for $0 < x < a$ is used in conjunction with the new wavefunction for $-b < x < 0$,

$$\Psi = Ce^{i\beta x} + De^{-i\beta x} \qquad -b < x < 0 \tag{14}$$

where the wavevector β is modified from (3) as

$$\beta^2 = \frac{2m_b(E - V_0)}{\hbar^2}. \tag{15}$$

The wavefunction from (14) then satisfies the Bloch theorem and may be substituted into (10). Similar to the foregoing example, application of the appropriate quantum mechanical boundary conditions yield

$$A + B = C + D \tag{16}$$

$$\frac{KA}{m_w} - \frac{KB}{m_w} = \frac{QC}{m_b} - \frac{QD}{m_b} \tag{17}$$

$$Ae^{iKa} + Be^{-iKa} = Ce^{-i\beta b}e^{ik(a+b)} + De^{i\beta b}e^{ik(a+b)} \tag{18}$$

$$\frac{KA}{m_w}e^{iKa} - \frac{KB}{m_w}e^{-iKa} = \frac{QC}{m_b}e^{-i\beta b}e^{ik(a+b)} - \frac{QD}{m_b}e^{i\beta b}e^{ik(a+b)}. \tag{19}$$

Then by the same argument as the foregoing example, the transcendental solution is

$$\cos k(a+b) = -\frac{\beta^2 m_w^2 + K^2 m_b^2}{2\beta K m_w m_b}\sin(\beta b)\sin(Ka) + \cos(\beta b)\cos(Ka)\,. \qquad (20)$$

Therefore, the energy bandstructure *E(k)* of a nanostructured superlattice that is approximated by the potential in Fig. 1 may be calculated from (4). The wavevector k is determined by the transcendental equations (13) and (20); these are eigenvalue solutions of the effective mass Schrödinger equation (5) for the Kronig-Penny periodic potential. The appropriate local wavevectors are given by (7) and (15). It is important to note that the solutions of the effective mass equation, (13) and (20), reduce to the solutions of the standard wave equation, (2), in the limit that $m_w = m_b$.

In Section 13.9, an InAs nanostructured system within a GaAs host was discussed. In that system, the InAs confined regions were considered to be 6 nm thick while the maximum desired GaAs barrier thickness was determined to be 7 nm. The analysis in that section also resulted in an energy difference of ~0.59 eV between the conduction bands of GaAs and InAs. In reference to Fig. 1, the constants are thus $a = 6$ *nm,* $b = 7$ *nm,* and $V_0 = 0.59$ *eV*. The electron effective masses presented in Section 3.14 for InAs and GaAs are $m_w = 0.67m_0$ and $m_b = 0.024m_0$, respectively, where m_0 is the rest mass of the electron. These parameters yield the conduction band energy dispersion in Fig. 2.a. Solid bands represent states that have $E < V_0$ and are solutions from (13); dashed bands are quasi-continuum states as these orbitals overlap with the GaAs continuum.

The analysis in Section 13.9 based on ATLAS device simulations showed that, for the nanostructured system discussed above, there was exactly one conduction band eigenstate. The location of the energy eigenlevel for that state is at approximately the same level as the first band in the energy dispersion of Fig. 2.a. It is also noted that the top of the second band of the energy dispersion is energetically located extremely close to the GaAs continuum.

Therefore it is foreseeable that the existence of a second eigenstate is just cut-off and would exist for a slightly larger conduction band difference between GaAs and InAs.

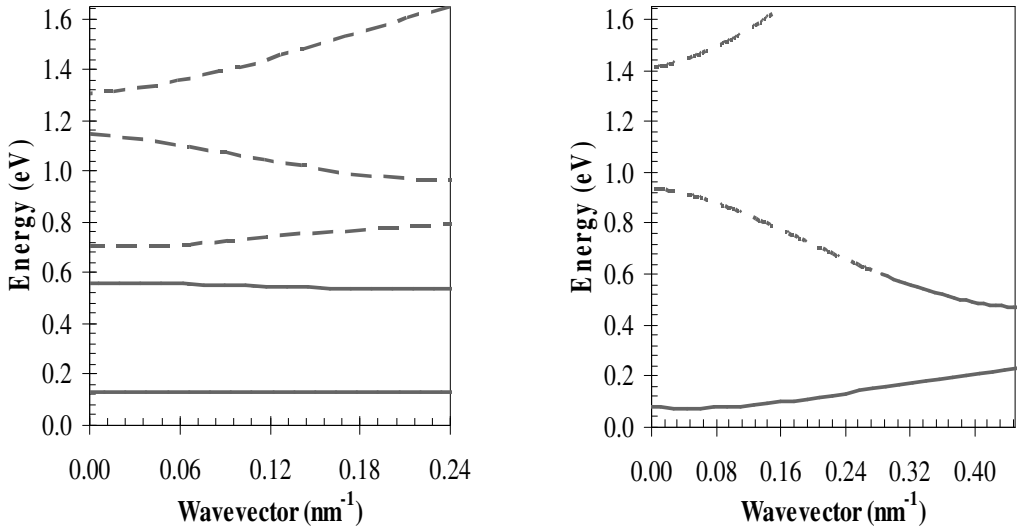

Fig. 2. Conduction band energy dispersion of an InAs/GaAs (confined/barrier) superlattice with InAs thickness of 6 nm and GaAs thickness of a) 7 nm and b) 1 nm. Solid bands represent states that are within the GaAs bandgap while dashed bands represent states that overlap with the GaAs continuum. The energy ordinate is taken with respect to the bottom of the bulk InAs conduction band.

It is instructive to decrease the barrier thickness of the discussed system to *b = 1 nm.* The modified energy dispersion is thus plotted in Fig. 2.b. As is expected, the energy bands widen due to the increased coupling of wavefunctions. Additionally, the second band now overlaps with the GaAs continuum essentially making it a quasi-continuum band. Since the first energy band has already been identified as the band of interest, it is worthwhile to analyze it further.

Ideally, the bottommost band in the superlattice energy dispersions will play the role of the miniband that is formed as a result of the creation of a nanostructure superlattice. In the case of the device described in Section 2.4, this can be the intermediate band of the

intermediate band solar cell. In that analysis, the placement of the intermediate band was shown to be of the utmost importance. Not considered, however, is the fact than a real intermediate band will posses some finite width. This may prove important in future analyses since an operational requirement of the intermediate band solar cell is the states in the intermediate band are only half-filled with electron [76]. Therefore, knowledge of the width of the intermediate band becomes important. Following from Fig. 2, several iterations of energy dispersion solutions yields a trend showing the variation of miniband width with barrier width as seen in Fig. 3. This information exemplifies the increased coupling that accompanies decreased barriers and may be useful in direct tuning of the miniband.

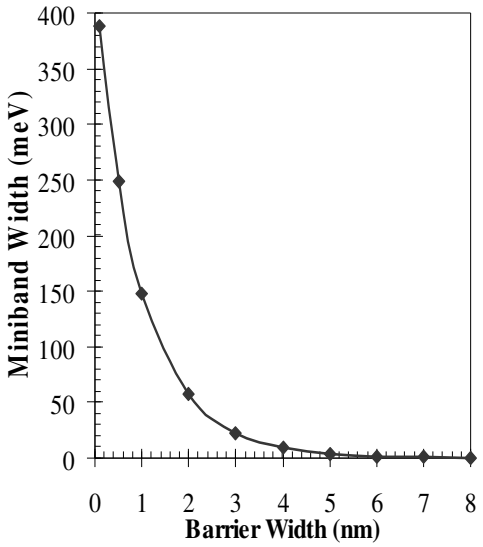

Fig. 3. The decrease in barrier width gives rise to an asymptotic increase in the width of the miniband. This is due to the larger degree of wavefunction overlap that occurs for decreasing barrier widths.

Appendix III

Bandstructure Calculations (MATLAB Code)

The following code consists of two m-files (*kp0.m* and *kp1.m*) that allow for the generation of superlattice bandstructures based of off a Kronig-Penney like model as described in Appendix II. The first file (*kp0.m*) generates a plot of the right hand sides of (II.13) and (II.20) vs. energy. This is a visual tool as the allowed energy bands will exist only when the right hand side of the Kronig-Penney solution is between -1 and 1. From this visual aid, a range of energies may be determined and serve as the input t*o kp1.m*.

The second file (*kp1.m*) plots the energy dispersion. This file takes several energy ranges as an input and plots the allowed bands in those energy ranges. These energies are determined from the visual aid plotted by *kp0.m*.

```
%%% kp0.m
%%% Run this code to find the allowed energy ranges and transfer them to
%%% kp1.m.

hb = 6.626068e-34 / (2*pi);   % Reduced Planck's Const
kB = 1.3806503e-23;   % Boltzmann's Const
q = 1.60217646e-19;   % Elementary charge

mw = 0.024 * 9.10938e-31;   % Well effective mass
mb = 0.067 * 9.10938e-31;   % Barrier effective mass
U = 0.59*q;   % Band offset
a = 6e-9;   % Well width
b = 7e-9;   % Barrier width

z = 1000;   %No. of data points to consider
E = linspace(0.001*U,3*U,z);   % Energy range to consider

K = sqrt(2*mw*E)/hb;   % Well wavevector
Q = sqrt(2*mb*(U-E))/hb;   % Barrier wavevector (E < U)
B = sqrt(2*mb*(E-U))/hb;   % Barrier wavevector (E > U)

for I = 1:length(E);
    if E(I) <= U;            % Kronig-Penny RHS (E < U)
        rhsA(I) = ((Q(I)^2 * mw^2 - K(I)^2 * mb^2) / (2*Q(I)*K(I)*mw*mb))
.* sinh(Q(I)*b) .* sin(K(I)*a) + cosh(Q(I)*b) .* cos(K(I)*a);
        rhsB(I) = NaN;
    else
        rhsA(I) = NaN;       % Kronig-Penny RHS (E > U)
        rhsB(I) = -((B(I)^2 * mw^2 + K(I)^2 * mb^2) / (2*B(I)*K(I)*mw*mb))
.* sin(B(I)*b) .* sin(K(I)*a) + cos(B(I)*b) .* cos(K(I)*a);
    end
end

E = E / q;

plot(E,rhsA,'.-', E,rhsB,'.-')
xlabel('Energy (eV)'); ylabel('Kronig-Penny RHS')
```

```
%%% kp1.m
%%% Run this code following kp0.m in order to accurately plot the bands.

hb = 6.626068e-34 / (2*pi);   % Reduced Planck's Const
kB = 1.3806503e-23;   % Boltzmann's Const
q = 1.60217646e-19;   % Elementary charge

mw = 0.024 * 9.10938e-31;   % Well effective mass
mb = 0.067 * 9.10938e-31;   % Barrier effective mass
U = 0.59*q;   % Band offset
a = 6e-9;   % Well width
b = 7e-9;   % Barrier width

%%%% Energy range to consider; refine as per kp0.m results. %%%%
%%%% Any number of distinct energy ranges may be entered.
E1 = linspace(0.126*q,0.129*q,1000);
E2 = linspace(0.5*q,0.6*q,1000);
E3 = linspace(0.68*q,.8*q,1000);
E4 = linspace(0.9*q,1.2*q,1000);

E = [E1 E2 E3 E4];
%%%%%%%%%%%%%%%%%%%%%%%%%%%%%%%%%%%%%%%%%%%%%%%%%%%%%%%%%%%%%%%%%%%%%%%

K = sqrt(2*mw*E)/hb;   % Well wavevector
Q = sqrt(2*mb*(U-E))/hb;   % Barrier wavevector (E < U)
B = sqrt(2*mb*(E-U))/hb;   % Barrier wavevector (E > U)

for I = 1:length(E);
    if E(I) <= U;            % Kronig-Penny RHS (E < U)
        rhsA(I) = ((Q(I)^2 * mw^2 - K(I)^2 * mb^2) / (2*Q(I)*K(I)*mw*mb))
.* sinh(Q(I)*b) .* sin(K(I)*a) + cosh(Q(I)*b) .* cos(K(I)*a);
        rhsB(I) = NaN;
        if abs(rhsA(I)) > 1;
            rhsA(I) = NaN;
        end
    else
        rhsA(I) = NaN;       % Kronig-Penny RHS (E > U)
        rhsB(I) = -((B(I)^2 * mw^2 + K(I)^2 * mb^2) / (2*B(I)*K(I)*mw*mb))
.* sin(B(I)*b) .* sin(K(I)*a) + cos(B(I)*b) .* cos(K(I)*a);
        if abs(rhsB(I)) > 1;
            rhsB(I) = NaN;
        end
    end
end

% Wavevector
kA = (a+b)^(-1) * acos(rhsA) * 1e-9;   %E < U
kB = (a+b)^(-1) * acos(rhsB) * 1e-9;   %E > U

E = E / q;

plot(kA,E,'.-', kB,E,'.-')
xlabel('Wavevector (nm^-^1)'); ylabel('Energy (eV)')
```

Appendix IV

Detailed Balance Model for a Single-Junction Solar Cell (MATLAB Code)

The following code consists of one m-file (*db-single.m*) that invokes the detailed balance model for the analysis of a single-junction solar cell as discussed in Section 2.2. The standard inputs are solar and device temperatures, material bandgap, and solar concentration factor. The routine is setup to allow for the analysis to use the blackbody, AM0, AM1.5G, or AM1.5D solar spectra. Upon running the routine, a current-voltage plot is generated and the detailed balance efficiency limit is printed to the command window.

```
% db-single.m
% Single cell detailed balance calculation using either blackbody or ASTM
% solar spectrums.

q=1.6021765e-19; h=6.626069e-34; c=299792458; k=1.38065e-23;
sigma=5.6704e-8; f=2.1646e-5;
Ts=6000; Tc=300; Eg=1.89; C=1;   % Tunable paramters; Eg in eV, C is solar
conc.
spec=1;   % Enter 0 for blackbody, 1 for AM0, 2 for AM1.5G, or 3 for
AM1.5D
V=linspace(0,Eg,400);

% This section chooses the correct solar spectrum and calculates Isc
if spec==0;
    specFluxS = @(E) 2*pi/(h^3*c^2) * E.^2 ./ (exp(E/(k*Ts)) - 1);
    Ps=C*f*sigma*Ts^4*1e-1;   % Solar irradiance (mW/cm2)
    Isc = q * C*f * quadgk(specFluxS, Eg*q, 22*q);   % Short-circuit
current
else
    load spectrumFlux   % ASTM spectral fluxs (photons/m2/s/nm),
wavelength (nm)
    if spec==1;
        specFluxS=AM0; lam=lam0; Ps=C*136.61;   % Solar irradiance
(mW/cm2)
    elseif spec==2;
        specFluxS=AM1p5G; lam=lam1p5; Ps=C*100.04;
    elseif spec==3;
        specFluxS=AM1p5D; lam=lam1p5; Ps=C*90.014;
    else
        disp('Incorrect option for solar spectrum!')
        clear AM0 AM1p5G AM1p5D lam0 lam1p5;
        return
    end
    clear AM0 AM1p5G AM1p5D lam0 lam1p5;
    lamG = h*c / (Eg*q) * 1e9;   % Wavelength (nm) corresponding to Eg
    maxPt = find(lam<=lamG, 1, 'last');   % Location of lamG in lam vector
    Isc = q*C * trapz(lam(1:maxPt), specFluxS(1:maxPt));   % Short-circuit
current
end

% This section calculates the dark and total currents
z=1; Id=zeros(1,length(V)); I=Id;   % Preallocations
while z<length(V);
    specFluxC = @(E) 2*pi/(h^3*c^2) * E.^2 ./ (exp( (E - (q*V(z)))/(k*Tc)
) - 1);
    Id(z) = -q * quadgk(specFluxC, Eg*q, 10*q);   % Dark current
    I(z) = (Isc+Id(z)) * 1e-1;   % Total current in mA/cm2
    if I(z)<0;
        I(z+1:length(I)) = NaN;
        z=length(V);   % Terminate calculations after reacing Voc
    else
        z=z+1;
    end
end

eff = 100*max(V.*I)/(Ps);   % Solar efficiency
```

```
disp('Maximum Efficiency (%):'); disp(eff);

plot(V,I); axis([0 Eg 0 2^nextpow2(I(1))]);
xlabel('Voltage (V)'); ylabel('Current (mA/cm^2)')
```

Appendix V

Detailed Balance Model for a Triple-Junction Solar Cell (MATLAB Code)

The following code consists of two m-files (*db-triple.m* and *currentMatchTriple.m*) that together invoke the detailed balance model for the analysis of a triple-junction solar cell as discussed in Section 2.3. The standard inputs are solar and device temperatures, solar concentration factor, and different semiconductor bandgaps corresponding to the different junctions in the multi-junction device. In the case of the bandgaps, a range of bandgaps may be entered for each junction. This allows for the generation of efficiency contours as presented in Section 2.3. The routine is setup to allow for the analysis to use the blackbody, AM0, AM1.5G, or AM1.5D solar spectra. Upon running the routine, the detailed balance efficiency limit, as well as the values of the current and voltage and that operating point, are saved in separate matrices for pertinent post-processing analysis.

The file *db-triple.m* is the master routine and calls upon *currentMatchTriple.m* as part of the routine. User-entered inputs and machine storage of pertinent data occurs in *db-triple.m*. This routine also loops through each permutation of bandgaps, each time passing the current permutation to *currentMatchTriple.m.* The *currentMatchTriple.m* routine numerically solves the detailed balance model for the given bandgap permutation.

```
% db-triple.m
% This routine takes a ranges of each of three bandgaps and determines the
% maximum efficiency at each location

q=1.6021765e-19; h=6.626069e-34; c=299792458; k=1.38065e-23;
sigma=5.6704e-8; f=2.1646e-5;
Ts=6000; Tc=300; C=1;   % Tunable paramters
spec=0;   % Enter 0 for blackbody, 1 for AM0, 2 for AM1.5G, or 3 for
AM1.5D
% Solar spectral flux
specFluxS = @(E) 2*pi/(h^3*c^2) * E.^2 ./ (exp(E/(k*Ts)) - 1);

% Define ranges for Eg1-top, Eg2-middle, Eg3-bottom
rangeEg1 = 1.5 : 0.02 : 2;
rangeEg2 = 0.7 : 0.02 : 1.5;
rangeEg3 = 0.2 : 0.02 : 0.7;

if spec ~= 0
    load spectrumFlux
end

% Fraction of the bandgap to pass to the lower limit of the chemical
% potential sweeps
A=0.5; B=0.8;   % Values corresponding to the cases of C=1 and C=1/f
fr = (A - B) * (log(C) / log(f)) + A;

% Pre-allocatons
Isc = zeros(length(rangeEg1), length(rangeEg2), length(rangeEg3));
Ival1=Isc; Ival2=Isc; Vval1=Isc; Vval2=Isc; effVal1=Isc; effVal2=Isc;

% Loop through bandgap values and determine efficiencies
for w = 1:length(rangeEg1)
    Eg1 = rangeEg1(w);
    for e = 1:length(rangeEg2)
        Eg2 = rangeEg2(e);
        for r = 1:length(rangeEg3)

            Eg3 = rangeEg3(r);

            % Find the efficiency values
            currentMatchTriple

            % Store values corresponding to the minimum delta
            Ival1(w,e,r) = Imax(1);
            Vval1(w,e,r) = Vmax(1);
            effVal1(w,e,r) = eff(1);

            % Store values corresponding to the maximum power at 1% error
            Ival2(w,e,r) = Imax(2);
            Vval2(w,e,r) = Vmax(2);
            effVal2(w,e,r) = eff(2);

            % Store short circuit current
            Isc(w,e,r) = ILmin;
```

```
        end

        % Interim save of pertinant values
        save finalBB Ival1 Ival2 Vval1 Vval2 effVal1 effVal2 Isc rangeEg1
rangeEg2 rangeEg3

    end
end

disp('Simulation complete!  =]')

if spec ~= 0
    clear AM0 AM1p5D AP1p5G lam0 lam1p5
end
```

```
% currentMatchTriple.m
% At a given set of triple junction bandgaps, this routine determines the
% maximum efficiency of the stack with respect to the constraint of
current
% matching

% ... called by db-triple.m

% Find the wavelengths (nm) corresponding to the tandem bandgaps for use
% with the ASTM spectra
if spec ~= 0
    lam1 = h*c / (Eg1*q) * 1e9;
    lam2 = h*c / (Eg2*q) * 1e9;
    lam3 = h*c / (Eg3*q) * 1e9;
end

% Short-circuit currents - 1: Top Cell,  2: Middle Cell,  3: Bottom Cell
switch spec
    case 0   % Blackbody
        IL1 = q*C*f * quadgk(specFluxS,q*Eg1, q*22);
        IL2 = q*C*f * quadgk(specFluxS,q*Eg2, q*Eg1);
        IL3 = q*C*f * quadgk(specFluxS,q*Eg3, q*Eg2);
        Ps = C*f*sigma*Ts^4;
    case 1   % AM0
        maxPt1 = find(lam0<=lam1, 1, 'last');
        maxPt2 = find(lam0<=lam2, 1, 'last');
        maxPt3 = find(lam0<=lam3, 1, 'last');
        IL1 = q*C * trapz(lam0(1:maxPt1), AM0(1:maxPt1));
        IL2 = q*C * trapz(lam0(maxPt1:maxPt2), AM0(maxPt1:maxPt2));
        IL3 = q*C * trapz(lam0(maxPt2:maxPt3), AM0(maxPt2:maxPt3));
        Ps = C*1366.1;
    case 2   % AM1.5G
        maxPt1 = find(lam1p5<=lam1, 1, 'last');
        maxPt2 = find(lam1p5<=lam2, 1, 'last');
        maxPt3 = find(lam1p5<=lam3, 1, 'last');
        IL1 = q*C * trapz(lam1p5(1:maxPt1), AM1p5G(1:maxPt1));
        IL2 = q*C * trapz(lam1p5(maxPt1:maxPt2), AM1p5G(maxPt1:maxPt2));
        IL3 = q*C * trapz(lam1p5(maxPt2:maxPt3), AM1p5G(maxPt2:maxPt3));
        Ps = C*1000.4;
    case 3   % AM1.5D
        maxPt1 = find(lam1p5<=lam1, 1, 'last');
        maxPt2 = find(lam1p5<=lam2, 1, 'last');
        maxPt3 = find(lam1p5<=lam3, 1, 'last');
        IL1 = q*C * trapz(lam1p5(1:maxPt1), AM1p5D(1:maxPt1));
        IL2 = q*C * trapz(lam1p5(maxPt1:maxPt2), AM1p5D(maxPt1:maxPt2));
        IL3 = q*C * trapz(lam1p5(maxPt2:maxPt3), AM1p5D(maxPt2:maxPt3));
        Ps = C*900.14;
    otherwise
        disp('Invalid entry for the solar spectrum!!!')
        return
end

% Short-circuit current of full stack
ILmin = min( [IL1 IL2 IL3] );

% Values of chemical potentials to sweep through
```

```
rangeMu1 = q * (fr*Eg1 : 0.001 : Eg1-0.001);
rangeMu2 = q * (fr*Eg2 : 0.001 : Eg2-0.001);
rangeMu3 = q * (fr*Eg3 : 0.001 : Eg3-0.001);

% Pre-allocations
I1 = zeros(1,length(rangeMu1));
I2 = zeros(1,length(rangeMu2));
I3 = zeros(1,length(rangeMu3));
delta = zeros(1, length(rangeMu1));
delta(:) = NaN; Im = delta; Vm = delta;
zz = 0;   % Counter for delta
tol = 0.99;   % Tollerence for allowed current mismatch

% Main body of the current matching routine
while tol ~= 0.89
% Begin by checking bottom cell current
for z=1:length(rangeMu3)

    mu3 = rangeMu3(z);
    % Bottom cell photocurrent and derivative
    specFluxC = @(E) 2*pi/(h^3*c^2) * E.^2 ./ (exp( ((E-mu3) / (k*Tc) ) -
1));
    I3(z) = IL3 - q*quadgk(specFluxC, q*Eg3, q*Eg2);
    specGrad = @(E) -2*pi/(h^3*c^2) * q/(4*k*Tc) * E.^2 .* (csch( (E-mu3)
/ (2*k*Tc) )).^2;
    gradI3 = quadgk(specGrad, q*Eg3, q*Eg2);

    % Only calculate the remaining stack while the bottom cell current is
    % positive; otherwise, end the loop
    if I3(z) > 0
        % For positive bottom cell current, check middle cell current
        for y=1:length(rangeMu2)

            mu2 = rangeMu2(y);
            disp('    Eg1       Eg2       Eg3'); disp([Eg1 Eg2 Eg3])
            disp('Matching middle and bottom cell photocurrents....')
            disp('    mu2       mu3'); disp([mu2 mu3]/q)
            disp('-----------------------------------------------------
-----------')
            disp(' ')

            % Middle cell photocurrent and derivative
            specFluxC = @(E) 2*pi/(h^3*c^2) * E.^2 ./ (exp( ((E-mu2) /
(k*Tc) ) - 1));
            I2(y) = IL2 - q*quadgk(specFluxC, q*Eg2, q*Eg1);
            specGrad = @(E) -2*pi/(h^3*c^2) * q/(4*k*Tc) * E.^2 .* (csch(
(E-mu2) / (2*k*Tc) )).^2;
            gradI2 = quadgk(specGrad, q*Eg2, q*Eg1);

            if I2(y) > 0
                % Calculate top cell photocurrent only if the bottom and
                % middle cell photocurrents are matched
                if min( [I2(y) I3(z)] ) / max( [I2(y) I3(z)] ) >= tol
                    for x=1:length(rangeMu1)
```

```
                        mu1 = rangeMu1(x);
                        V = (mu1 + mu2 + mu3)/q;
                        disp('    Eg1       Eg2       Eg3'); disp([Eg1 Eg2
Eg3])
                        disp('Matching top cell photocurrent to the
stack....')
                        disp('    mu1       mu2       mu3'); disp([mu1 mu2
mu3]/q)
                        disp('-----------------------------------------
-----------------------')
                        disp(' ')

                        % Top cell photocurrent and derivative
                        specFluxC = @(E) 2*pi/(h^3*c^2) * E.^2 ./ (exp(
((E-mu1) / (k*Tc) ) - 1));
                        I1(x) = IL1 - q*quadgk(specFluxC, q*Eg1, q*10);
                        specGrad = @(E) -2*pi/(h^3*c^2) * q/(4*k*Tc) *
E.^2 .* (csch( (E-mu1) / (2*k*Tc) )).^2;
                        gradI1 = quadgk(specGrad, q*Eg1, q*10);

                        if I1(x) > 0
                            % Calculate delta only if all photocurrents
are matched
                            if min( [I1(x) I2(y)] ) / max( [I1(x) I2(y)] )
>= tol
                                zz = zz + 1;
                                % Store variables
                                Im(zz) = max( [I1(x) I2(y) I3(z)] );
Vm(zz) = V;
                                % Lagrange-maximized function
                                delta(zz) = q*V + Im(zz) * ( 1/gradI1 +
1/gradI2 + 1/gradI3 );
                            end
                        else
                            % Return to middle cell calculation once top
                            % cell current becomes negative
                            x = length(rangeMu1);
                        end
                    end
                end
            else
                % Return to bottom cell calculation once middle cell
                % current becomes negative
                y = length(rangeMu2);
            end
        end
    else
        % End the loop once bottom cell current becomes negative
        z = length(rangeMu3);
    end
end

% Truncate values and check
delta = delta( ~isnan(delta) );
if isempty(delta)
    tol = tol - 0.01;   % Increase tolerance
```

```
    if tol == 0.89
        % Give up calculation at this data point
        delta = NaN; Im = NaN; Vm = NaN; Pm = NaN;
    else
        % Reset values and try again
        delta = zeros(1, length(rangeMu1));
        delta(:) = NaN; Im = delta; Vm = delta;
        zz = 0;   % Counter for delta
    end
else
    tol = 0.89;
    Im = Im( ~isnan(Im) );
    Vm = Vm( ~isnan(Vm) );
    Pm = Vm .* Im;
end
end

% Store values  -  [values @ minimum delta , values @ maximum efficiency]
Vmax = [Vm( abs(delta) == min(abs(delta)) ) Vm(Pm == max(Pm))];
if isempty(Vmax)
    Vmax = [NaN NaN]; Imax = [NaN NaN]; eff = [NaN NaN];
else
    Imax = [Im( abs(delta) == min(abs(delta)) ) Im(Pm == max(Pm))];
    eff = Vmax .* Imax / Ps;
end
```

Appendix VI

Detailed Balance Model for an Intermediate Band Solar Cell

(MATLAB Code)

The following code consists of three m-files (*db-ibsc.m, effFindIBSC.m,* and *currentMatchIBSC.m*) that together invoke the detailed balance model for the analysis of an intermediate band solar cell as discussed in Section 2.4. The standard inputs are solar and device temperatures, solar concentration factors, and the bandgaps separating the conduction band from the intermediate band and separating the intermediate band from the valence band. A range of solar concentrations and of both bandgaps may be entered. The routine loops through each value in these ranges allowing for the generation of efficiency contours as presented in Section 2.4. The routine is setup to allow for the analysis to use the blackbody, AM0, AM1.5G, or AM1.5D solar spectra. Upon running the routine, the detailed balance efficiency limits are saved in the *effVal* matrix for pertinent post-processing analysis.

The file *db-ibsc.m* is the master routine and calls upon *effFindIBSC.m* as part of the routine. User-entered inputs and machine storage of pertinent data occurs in *db-ibsc.m*. This routine also loops through each permutation of bandgaps and solar concentrations, each time passing the current permutation to *effFindIBSC.m.* The solar spectra are automatically chosen by *db-ibsc.m*

The *effFindIBSC.m* routine numerically solves the detailed balance model to determine the current due to the bulk response. This file then calls upon the *currentMatchIBSC.m* routine to find the current arising from the intermediate transitions. These currents are determined over an iterative voltage sweep until a maximum power is

found thus giving the detailed balance efficiency. The *currentMatchIBSC.m* algorithm iteratively determines the current arising from the intermediate transition subject to the constraint of current matching discussed in Section 2.4.

```
% db-ibsc.m
% Thus routine loops effFindIBSC.m through several solar concentrations
and
% finds maximum efficiency as a function of the two intermediate bandgaps

load spectrumFlux
q=1.6021765e-19; h=6.626069e-34; c=299792458; k=1.38065e-23;
sigma=5.6704e-8; f=2.1646e-5;

% Tunable paramters
Ts=6000; Tc=300;
rangeC = [1 10 100 1000 10000 1/f];
rangeEci = 1:0.01:2; rangeEiv = 0.50:0.01:0.95;

% Solar spectral flux
specFluxS = @(E) 2*pi/(h^3*c^2) * E.^2 ./ (exp(E/(k*Ts)) - 1);

% Preallocation for effiencies: Row-Eci, Col-Eiv, Dpt-Conc, 4th-Spectrum
effVal = zeros(length(rangeEci), length(rangeEiv), length(rangeC), 3);

amCount=0;
for w = 1:3;
    switch w
        case 1   % Blackbody
            spec=0;
        case 2   % AM0
            spec=1;
        case 3   % AM1.5G for one sun, AM1.5D for the rest
            if amCount == 0
                spec=2; amCount=1;
            else
                spec=3;
            end
    end

    for x = 1:length(rangeC)
        C = rangeC(x);
        for y = 1:length(rangeEci)
            Eci = rangeEci(y);
            for z = 1:length(rangeEiv)
                Eiv = rangeEiv(z);
                Eg = Eci + Eiv;

                effFindIBSC
                effVal(y,z,x,w) = eff;   % Row-Eci, Col-Eiv, Dpt-C, 4th-
Spec
            end
        end

        % Interim save
        save effFile effVal
    end
end
```

```
% effFindIBSC.m
% This routine steps currentMatchIBSC.m through several voltages until the
code
% converges onto a maximum efficiency for the specified bandgaps.

% Fraction of the bulk bandgap ranging from 0.65 to 0.90 used to determine
% the initial voltage and chemical potentials
fr = .25 * ( 13/5 - log(C)/log(f) );
% Initial voltage and chemical potentials
V=fr*Eg; muIV=mean([V-Eci Eiv]); muCI=V-muIV;

% Bulk short-circuit current
switch spec
    case 0
        IcvL = q*C*f * quadgk(specFluxS,q*Eg, q*22);
    case 1
        lamCV = h*c / (Eg*q) * 1e9;   % Wavelength (nm) corresponding to
        maxPtCV = find(lam0<=lamCV, 1, 'last');           % the enrgy gap
        IcvL = q*C * trapz(lam0(1:maxPtCV), AM0(1:maxPtCV));
    case 2
        lamCV = h*c / (Eg*q) * 1e9;   % Wavelength (nm) corresponding to
        maxPtCV = find(lam1p5<=lamCV, 1, 'last');         % the enrgy gap
        IcvL = q*C * trapz(lam1p5(1:maxPtCV), AM1p5G(1:maxPtCV));
    case 3
        lamCV = h*c / (Eg*q) * 1e9;   % Wavelength (nm) corresponding to
        maxPtCV = find(lam1p5<=lamCV, 1, 'last');         % the enrgy gap
        IcvL = q*C * trapz(lam1p5(1:maxPtCV), AM1p5D(1:maxPtCV));
end

stopSweep=0; eff=0; effOld=0; effCount=0; revDir=0;
while stopSweep == 0;
    effCount = effCount + 1;
    currentMatchIBSC
    if isnan(eff)
        return
    end

    % Determine total current and efficiency for voltage V
    specFluxC = @(E) 2*pi/(h^3*c^2) * E.^2 ./ (exp( (E - (q*V))/(k*Tc) ) -
1);
    Icv = IcvL - q * quadgk(specFluxC,q*Eg, q*10);
    Itotal = Icv + Ici;
    switch spec
        case 0
            eff = V * Itotal / (C*f*sigma*Ts^4);
        case 1
            eff = V * Itotal / (C*1366.1);
        case 2
            eff = V * Itotal / (C*1000.4);
        case 3
            eff = V * Itotal / (C*900.14);
    end

    if eff > effOld;
        if revDir == 0;   % Check to see which direction to sweep voltage
            Vold = V;
```

```
            V = V + 0.01;
        else
            Vold = V;
            V = V - 0.01;
        end
    elseif eff < effOld;
        if effCount ~= 2;
            eff = effOld;
            V = Vold;
            stopSweep = 1;
        else   % This runs only if a maximum is detected in the first run
            Vold = V;
            V = Vold - 0.01;
            revDir = 1;   % Reverse direction of the bias sweep
        end
    else
        stopSweep = 1;
    end

    disp('Solar Concentration:'); disp(C)
    disp('Voltage Step:'); disp(effCount)
    disp('    V         Eff.      Eci       Eiv       mu_ci     mu_iv')
    disp([V eff Eci Eiv muCI muIV])
    disp('    Ici'); disp(Ici)
    disp('    Iiv'); disp(Iiv)
    disp('    Icv'); disp(Icv)
    disp('    Itotal'); disp(Itotal)

    if stopSweep == 0;
        effOld = eff;
        disp('Finding maximum efficiency....')
    else
        disp('Converged to maximum efficiency!')
    end
    disp('------------------------------------------------------------
')
    disp(' ')
end
```

```
% currentMatchIBSC.m
% At a given bias and band spacing, this routine determines the
% intermediate band chemical potentials and cell photocurrent.

% Intermediate band short-circuit currents
switch spec
    case 0
        IciL = q*C*f * quadgk(specFluxS,q*Eci, q*Eg);
        IivL = q*C*f * quadgk(specFluxS,q*Eiv, q*Eci);
    case 1
        lamCI = h*c / (Eci*q) * 1e9;   % Wavelengths (nm) corresponding to
        lamIV = h*c / (Eiv*q) * 1e9;   % the energy gaps.
        maxPtCI = find(lam0<=lamCI, 1, 'last');
        maxPtIV = find(lam0<=lamIV, 1, 'last');
        IciL = q*C * trapz(lam0(maxPtCV:maxPtCI), AM0(maxPtCV:maxPtCI));
        IivL = q*C * trapz(lam0(maxPtCI:maxPtIV), AM0(maxPtCI:maxPtIV));
    case 2
        lamCI = h*c / (Eci*q) * 1e9;   % Wavelengths (nm) corresponding to
        lamIV = h*c / (Eiv*q) * 1e9;   % the energy gaps.
        maxPtCI = find(lam1p5<=lamCI, 1, 'last');
        maxPtIV = find(lam1p5<=lamIV, 1, 'last');
        IciL = q*C * trapz(lam1p5(maxPtCV:maxPtCI),
AM1p5G(maxPtCV:maxPtCI));
        IivL = q*C * trapz(lam1p5(maxPtCI:maxPtIV),
AM1p5G(maxPtCI:maxPtIV));
    case 3
        lamCI = h*c / (Eci*q) * 1e9;   % Wavelengths (nm) corresponding to
        lamIV = h*c / (Eiv*q) * 1e9;   % the energy gaps.
        maxPtCI = find(lam1p5<=lamCI, 1, 'last');
        maxPtIV = find(lam1p5<=lamIV, 1, 'last');
        IciL = q*C * trapz(lam1p5(maxPtCV:maxPtCI),
AM1p5D(maxPtCV:maxPtCI));
        IivL = q*C * trapz(lam1p5(maxPtCI:maxPtIV),
AM1p5D(maxPtCI:maxPtIV));
end

% Initial solution for intermediate band photocurrents
specFluxC = @(E) 2*pi/(h^3*c^2) * E.^2 ./ (exp( (E - (q*muCI))/(k*Tc) ) -
1);
Ici = IciL - q*quadgk(specFluxC, q*Eci, q*Eg);
specFluxC = @(E) 2*pi/(h^3*c^2) * E.^2 ./ (exp( (E - (q*muIV))/(k*Tc) ) -
1);
Iiv = IivL - q*quadgk(specFluxC, q*Eiv, q*Eci);

% Current matching algorithm for the intermediate band photocurrents
stp = 0.1;   % Amount by which to increase the chemical potential
if min([Eci-muCI Eiv-muIV]) <= 0.01
    stp = stp/100;
elseif min([Eci-muCI Eiv-muIV]) <= 0.1
    stp = stp/10;
end
match=0; count=0; muCIolder=100;
while match==0;
    count=count+1;
    disp('Solar Concentration:'); disp(C)
    disp('Voltage Step:'); disp(effCount)
```

```
    disp('Iteration:'); disp(count)

    delta = Ici - Iiv;
    % WARNING!!!
    % The delta parameter assumes both currents to be positive values.
    % An interlock is implemented at the end of the loop; however, it is
    % not 100% failsafe (especially if a negative current is realized
    % during the first itteration).

    % This is an interlock to make sure the chemical potentials do not
    % exceed their respective energy gaps
    if max([(Eci <= muCI) (Eiv <= muIV)]) == 1
        muCI = muCIold; muIV = muIVold;
        stp = stp/10;
    elseif min([Eci-muCI Eiv-muIV]) <= 0.01
        stp = 0.001;
        muCIold = muCI; muIVold = muIV;
        Iciold= Ici; Iivold = Iiv;
    elseif min([Eci-muCI Eiv-muIV]) <= 0.1
        if stp ~= 0.001
            stp = 0.01;
        end
        muCIold = muCI; muIVold = muIV;
        Iciold= Ici; Iivold = Iiv;
    else
        % Store current values for when they must be reverted to
        muCIold = muCI; muIVold = muIV;
        Iciold= Ici; Iivold = Iiv;
    end

    % Determine whether to step the chemical potentials up or down
    if delta > 0;
        if muCI + stp >= Eci;
            stp = stp/10;
        end
        disp('Increasing conduction-to-intermediate band dark
current....')
        muCI =  muCI + stp;
        muIV = V - muCI;
    elseif delta < 0;
        if muIV + stp >= Eiv;
            stp = stp/10;
        end
        disp('Increasing intermediate-to-valence band dark current....')
        muIV =  muIV + stp;
        muCI = V - muIV;
    else
        disp('Converged to a solution!')
        match = 1;
    end

    if match == 0;
        % Check to see if there is a possible match or if a decrease in
        % step is necessary
        if muCI == muCIolder;
            if stp == 0.001;
```

```
                disp('Converged to a solution!')
                match = 1;
                % Reset to previous chemical potentials; note there is no
                % new recalculation of the photocurrents
                muCI = muCIold; muIV = muIVold;
                % Determine and use whichever data has less error
                if abs(Iciold - Iivold) > abs(Iciolder - Iivolder);
                    Ici = Iciolder; Iiv = Iivolder;
                    muCI = muCIolder; muIV = muIVolder;
                end
            else
                stp = stp/10;
            end
        end
    end

    % Recalculate the intermediate band photocurrents
    if match == 0;
        specFluxC = @(E) 2*pi/(h^3*c^2) * E.^2 ./ (exp( (E -
(q*muCI))/(k*Tc) ) - 1);
        Ici = IciL - q*quadgk(specFluxC, q*Eci, q*Eg);
        specFluxC = @(E) 2*pi/(h^3*c^2) * E.^2 ./ (exp( (E -
(q*muIV))/(k*Tc) ) - 1);
        Iiv = IivL - q*quadgk(specFluxC, q*Eiv, q*Eci);

        if min(sign([Ici Iiv])) < 1;
            % Revert to previous values if either photocurrent becomes
            % negative
            muCI = muCIold; muIV = muIVold;
            Ici = Iciold; Iiv = Iivold;
            stp = stp/10;
        else
            % Store old values as older values for comparison above
            muCIolder = muCIold; muIVolder = muIVold;
            Iciolder = Iciold; Iivolder = Iivold;
        end
    end

    disp(' ')
    disp('    V         Eff.      Eci       Eiv       mu_ci     mu_iv')
    disp([V eff Eci Eiv muCI muIV])
    disp('    Ici'); disp(Ici)
    disp('    Iiv'); disp(Iiv)
    disp('-----------------------------------------------------------------')
    disp(' ')

    if stp < 0.001
        stp = 0.001;
    end

    if count == 1000
        disp('Unable to converge!')
        eff = NaN;
        return
    end
end
```

Appendix VII

Single-Junction Solar Cell Device Model (ATLAS Code)

The following code consists of three ATLAS decks (*pv00.in, pv01.in, and sr00.in*) that individually simulate the single-junction solar cell as described in Sections 3.16 and 3.17. The *pv00.in* and *pv01.in* decks both simulate the illuminated current-voltage response of the solar cell. In the first file, the device structure is defined using an auto-meshing technique that is simpler to define and more accurate in the numerical analysis. The latter defines the device structure by manual meshing. This is a more complicated technique but, if properly applied, leads to a more efficiently obtained solution. The *sr00.in* deck uses the same auto-meshing technique as in *pv00.in* and solves for the spectral response of the device.

```
# pv00.in

go atlas

mesh auto

x.mesh loc=-200 spac=10
x.mesh loc=-50  spac=10
x.mesh loc=-45  spac=5
x.mesh loc=-10  spac=5
x.mesh loc=-9   spac=1
x.mesh loc=0    spac=1
x.mesh loc=9    spac=1
x.mesh loc=10   spac=5
x.mesh loc=45   spac=5
x.mesh loc=50   spac=10
x.mesh loc=200  spac=10

# Regions
region                top    thick=0.010 ny=1  material=Vacuum
region name=Contact   bottom thick=0.100 ny=5  material=GaAs
      acceptor=1e19
region name=Window    bottom thick=0.050 ny=6  material=InGaP
      acceptor=2e18 x.comp=0.52
region name=Emitter   bottom thick=0.500 ny=6  material=GaAs
      acceptor=1e18
region name=Intrinsic bottom thick=0.100 ny=5  material=GaAs  acceptor=0
      donor=0
region name=Base      bottom thick=2.000 ny=20 material=GaAs  donor=1e17
region name=BSF       bottom thick=0.050 ny=6  material=InGaP donor=1e18
      x.comp=0.52
region name=Sub       bottom thick=0.100 ny=4  material=GaAs  donor=1e18
# Contact Etch
region x.min=-200 x.max=-4   y.min=0 y.max=0.1 material=Vacuum
region x.min=4    x.max=200  y.min=0 y.max=0.1 material=Vacuum

# Electrodes
electrode name=Anode   x.min=-4 x.max=4 y.min=-0.010 y.max=0
electrode name=Cathode bottom

# Interfaces
# Vacuum-Window
interface x.min=-200 x.max=-4  y.min=0.080 y.max=0.120 s.n=1e8
interface x.min=4    x.max=200 y.min=0.080 y.max=0.120 s.n=1e8
# Back Window
interface x.min=-200 x.max=200 y.min=0.120 y.max=0.180 s.s thermionic
      tunnel
# Back BSF
interface x.min=-200 x.max=200 y.min=2.780 y.max=2.820 s.s thermionic
      tunnel

# Material Properties
material taup=50e-9 taun=50e-9
# GaAs
material material=GaAs copt=7.2e-10
# InGaP
material material=InGaP affinity=4.07 index.file=../InGaP.opt
```

```
material name=Window    mun=600 mup=40
material name=BSF       mun=800 mup=40
# Contact
material material=Conductor imag.index=1000

# Models & Outputs
model fermi SRH
model material=GaAs conmob optr print
output val.band con.band opt.int u.aug u.srh u.rad

# Define AM0 spectrum
beam num=1 x.origin=0 y.origin=-0.1 angle=90 power.file=../AM0.spec
      wavel.start=0.200 wavel.end=0.930 wavel.num=146

# Initial solution
solve init
solve prev
log outf=pv00.log

save outf=pv00_0.str

# Zero bias w/ photogeneration
solve b1=1

save outf=pv01_1.str

# Light IV sweep
solve b1=1 vanode=0.050 vstep=0.050 vfinal=0.800 name=anode
solve b1=1 vanode=0.805 vstep=0.005 vfinal=1.000 name=anode
solve b1=1 vanode=1.010 vstep=0.010 vfinal=1.100 name=anode

# Plot IV curve
tonyplot pv00.log -set ../iv.set

# Extracts
extract name="Voc" x.val from curve(v."anode", i."cathode") where y.val=0
extract name="Isc" y.val from curve(v."anode", i."cathode"*25*1e4*1000)
      where x.val=0
extract name="Pm" max(v."anode"*i."cathode"*25*1e4*1000)
```

```
# pv01.in

go atlas

mesh space.mult=1

x.mesh loc=-200 spac=20
x.mesh loc=-50  spac=10
x.mesh loc=-45  spac=5
x.mesh loc=-10  spac=5
x.mesh loc=-9   spac=1
x.mesh loc=0    spac=1
x.mesh loc=9    spac=1
x.mesh loc=10   spac=5
x.mesh loc=45   spac=5
x.mesh loc=50   spac=10
x.mesh loc=200  spac=20

# Anode
y.mesh loc=-0.01 spac=0.005
# Contact
y.mesh loc=0.000 spac=0.005
y.mesh loc=0.005 spac=0.005
y.mesh loc=0.010 spac=0.010
# Window
y.mesh loc=0.050 spac=0.010
y.mesh loc=0.060 spac=0.020
# Emitter
y.mesh loc=0.560 spac=0.020
# Intrinsic Top
y.mesh loc=0.565 spac=0.005
y.mesh loc=0.575 spac=0.002

# Well Region
y.mesh loc=0.645 spac=0.002

# Intrinsic Bottom
y.mesh loc=0.660 spac=0.005
# Base
y.mesh loc=0.680 spac=0.010
y.mesh loc=0.720 spac=0.020
y.mesh loc=1.000 spac=0.200
y.mesh loc=2.600 spac=0.020
y.mesh loc=2.640 spac=0.020
y.mesh loc=2.660 spac=0.010
# BSF
y.mesh loc=2.710 spac=0.010
# Substrate
y.mesh loc=2.810 spac=0.020

# Bulk Regions
region                x.min=-200 x.max=-4  y.min=-0.01 y.max=0.010
      material=Vacuum
region                x.min=4    x.max=200 y.min=-0.01 y.max=0.010
      material=Vacuum
region name=Contact   x.min=-4   x.max=4   y.min=0.000 y.max=0.010
      material=GaAs  acceptor=1e19
```

```
region name=Window    x.min=-200 x.max=200 y.min=0.010 y.max=0.060
      material=InGaP acceptor=2e18 x.comp=0.52
region name=Emitter   x.min=-200 x.max=200 y.min=0.060 y.max=0.560
      material=GaAs  acceptor=1e18
region name=Intrinsic x.min=-200 x.max=200 y.min=0.560 y.max=0.660
      material=GaAs  acceptor=0    donor=0
region name=Base      x.min=-200 x.max=200 y.min=0.660 y.max=2.660
      material=GaAs  donor=1e17
region name=BSF       x.min=-200 x.max=200 y.min=2.660 y.max=2.710
      material=InGaP donor=1e18    x.comp=0.52
region name=Sub       x.min=-200 x.max=200 y.min=2.710 y.max=2.810
      material=GaAs  donor=1e18

# Electrodes
electrode name=Anode   x.min=-4 x.max=4 y.min=-0.010 y.max=0.000
electrode name=Cathode bottom

# Interfaces
# Vacuum-Window
interface x.min=-200 x.max=-4  y.min=0.008 y.max=0.012 s.n=1e8
interface x.min=4    x.max=200 y.min=0.008 y.max=0.012 s.n=1e8
# Back Window
interface x.min=-200 x.max=200 y.min=0.058 y.max=0.062 s.s thermionic
      tunnel
# Back BSF
interface x.min=-200 x.max=200 y.min=2.708 y.max=2.712 s.s thermionic
      tunnel

# Material Properties
material taup=50e-9 taun=50e-9
# GaAs
material material=GaAs copt=7.2e-10
# InGaP
material material=InGaP affinity=4.07 index.file=../InGaP.opt
material name=Window    mun=600 mup=40
material name=BSF       mun=800 mup=40
# Contact
material material=Conductor imag.index=1000

# Models & Outputs
model fermi SRH
model material=GaAs conmob optr print
output val.band con.band opt.int u.aug u.srh u.rad

# Define AM0 spectrum
beam num=1 x.origin=0 y.origin=-0.1 angle=90 power.file=../AM0.spec
      wavel.start=0.200 wavel.end=4.000 wavel.num=760

# Initial solution
solve init
solve prev
log outf=pvXX.log

#save outf=pv01_0.str

# Zero bias w/ photogeneration
solve b1=1
```

```
#save outf=pv01_1.str

# Light IV sweep
solve b1=1 vanode=0.050 vstep=0.050 vfinal=0.800 name=anode
solve b1=1 vanode=0.805 vstep=0.005 vfinal=1.000 name=anode
solve b1=1 vanode=1.010 vstep=0.010 vfinal=1.100 name=anode

# Plot IV curve
tonyplot pvXX.log -set ../iv.set

# Extracts
extract name="Voc" x.val from curve(v."anode", i."cathode") where y.val=0
extract name="Isc" y.val from curve(v."anode", i."cathode"*25*1e4*1000)
      where x.val=0
extract name="Pm" max(v."anode"*i."cathode"*25*1e4*1000)
```

```
# sr00.in

go atlas

mesh auto

x.mesh loc=-200 spac=10
x.mesh loc=-50  spac=10
x.mesh loc=-45  spac=5
x.mesh loc=-10  spac=5
x.mesh loc=-9   spac=1
x.mesh loc=0    spac=1
x.mesh loc=9    spac=1
x.mesh loc=10   spac=5
x.mesh loc=45   spac=5
x.mesh loc=50   spac=10
x.mesh loc=200  spac=10

# Regions
region                top    thick=0.010 ny=1  material=Vacuum
region name=Contact   bottom thick=0.100 ny=5  material=GaAs
      acceptor=1e19
region name=Window    bottom thick=0.050 ny=6  material=InGaP
      acceptor=2e18 x.comp=0.52
region name=Emitter   bottom thick=0.500 ny=6  material=GaAs
      acceptor=1e18
region name=Intrinsic bottom thick=0.100 ny=5  material=GaAs  acceptor=0
      donor=0
region name=Base      bottom thick=2.000 ny=20 material=GaAs  donor=1e17
region name=BSF       bottom thick=0.050 ny=6  material=InGaP donor=1e18
      x.comp=0.52
region name=Sub       bottom thick=0.100 ny=4  material=GaAs  donor=1e18
# Contact Etch
region x.min=-200 x.max=-4   y.min=0 y.max=0.1 material=Vacuum
region x.min=4    x.max=200  y.min=0 y.max=0.1 material=Vacuum

# Electrodes
electrode name=Anode   x.min=-4 x.max=4 y.min=-0.010 y.max=0
electrode name=Cathode bottom

# Interfaces
# Vacuum-Window
interface x.min=-200 x.max=-4  y.min=0.080 y.max=0.120 s.n=1e8
interface x.min=4    x.max=200 y.min=0.080 y.max=0.120 s.n=1e8
# Back Window
interface x.min=-200 x.max=200 y.min=0.120 y.max=0.180 s.s thermionic
# Back BSF
interface x.min=-200 x.max=200 y.min=2.780 y.max=2.820 s.s thermionic

# Material Properties
material taup=50e-9 taun=50e-9
# GaAs
material material=GaAs copt=7.2e-10
# InGaP
material material=InGaP affinity=4.07 index.file=../InGaP.opt
material name=Window    mun=600 mup=40
material name=BSF       mun=800 mup=40
```

```
# Contact
material material=Conductor imag.index=1000

# Models & Outputs
model fermi SRH
model material=GaAs conmob optr
output val.band con.band opt.int u.aug u.srh u.rad

# Initial solution
solve init
solve prev
log outf=sr00.log

# Monochromatic Beam
beam num=2 x.origin=0 y.origin=-1 angle=90

# Solve spectral response
solve b2=.1 lambda=1.000
solve b2=.1 lambda=0.975
solve b2=.1 lambda=0.950
solve b2=.1 lambda=0.925
solve b2=.1 lambda=0.900
solve b2=.1 lambda=0.875
solve b2=.1 lambda=0.850
solve b2=.1 lambda=0.825
solve b2=.1 lambda=0.800
solve b2=.1 lambda=0.775
solve b2=.1 lambda=0.750
solve b2=.1 lambda=0.725
solve b2=.1 lambda=0.700
solve b2=.1 lambda=0.675
solve b2=.1 lambda=0.650
solve b2=.1 lambda=0.625
solve b2=.1 lambda=0.600
solve b2=.1 lambda=0.575
solve b2=.1 lambda=0.550
solve b2=.1 lambda=0.525
solve b2=.1 lambda=0.500
solve b2=.1 lambda=0.475
solve b2=.1 lambda=0.450
solve b2=.1 lambda=0.425
solve b2=.1 lambda=0.400
solve b2=.1 lambda=0.375
solve b2=.1 lambda=0.350
solve b2=.1 lambda=0.325
solve b2=.1 lambda=0.300
solve b2=.1 lambda=0.275
solve b2=.1 lambda=0.250
solve b2=.1 lambda=0.225
solve b2=.1 lambda=0.200

tonyplot sr00.log -set ../qe.set
```

Appendix VIII

Dual-Junction Solar Cell Device Model (ATLAS Code)

The following code consists of two ATLAS decks (*djIV.in and djSR.in*) that individually simulate the dual-junction solar cell as described in Section 3.18. The *djIV.in* deck simulates the illuminated current-voltage response of the solar cell while the *djSR.in* deck solves for the spectral response of the device.

```
# djIV.in

go atlas

mesh auto

x.mesh loc=-200 spac=20
x.mesh loc=-40  spac=20
x.mesh loc=-30  spac=10
x.mesh loc=-10  spac=5
x.mesh loc=-9   spac=1
x.mesh loc=0    spac=1
x.mesh loc=9    spac=1
x.mesh loc=10   spac=5
x.mesh loc=30   spac=10
x.mesh loc=40   spac=20
x.mesh loc=200  spac=20

# Regions
region                top    thick=0.010 ny=1  material=Vacuum
# Top Cell
region name=tContact   bottom thick=0.100 ny=3  material=GaAs
      acceptor=1e19
region name=tWindow    bottom thick=0.030 ny=3  material=AlAs
      acceptor=1e18
region name=tEmitter   bottom thick=0.100 ny=3  material=InGaP
      acceptor=1e18 x.comp=0.52
region name=tBase      bottom thick=2.000 ny=3  material=InGaP donor=1e17
      x.comp=0.52
region name=tBSF       bottom thick=0.100 ny=3  material=InGaP donor=1e18
      x.comp=0.52

# Tunnel
region name=td1        bottom thick=0.050 ny=4  material=InAs  donor=1e19
region name=td2        bottom thick=0.050 ny=4  material=InAs
      acceptor=1e19

# Middle Cell
region name=mWindow    bottom thick=0.050 ny=3  material=InGaP
      acceptor=2e18 x.comp=0.52
region name=mEmitter   bottom thick=0.500 ny=3  material=GaAs
      acceptor=1e18
region name=mIntrinsic bottom thick=0.100 ny=3  material=GaAs  acceptor=0
      donor=0
region name=mBase      bottom thick=2.000 ny=3  material=GaAs  donor=1e17
region name=mBSF       bottom thick=0.050 ny=3  material=InGaP donor=1e18
      x.comp=0.52
region name=mSub       bottom thick=0.100 ny=3  material=GaAs  donor=1e18

# Contact Etch
region x.min=-200 x.max=-4  y.min=0 y.max=0.1 material=Vacuum
region x.min=4    x.max=200 y.min=0 y.max=0.1 material=Vacuum

# Electrodes
electrode name=Anode   x.min=-4 x.max=4 y.min=-0.010 y.max=0
electrode name=Cathode bottom
```

```
# Interfaces
# Vacuum-Window
interface x.min=-200 x.max=-4  y.min=0.090 y.max=0.110 s.n=1e8
interface x.min=4    x.max=200 y.min=0.090 y.max=0.110 s.n=1e8

# Material Properties
material taup=50e-9 taun=50e-9
# GaAs
material material=GaAs copt=7.2e-10
# InGaP
material material=InGaP affinity=4.07 index.file=../InGaP.opt mun=800
      mup=40
# Contact
material material=Conductor imag.index=1000
# AlAs
material material=AlAs mun=150 mup=65
# Tunnel
material material=InAs index.file=../GaAs0ab.opt

# Models & Outputs
model fermi SRH
model material=GaAs conmob optr print
model material=InAs bbt.std
output val.band con.band opt.int u.aug u.srh u.rad

# Define AM0 spectrum
beam num=1 x.origin=0 y.origin=-0.1 angle=90 power.file=../AM0.spec
      wavel.start=0.200 wavel.end=2.000 wavel.num=360

# Initial solution
solve init
save outf=pv00a_0.str
log outf=pv00a.log

# Zero bias w/ photogeneration
solve b1=1

save outf=pv00_1.str

# Light IV sweep
solve b1=1 vanode=0.10 vstep=0.10 vfinal=2.6 name=anode
#solve b1=1 vanode=1.71 vstep=0.01 vfinal=1.9 name=anode
#solve b1=1 vanode=2.00 vstep=0.10 vfinal=2.6 name=anode

# Plot IV curve
tonyplot pv00a.log -set ../iv.set

# Extracts
extract name="Voc" x.val from curve(v."anode", i."cathode") where y.val=0
extract name="Isc" y.val from curve(v."anode", i."cathode"*25*1e4*1000)
      where x.val=0
extract name="Pm" max(v."anode"*i."cathode"*25*1e4*1000)
```

```
# djSR.in

go atlas

mesh auto

x.mesh loc=-200 spac=20
x.mesh loc=-40  spac=20
x.mesh loc=-30  spac=10
x.mesh loc=-10  spac=10
x.mesh loc=-9   spac=1
x.mesh loc=0    spac=1
x.mesh loc=9    spac=1
x.mesh loc=10   spac=10
x.mesh loc=30   spac=10
x.mesh loc=40   spac=20
x.mesh loc=200  spac=20

# Regions
region                top     thick=0.010 ny=1 material=Vacuum

# InGaP Cell
region name=tContact   bottom thick=0.100 ny=3 material=GaAs
      acceptor=1e19
region name=tWindow    bottom thick=0.030 ny=3 material=AlAs
      acceptor=2e18
region name=tEmmitter  bottom thick=0.100 ny=3 material=InGaP
      acceptor=1e18 x.comp=0.52
region name=tBase      bottom thick=1.000 ny=3 material=InGaP donor=1e17
      x.comp=0.52
region name=tBSF       bottom thick=0.100 ny=3 material=InGaP donor=2e18
      x.comp=0.52
#
region name=tSpace     bottom thick=0.050 ny=1 material=Air
# GaAs Cell
region name=mWindow    bottom thick=0.050 ny=3 material=InGaP
      acceptor=2e18 x.comp=0.52
region name=mEmitter   bottom thick=0.500 ny=3 material=GaAs
      acceptor=1e18
region name=mIntrinsic bottom thick=0.100 ny=3 material=GaAs  acceptor=0
      donor=0
region name=mBase      bottom thick=2.000 ny=3 material=GaAs  donor=1e17
region name=mBSF       bottom thick=0.050 ny=3 material=InGaP donor=1e18
      x.comp=0.52
region name=mSub       bottom thick=0.150 ny=3 material=GaAs  donor=1e18
# Contact Etch
region x.min=-200 x.max=-4   y.min=0 y.max=0.1 material=Vacuum
region x.min=4    x.max=200  y.min=0 y.max=0.1 material=Vacuum

# Electrodes
electrode name=tAnode   x.min=-4   x.max=4   y.min=-0.010 y.max=0
electrode name=tCathode x.min=-200 x.max=200 y.min=1.330  y.max=1.330
electrode name=mAnode   x.min=-200 x.max=200 y.min=1.380  y.max=1.380
electrode name=mCathode bottom

contact name=tCathode common=mCathode
```

```
# Interfaces
# Vacuum-Window
interface x.min=-200 x.max=-4  y.min=0.090 y.max=0.110 s.n=1e8
interface x.min=4    x.max=200 y.min=0.090 y.max=0.110 s.n=1e8

# Material Properties
material taup=50e-9 taun=50e-9
# GaAs
material material=GaAs copt=7.2e-10
# InGaP
material material=InGaP  affinity=4.07 index.file=../InGaP.opt mup=40
material name=tEmitter   mun=800
material name=tBase      mun=1000
material name=tBSF       mun=600
material name=mWindow    mun=600
material name=mBSF       mun=800
# AlAs
material material=AlAs   mun=500  mup=100
# Top Contact
material material=Conductor imag.index=1000
# Spacing
material material=Air index.file=../GaAs.opt

# Models & Outputs
model fermi SRH
model material=GaAs conmob optr print
output val.band con.band opt.int u.aug u.srh u.rad

# Initial solution
solve init
solve prev

log  outf=srmB1.log

# Monochromatic Beam
beam num=2 x.origin=0 y.origin=-1 angle=90

# Solve spectral response
solve b2=.1 lambda=1.000
solve b2=.1 lambda=0.975
solve b2=.1 lambda=0.950
solve b2=.1 lambda=0.925
solve b2=.1 lambda=0.900
solve b2=.1 lambda=0.875
solve b2=.1 lambda=0.850
solve b2=.1 lambda=0.825
solve b2=.1 lambda=0.800
#save outf=sr00_800.str

solve b2=.1 lambda=0.775
solve b2=.1 lambda=0.750
solve b2=.1 lambda=0.725
solve b2=.1 lambda=0.700
solve b2=.1 lambda=0.675
solve b2=.1 lambda=0.650
solve b2=.1 lambda=0.625
solve b2=.1 lambda=0.600
```

```
solve b2=.1 lambda=0.575
solve b2=.1 lambda=0.550
#save outf=sr00_550.str

solve b2=.1 lambda=0.525
solve b2=.1 lambda=0.500
solve b2=.1 lambda=0.475
solve b2=.1 lambda=0.450
solve b2=.1 lambda=0.425
solve b2=.1 lambda=0.400
solve b2=.1 lambda=0.375
solve b2=.1 lambda=0.350
solve b2=.1 lambda=0.325
solve b2=.1 lambda=0.300
solve b2=.1 lambda=0.275
solve b2=.1 lambda=0.250
solve b2=.1 lambda=0.225
solve b2=.1 lambda=0.200
```

Appendix IX

Nanostructured Solar Cell Device Model (ATLAS Code)

The following code consists of two ATLAS decks (*pvQW.in* and *pvEL.in*) that individually simulate the quantum mechanical effects that arise due to the inclusion of nanostructures in a single-junction solar cell as described in Section 3.19. The *pvQW.in* deck is used to explicitly analyze the quantum confined regions and to specifically determine the properties of the eigenstates located therein. The *pvEL.in* deck simulates the electroluminescence that occurs due to the nanostructured regions.

```
# pvQW.in

go atlas

mesh space.mult=1.0 auto

x.mesh loc=-2.00 spac=0.50
x.mesh loc=2.00 spac=0.50

region num=1  material=GaAs thick=1.500 sy=0.150 bottom acceptor=1e18
region num=2  material=GaAs thick=0.015 sy=0.005 bottom
region num=3  material=InAs thick=0.006 sy=0.001 bottom
region num=4  material=GaAs thick=0.010 sy=0.005 bottom
region num=5  material=InAs thick=0.006 sy=0.001 bottom
region num=6  material=GaAs thick=0.010 sy=0.005 bottom
region num=7  material=InAs thick=0.006 sy=0.001 bottom
region num=8  material=GaAs thick=0.010 sy=0.005 bottom
region num=9  material=InAs thick=0.006 sy=0.001 bottom
region num=10 material=GaAs thick=0.010 sy=0.005 bottom
region num=11 material=InAs thick=0.006 sy=0.001 bottom
region num=12 material=GaAs thick=0.015 sy=0.005 bottom
region num=13 material=GaAs thick=1.500 sy=0.150 bottom donor=1e17

# Electrodes
electrode name=anode   top
electrode name=cathode bottom

# Material Properties
material taun=1e-6 taup=1e-6
# GaAs
material material=GaAs copt=7.2e-10
# InAs
material material=InAs index.file=../InAs.opt copt=1.1e-10

# Models & Outputs
models fermi srh optr
models material=GaAs conmob
models material=InAs li qwell well.nx=9 well.ny=100 well.cnbs=1
      well.vnbs=5
output val.band con.band opt.int u.aug u.srh u.rad

# Define AM0 spectrum
beam num=1 x.origin=0 y.origin=-1 angle=90 power.file=../AM0.spec
      wavel.start=0.200 wavel.end=4.000 wavel.num=76

# Initial solution, save equilibrium structure
solve init
solve prev
save outf=pvQW_0.str
tonyplot

# Zero bias structure w/ photogeneration
log outf=pvQW.log
solve b1=1
save outf=pvQW_1.str
```

```
# pvEL.in

go atlas

mesh space.mult=1

x.mesh loc=-200 spac=20
x.mesh loc=-50  spac=10
x.mesh loc=-45  spac=5
x.mesh loc=-10  spac=5
x.mesh loc=-9   spac=1
x.mesh loc=0    spac=1
x.mesh loc=9    spac=1
x.mesh loc=10   spac=5
x.mesh loc=45   spac=5
x.mesh loc=50   spac=10
x.mesh loc=200  spac=20

# Anode
y.mesh loc=-0.01 spac=0.005
# Contact
y.mesh loc=0.000 spac=0.005
y.mesh loc=0.005 spac=0.005
y.mesh loc=0.010 spac=0.010
# Window
y.mesh loc=0.050 spac=0.010
y.mesh loc=0.060 spac=0.020
# Emitter
y.mesh loc=0.560 spac=0.020
# Intrinsic Top
y.mesh loc=0.565 spac=0.005
y.mesh loc=0.575 spac=0.002

# Well Region
y.mesh loc=0.645 spac=0.002

# Intrinsic Bottom
y.mesh loc=0.660 spac=0.005
# Base
y.mesh loc=0.680 spac=0.010
y.mesh loc=0.720 spac=0.020
y.mesh loc=1.000 spac=0.200
y.mesh loc=2.600 spac=0.020
y.mesh loc=2.640 spac=0.020
y.mesh loc=2.660 spac=0.010
# BSF
y.mesh loc=2.710 spac=0.010
# Substrate
y.mesh loc=2.810 spac=0.020

# Bulk Regions
region                x.min=-200 x.max=-4  y.min=-0.01 y.max=0.010
      material=Vacuum
region                x.min=4    x.max=200 y.min=-0.01 y.max=0.010
      material=Vacuum
region name=Contact   x.min=-4   x.max=4   y.min=0.000 y.max=0.010
      material=GaAs  acceptor=1e19
```

```
region name=Window    x.min=-200 x.max=200 y.min=0.010 y.max=0.060
      material=InGaP acceptor=2e18 x.comp=0.52
region name=Emitter   x.min=-200 x.max=200 y.min=0.060 y.max=0.560
      material=GaAs  acceptor=1e18         LED

region name=Intrinsic1 x.min=-200 x.max=200 y.min=0.560 y.max=0.575
      material=GaAs  acceptor=0    donor=0 LED
region name=Intrinsic2 x.min=-200 x.max=200 y.min=0.645 y.max=0.660
      material=GaAs  acceptor=0    donor=0 LED

region name=Base      x.min=-200 x.max=200 y.min=0.660 y.max=2.660
      material=GaAs  donor=1e17            LED
region name=BSF       x.min=-200 x.max=200 y.min=2.660 y.max=2.710
      material=InGaP donor=1e18    x.comp=0.52
region name=Sub       x.min=-200 x.max=200 y.min=2.710 y.max=2.810
      material=GaAs  donor=1e18

# Well Regions
region name=Well1 x.min=-200 x.max=200 y.min=0.575 y.max=0.581
      material=InAs LED acceptor=0 donor=0
region name=Barr1 x.min=-200 x.max=200 y.min=0.581 y.max=0.591
      material=GaAs LED acceptor=0 donor=0
region name=Well2 x.min=-200 x.max=200 y.min=0.591 y.max=0.597
      material=InAs LED acceptor=0 donor=0
region name=Barr2 x.min=-200 x.max=200 y.min=0.597 y.max=0.607
      material=GaAs LED acceptor=0 donor=0
region name=Well3 x.min=-200 x.max=200 y.min=0.607 y.max=0.613
      material=InAs LED acceptor=0 donor=0
region name=Barr3 x.min=-200 x.max=200 y.min=0.613 y.max=0.623
      material=GaAs LED acceptor=0 donor=0
region name=Well4 x.min=-200 x.max=200 y.min=0.623 y.max=0.629
      material=InAs LED acceptor=0 donor=0
region name=Barr4 x.min=-200 x.max=200 y.min=0.629 y.max=0.639
      material=GaAs LED acceptor=0 donor=0
region name=Well5 x.min=-200 x.max=200 y.min=0.639 y.max=0.645
      material=InAs LED acceptor=0 donor=0

# Electrodes
electrode name=Anode   x.min=-4 x.max=4 y.min=-0.010 y.max=0.000
electrode name=Cathode bottom

# Interfaces
# Vacuum-Window
interface x.min=-200 x.max=-4  y.min=0.008 y.max=0.012 s.n=1e8
interface x.min=4    x.max=200 y.min=0.008 y.max=0.012 s.n=1e8
# Back Window
interface x.min=-200 x.max=200 y.min=0.058 y.max=0.062 s.s thermionic
      tunnel
# Back BSF
interface x.min=-200 x.max=200 y.min=2.708 y.max=2.712 s.s thermionic
      tunnel

# Material Properties
material taup=50e-9 taun=50e-9
# GaAs
material material=GaAs copt=7.2e-10
# InGaP
```

```
material material=InGaP affinity=4.07 index.file=../InGaP.opt
material name=Window    mun=600 mup=40
material name=BSF       mun=800 mup=40
# InAs
material material=InAs index.file=../InAs.opt copt=1.1e-10
# Contact
material material=Conductor imag.index=1000

# Models & Outputs
model fermi SRH
model material=GaAs conmob li spont print
model material=InAs li qwell well.nx=9 well.ny=100 well.cnbs=1 well.vnbs=5
      spont
output val.band con.band opt.int u.aug u.srh u.rad

# Initial solution
solve init
solve prev
log outf=pv05a.log

# IV sweep
solve vanode=0.010 vstep=0.020 vfinal=0.400 name=anode
save spectrum=spec05a.log lmin=0.5 lmax=4.0 nsamp=300

tonyplot spec05.log -overlay spec05a.log
```

References

[1] *Basic Research Needs for Solar Energy Utilization: Report on the Basic Energy Sciences Workshop of Solar Energy Utilization, April 18-21, 2005*, Office of Science, US Dept. of Energy, 2005.

[2] *Green Paper: Towards a European Strategy for the Security of Energy Supply,* European Commission, 2001.

[3] *Advanced Energy Initiative,* White House National Economic Council, February 2006.

[4] S.M. Hubbard *et al.*, "Effect of Strain Compensation on Quantum Dot Enhanced GaAs Solar Cells," *Appl. Phys. Lett.,* vol. 92, pp. 123512-1 – 123512-3, 2008.

[5] A. Martí, L. Cuadra, and A. Luque, "Quantum Dot Intermediate Band Solar Cell," in *Conf. Rec. 28th IEEE Photovoltaics Spec. Conf.,* Anchorage, AK, 2000, pp. 940-943.

[6] R. R. King *et al.*, "40% Efficient Metamorphic GaInP/GaInAs/Ge Multijunction Solar Cells," *Appl. Phys. Lett.,* vol. 90, pp. 183516-1–183516-3, 2007.

[7] M.A. Green *et al.*, "Solar Cell Efficiency Tables (Version 29)," *Prog. Photovoltaics Res. Appl.,* vol. 15, pp. 35-40, 2007.

[8] M.A. Green, *Third Generation Photovoltaics: Advanced Solar Energy Conversion*, Springer-Verlag, 2006.

[9] C.D. Cress, *Effects of Ionizing Radiation on Nanomaterials and III-V Semiconductor Devices*, PhD Dissertation, Rochester Institute of Technology, New York, 2008.

[10] S.M. Sze and K.K. Ng, *Physics of Semiconductor Devices*, 3rd Ed., John Wiley & Sons, Hoboken, NJ, 2007.

[11] A.L Fahrenbruch and R.H. Bube, *Fundamentals of Solar Cells: Photovoltaic Solar Energy Conversion,* Academic Press, New York, NY 1983.

[12] D. Griffiths, *Introduction to Quantum Mechanics*, 2nd Ed., Pearson Prentice Hall, Upper Saddle River, NJ, 2005.

[13] C. Kittel, *Introduction to Solid State Physics*, 8th Ed., John Wiley & Sons, 2005.

[14] L.D. Landau and E.M Lifshitz*, Statistical Physics*, Addison-Wesley Publishing Co., Reading, MA, 1958.

[15] W. Shockley, "The Theory of p-n Junctions in Semiconductors and p-n Junction Transistors," *Bell Sys. Tech. J.,* vol. 28, pp. 435-489, 1949.

[16] Renewable Resource Data Center, National Renewable Energy Laboratory, (2008, Oct.), "Solar Spectra" [online], Available: http://rredc.nrel.gov/solar/spectra/.

[17] L. Esaki and R. Tsu, "Superlattice and Negative Differential Conductivity in Semiconductors," *IBM J. Res. Develop.,* vol. 14, pp. 61-65, 1970.

[18] W. Shockley and H.J. Queisser, "Detailed Balance Limit of Efficiency of p-n- Junction Solar Cells," *J. Appl. Phys.,* vol. 32, pp. 510-519, 1961.

[19] M. Plank, "Ueber das Gesetz der Energieverteilung im Normalspectrum," *Annalen der Physik*, vol. 309, pp. 553-563, 1901.

[20] C.T. Sah, R.N. Noyce, and W. Shockley, "Carrier Generation and Recombination in p-n Junctions and p-n Junction Characteristics," *Proc. IRE*, vol. 45, pp. 1228-1243, 1957.

[21] W. Shockley, "Electrons, Holes, and Traps," *Proc. IRE*, vol. 46, pp. 973-990, 1958.

[22] P. Würfel, "The Chemical Potential of Radiation," *J. Phys. C,* vol. 15, pp. 3967-3985, 1982.

[23] A. de Vos and H. Pauwels, "On the Thermodynamic Limit of Photovoltaic Energy Conversion," *Appl. Phys,* vol. 25, pp. 119-125, 1981.

[24] W. Ruppel and P. Würfel, "Upper Limit of the Conversion of Solar Energy," *IEEE Trans. Elec. Devices,* vol. ED-27, pp. 877-882, 1980.

[25] J.E. Parrott, "Self Consistent Detailed Balance Treatment of the Solar Cell," *IEE Proc.,* vol. 133, pp. 314-318, 1986.

[26] L.F. Shampine, "Vectorized Adaptive Quadrature in Matlab," *J. Computational Appl. Math.,* vol. 211, pp. 131-140, 2008.

[27] R.P. Raffaelle *et al.,* "Multi-Junction Solar Cell Spectra Tuning with Quantum Dots," in *Conf. Rec. 2006 IEEE 4th World Conf. Photovoltaic Energy Conv.*, Waikoloa, HI, 2006, pp.162-166.

[28] A. Luque and A. Martí, "Increasing the Efficiency of Ideal Solar Cells by Photon Induced Transitions at Intermediate Levels," *Phys. Rev. Lett.*, vol. 78, pp. 5014-5017, 1997.

[29] M. Wolf, "Limitations and Possibilities for Improvement of Photovoltaic Solar Energy Converters," *Proc. IRE*, vol. 48, pp. 1246-1263, 1960.

[30] *ATLAS User's Manual: Device Simulation Software*, 06/11/08 Ed., Silvaco Data Systems, Inc., Santa Clara, CA, 2008.
[31] J.S. Blakemore, "Approximations for Fermi-Dirac Integrals, Especially the Function $F_{1/2}(\eta)$ Used to Describe Electron Density in a Semiconductor," *Sol. State Elec.*, vol. 25, pp. 1067-1076, 1982.
[32] S.A. Wong, S.P. McAlister, and Z.M. Li, "A Comparison of Some Approximations for the Fermi-Dirac Integral of Order 1/2," *Sol. State Elec.*, vol. 37, pp. 61-64, 1994.
[33] W. Shockley and W.T. Read, "Statistics of the Recombination of Holes and Electrons," *Phys. Rev.,* vol. 87, pp. 835-842, 1952.
[34] R.N. Hall, "Electron-Hole Recombination in Germanium," *Phys. Rev.,* vol. 87, p. 387, 1952.
[35] C.T. Sah, R.N. Noyce, and W. Shockley, "Carrier Generation and Recombination in p-n Junctions and p-n Junction Characteristics," *Proc. IRE*, vol. 45, pp. 1228-1243, 1957.
[36] J. Piprek, *Semiconductor Optoelectronic Devices: Introduction to Physics and Simulation*, Elsevier Science, USA, 2003.
[37] R.F. Pierret, *Semiconductor Device Fundamentals*, Addison-Wesley Publishing Co., USA, 1996.
[38] A.S. Grove, *Physics and Technology of Semiconductor Device*, John Wiley & Sons, Hoboken, NJ, 1967.
[39] L.L. Chang, "The Conduction Properties of Ge-$GaAs_{1-x}P_x$ n-n Heterojunctions," *Sol. State Elec.,* vol. 8, pp. 721-728, 1965.
[40] H.A. Bethe, "Theory of the Boundary Layer of Crystal Rectifiers," *MIT Radiat. Lab. Rep.,* 43-12, 1942.
[41] C.M. Wu and E.S. Yang, "Carrier Transport Across Heterojunction Interfaces," *Sol. State Elec.*, vol. 22, pp. 241-248, 1979.
[42] K. Yang, J. East, and G. Haddad, "Numerical Modeling of Abrupt Heterojunctions Using a Thermionic-Field Emission Boundary Condition," *Sol. State Elec.*, vol. 36, pp. 321-330, 1993.
[43] E. Hecht, *Optics*, 4th Ed., Addison-Wesley Publishing Co., San Francisco, CA, 2002.
[44] O. Manasreh, *Semiconductor Heterojunctions and Nanostructures*, McGraw-Hill Co., USA, 2005.
[45] R.H. Yan, S.W. Corzine, L.A. Coldren, and I. Suemune, "Corrections to the Expression of Gain in GaAs," *IEEE J. Quantum Elec.,* vol. 26, pp. 213-216, 1990.
[46] A. Yariv and P. Yeh, *Photonics: Optical Electronics in Modern Communications*, 6th Ed., Oxford University Press, New York, 2007.
[47] Z.M. Li, K.M. Dzurko, A. Delâge, and S.P. McAlister, "A Self-Consistent Two-Dimensional Model of Quantum-Well Semiconductor Lasers: Optimization of a GRIN-SCH SQW Laser Structure," *IEEE J. Quantum Elec.,* vol. 28, pp.792-803, 1992.
[48] I. Vurgaftman, J.R. Meyer, and L.R. Ram-Mohan, "Band Parameters for III-V Compound Semiconductors and Their Alloys," *J. Appl. Phys.,* vol. 89, pp. 5815-5875, 2001.
[49] W. Nakwaski, "Effective Masses of Electrons and Heavy Holes in GaAs, InAs, AlAs, and Their Ternary Compounds," *Physica B,* vol. 210, pp. 1-25, 1995.
[50] M. Sotoodeh, A.H. Khalid, and A.A. Rezazadeh, "Empirical Low-Field Mobility Model for III-V Compounds Applicable in Device Simulation Codes," *J. Appl. Phys.*, vol. 87, pp. 2890-2900, 2000.
[51] C. Hilsum, "Simple Empirical Relationship Between Mobility and Carrier Concentration," *Electronics Lett.*, vol. 10, pp. 259-260, 1974.
[52] W.W. Tyler and H.H. Woodbury, "Scattering of Carriers from Doubly Charged Impurity Sites in Germanium," *Phys. Rev.*, vol. 102, pp. 647-655, 1956.
[53] D.E. Aspnes and A.A. Studna, "Dielectric Functions and Optical Parameters of Si, Ge, GaP, GaAs, GaSb, InP, InAs, and InSb from 1.5 to 6.0 eV," *Phys. Rev. B*, vol. 27, pp. 985-1009, 1983.
[54] A.B. Djurisic *et al.*, "Modeling the Optical Constants of GaP, InP, and InAs," *J. Appl. Phys.,* vol. 85, pp. 3638-3642, 1999.
[55] Measured complex refractive index of $In_{0.5}Ga_{0.5}P$ courtesy of SOPRA Inc., who distributes such data to several physics-based model developers.
[56] D.E. Aspnes, "Recombination at Semiconductor Surfaces and Interfaces," *Surf. Sci.,* vol. 132, pp. 406-421, 1983.
[57] S.J. Pearton *et al.*, "Comparison of Surface Recombination Velocities in InGaP and AlGaAs Mesa Diodes," *J. Vac. Sci. Tech. B*, vol. 12, pp.142-146, 1994.
[58] J.M. Olson *et al.,* "Ultralow Recombination Velocity at $Ga_{0.5}In_{0.5}P$/GaAs Heterointerfaces," *Appl. Phys. Lett.,* vol. 55, pp. 1208-1210, 1989.
[59] *PC1D*, Version 5.9, P.A. Basore and D.A. Clugston, Photovoltaics Special Research Centre, University of New South Wales, Sydney, Australia, 2003.

[60] Y.P. Vrashni, "Band-to-Band Recombination in Groups IV, VI, and III-V Semiconductors (I)", *Phys. Stat. Sol.,* vol. 19, pp. 459-514, 1967.
[61] L. Pavesi and M. Guzzi, "Photoluminescence of $Al_xGa_{1-x}As$ Alloys," *J. Appl. Phys.*, vol. 75, pp. 4779-4842, 1994.
[62] C. Nozaki *et al.,* "Growth Temperature Dependent Atomic Arrangements and Their Role on Band-Gap of InGaAlP Alloys Grown by MOCVD," *J. Crystal Growth,* vol. 93, pp. 406-411, 1988.
[63] N. El-Masry and S.M. Bedair, "Ordered-Disordered Ternary Alloys by Atomic Layer Epitaxy," *Opt. Quantum Elec.,* vol. 23, pp. S909-S913, 1991.
[64] R.G. Alonso *et al.,* "Spontaneous Ordering in $GaInP_2$: A Polarized-Piezomodulated-Reflectivity Study," *Phys. Rev. B,* vol. 48, pp. 11833-11837, 1993.
[65] T. Saß, I. Pietzonka, and H. Schmidt, "Influence of the Domain Size on the Band Gap of Ordered (GaIn)P," *J. Appl. Phys.,* vol. 85, pp. 3561-3564, 1999.
[66] S.F. Keeny *et al.*, "Complete Transient Simulation of Flash EEPROM Devices," in *IEDM Technical Digest*, pp. 201-204, 1990.
[67] P. Michalopoulos, *A Novel Approach for the Development of And Optimization of State-of-the-Art Photovoltaic Devices Using Silvaco*, MS Thesis, Naval Postgraduate School, Monterey, CA, 2002.
[68] R. Gelinas, *A Novel Approach to Modeling Tunnel Junction Diodes Using Silvaco ATALS Software*, MS Thesis, Naval Postgraduate School, Monterey, CA, 2005.
[69] G.A.M. Hurkx, D.B.M. Klaassen, and M.P.G. Knuvers, "A New Recombination Model of Device Simulation Including Tunneling," *IEEE Trans. Elec. Devices,* vol. 39, pp. 331-338, 1992.
[70] G.A.M. Hurkx *et al.*, "A New Recombination Model Describing Heavy-Doping Effects and Low Temperature Behaviour," in *IEDM Technical Digest,* pp. 307-310, 1989.
[71] S.M. Hubbard *et al.*, "Growth and Characterization of InAs Quantum Dot Enhanced Photovoltaic Devices," *Mater. Res. Soc. Symp. Proc.*, vol. 1017E, pp. DD13-11 – DD13-16, 2007.
[72] H. Kroemer and Q.G. Zhu, "On the Interface Connection Rules for Effective-Mass Wave Functions at an Abrupt Heterojunction Between Two Semiconductors with Different Effective Mass," *J. Vac. Sci. Tech.*, vol. 21 pp. 551-553, 1982.
[73] H. Kroemer and Q.G. Zhu, "Interface Connection Rules for Effective-Mass Wave Functions at an Abrupt Heterojunction Between Two Different Semiconductors," *Phys. Rev. B*, vol. 27 pp. 3519-3527, 1983.
[74] R.A. Morrow and K.R. Brownstein, "Model Effective-Mass Hamiltonians for Abrupt Heterojunctions and the Associated Wave-Function Matching Conditions," *Phys. Rev. B.,* vol. 30, pp.678-680, 1984.
[75] R.L. Kronig and W.G. Penney, "Quantum Mechanics of Electrons in Crystal Lattices," *Proc. Royal Soc. London A*, vol. 130, pp. 499-513, 1931.
[76] A. Martí, L. Cuadra, and A. Luque, "Partial Filling of a Quantum Dot Intermediate Band for Solar Cells," *IEEE Trans. Elec. Dev.* vol. 48, pp. 2394-2399, 2001.
[77] A Martí, *et al.*, "Novel Semiconductor Solar Cell Structures: The Quantum Dot Intermediate Band Solar Cell," *Thin Sol. Films,* vol. 511-512, pp. 638-644, 2006.
[78] M.Y. Levy and C. Honsberg, "Nanostructured Absorbers for Multiple Transition Solar Cells," *IEEE Trans. Elec. Dev.,* vol. 55, pp. 706-711, 2008.